ISSN number 0971 - 9709

IGU
Promoting Earth System Sciences

The Journal of Indian Geophysical Union

A SCI Journal

Impact Factor (2025) 0.2

AN OPEN ACCESS BIMONTHLY JOURNAL OF IGU

VOLUME 30, ISSUE 1, JAN. 2026

EDITORIAL OFFICE
Indian Geophysical Union, NGRI Campus, Uppal Road, Hyderabad- 500 007
Telephone: 91-4027012739, 27012332; Telefax:+91-04-27171564
Email: jigu1963@gmail.com, website: http://iguonline.in/journal/

The Journal with six issues in a year publishes articles covering
Solid Earth Geosciences; Marine Geosciences; and Atmospheric, Space and Planetary Sciences.
The Journal is Financially supported by MoES, Govt. of India.

Annual Subscription
Individual Rs -1000/- per issue and Institutional Rs- 5000/- for six issues
Payments should be sent by DD drawn in favour of "The Treasurer, Indian Geophysical Union", payable at Hyderabad,
Money Transfer/NEFT/RTGS (Inter-Bank Transfer), Treasurer, Indian Geophysical Union, State Bank of India, Habsiguda Branch,
Habsiguda, Uppal Road, Hyderabad- 500 007
A/C: 52191021424, IFSC Code: SBIN0020087, MICR Code: 500002318, SWIFT Code: SBININBBHO9.
For correspondence, please contact, Hon. Secretary, Indian Geophysical Union, NGRI Campus, Uppal Road,
Hyderabad - 500 007, India; Email: igu123@gmail.com; Ph: 040 27012332

ISSN: 0257-7968 (Clarivate Analytics)
ISSN: 0971-9709 (NISCAIR)
Approved as bimonthly ESCI journal by Clarivate Analytics
Cited in Indian Citation Index (ICI), New Delhi
Evaluated by NISCAIR, New Delhi
UGC Approved Journal

CONTENTS

Editorial

Research Articles

Scientific Report

J.Ind.Geophys.Union,30(1)(2026),1-5
https://doi.org/10.71122/JIGU.30(1)2026.001

EDITORIAL

Flash floods in Uttarakhand Himalaya: Reasons and remediation

The Himalayan region has been suffering from different kinds of climate-induced geological hazards, out of which the flash floods have been often due to one of the causes of erratic rainfall or cloudbursts, ice/snow avalanches, glacial lakes outburst, landslide lakes outburst, fluvial extremes, abrupt river incisions, reservoir-dam failure, or a combination of two or more of these. The floods have instigated loss of lives and livestock, and/or damage to properties and structures leading to disasters of variable magnitudes. The aspects that have been responsible are, climate change or global warming and stresses persuaded by unplanned anthropogenic activities. It is to be stated that 'çloudburst' is defined as more than 100 mm rainfall per hour, suddenly occurring over a small area. The 'flash flood' is the fast and impulsive inundation, while the normal 'flood' is slower and more prolong that affect generally larger areas with steadily increasing water level. The constricted drainage system and narrow river valley have been attributed to the rainfall-triggered flash floods at many places. There has been cascading effect also due to earthquakes, (caused by plate convergence), to landslides to landslide-lake formation followed by its sudden rupturing to flash floods. It is the landscape and geomorphological features of the Himalaya that control the damage pattern during a catastrophe.

Several factors such as unauthorized civil constructions, non-abiding by building codes, erection of infrastructures in unscientific manner, exposure to vulnerable areas like river beds/banks, and lack of awareness, are attributed to the reasons of disasters. The youngest Uttarakhand (UK) state in the Indian Himalayan Region is ~85% mountainous, and has experienced flash floods and other geological cataclysms from time to time. To mention a few dreaded flash floods are, complete burst of Chorabari Lake leading to glacial lake outburst flood (GLOF) in 2013, Gangotri debris-flow that devastated a large area in 2017, ice-rock mass avalanche at Dhauliganga-Rishiganga catchment in 2021, snow-avalanches in Kedarnath and Hemkund Sahib in 2022, cloudburst events in Arakat-Uttarkashi (2019), Dharchula-Pithoragarh (2023) and Maldevta-Dehradun (2022), and rainfall triggered surge-type flash floods in Dharali-Uttarkashi (2025). The UK Himalaya has also witnessed disasters caused by rainfall-triggered 2003 landslides at Varunavrat Parbat in Uttarkashi, and massacre by earthquakes like Uttarkashi (1991) and Chamoli (1999) due to tectonic movement. Hence, we synthesize some key flash floods in the UK Himalaya to comprehend the reasons and provide their plausible remediation.

On 16th September 2025, Sahastradhara and surrounding areas of Dehradun, were ravaged by flash floods and landslides due to heavy rainfall or cloudburst. Several shops, hotels, homes and infrastructure were washed away or severely damaged, a few people went missing, popular tourist spot was flooded, and pathways were waterlogged. Again on 5th August 2025, a rainfall triggered landslides and massive mud-water flash floods in the Kheer Ganga river destroyed the Dharali village of Uttarkashi district, claiming 5 persons dead, 50 feared missing, several goats swept away, and many houses, shops, homestays and roads destroyed. The brunt of the massacre is also visible at nearby regions of Horsil and Sukhitop. The entire area in mountainous terrain is known for its scenic beauty. It is also the way to pilgrimage site and trekking route to Gangotri glacier and Gomukh, source for the Bhagirathi River. The higher Himalayan crystalline rocks, composed of gneisses, schists and migmatites, are highly weathered, fractured and jointed under the influence of cooling and warming phenomena. of climate variation. The glacio-fluvial deposits or loose debris materials, soaked with snow/glacier melt water, over the steep mountainous slope of more than $>45^{O}$; rainfall at higher elevation; narrow valley with high inclines, created a surge-type flash flood by rapidly mobilizing the mud-water at downstream. However, the disaster was due to unregulated buildings in front of the Kheer Ganga river curve and construction on the alluvial fan and floodplain that disrupted the river's historical drainage path. Since the rainfall is shifting upward, the stations must be deployed at higher elevation for rainfall recording. We also need to look into high resolution drone-based and remote sensing data for establishing the fact of this disaster.

Another climate-surprise disaster in the UK Himalaya was heavy rainfall-triggered slope breakdown near Maldevta-Dehradun in August 2022. This smashed the channel and bank of Song and Baldi rivers for a 15 km stretch between Sarkhet and Thano, and completely eroded Sarkhet, Kumalta and lower portion of Maldevta town. It destroyed/washed away some huts and temporary stalls built on the banks of the river. The cloudburst in Arakot-Uttarkashi in August 2019 made double-impact as flash flood in Arakot nala and landslides at nearby region. This flash flood caused 19 people dead, 8 feared dead, and 15 injured, affected 38 villages covering an area of ~70 km^2, and stranded ~400 people at various places. The Lasko valley in Pithoragarh district of UK state near Indo-Nepal border also witnessed rainfall-induced disaster in September 2022, which caused 6 fatalities, 11 reported missing, 72 houses severely damaged and more than 62 families deserted at

multiple places. During this catastrophe, roads were destroyed, land-degraded, small landslides occurred, minor bridges collapsed, and Lasko valley was also damaged. The reasons of the flash flood have been due to constricted drainage systems through which so much rainwater could not be drained out through the confluence of the Kali river and Lasko nala. In fact, water receded back and inundated upstream villages on the riverside.

In October 2022, intermittent snow avalanches took place in the Mandakini catchment area adjacent to the Kedarnath Temple town. From the analysis of aerial data and ground survey, it was established that the snow-avalanches originated ~6 km uphill of Kedarnath town from the peak of Companion Glacier in the Mahalaya Parvat (5970 masl), closet to the Chorabari Glacier. As the run-out and deposition zones are situated ~5 km uphill of Kedarnath town, it does not pose threat to the temple township by avalanche hazards. The study from the slope morphology, grass clearing, snow drifts, and debris cones have identified fifteen avalanches in this area. The climate-related other incidence is the Atalakodi snow avalanche in Hemkund Sahib in April 2022. This destroyed a section of the trail between Ghangria and Hemkund Sahib. The Atalakodi route is considered a potential site for future snow avalanches. The historical data in this area, shows fatalities due to past avalanches. One of these was in 1998 that buried 27 pilgrims, and another was in 2008 that resulted into 8 deaths and 12 injuries. The Atalakodi avalanche, affected an area of ~4 km long and ~150 m width. The steep slopes, structures and lithologies have been attributed for the snow avalanches in Kedarnath and Hemkund Sahib. The ropeway, environment impact assessment, and construction at no-risk zone have been recommended for the mitigation from such disasters.

Around 968 glaciers and 1,265 glacier lakes with variable sizes,, occur in the UK Himalaya. The large moraine-dammed lakes with appreciable slopes, evolving activities and habitation in downstream, and comparatively fast melting of associated glaciers are critical parameters to be considered for assessing the glaciers-related hazards, which mean glacier detachment primarily that lead to debris flow and flash floods secondarily. A typical example is the 2021 Chamoli disaster caused by a massive avalanche of ice-rock mass in the peak winter on 7th February. The gigantic ice-rock (27 million m^3 in volume) fell down to 3600 masl in the Dhauliganga-Rishiganga basin from a height of 5600 m, got fragmented and melted by its impact and created slurry materials leading to huge deluge. The reason of ice-rock mass detachment has been attributed to the heavy snow precipitation over the hanging glacier and development of cracks and fissures in the underlying basement rocks due to freezing and thawing processes. The debris materials flew down the slopes, disconnected villages by disintegrating roads/bridges, and smashed hydro projects, as well as killed more than 200 people. By analyzing seismological data, retrieved from a nearby station, the scientists from Wadia Institute of Himalayan Geology could identify seismic precursors of glacial avalanche, first of its kind, for about 3 and a half hour's duration before the main event of ice-rock avalanche. This study led to the establishment of a network of seismological stations along with the hydro-meteorological stations, real time transfer of data through VSAT/ GSM, automatic scrutiny and integration of data using suitable AI/ML algorithms and development of an integrated early warning system (IEWS). Such a system is to be developed and deployed at other basins for detection and early warning of glacial hazard.

High sediment transfer continues and might impact hydro-projects in downstream by silting reservoir and/or corroding turbine blades. The stakeholders of hydropower projects must build the IEWS for their dams and take care of maintenance. Understanding the sediment dynamics necessitates for debris flow simulation. The combined remote sensing, field observations and numerical modelling show that 7 million m^3 of debris, deposited by 2021 Chamoli glacial avalanche, was removed along a 30-km-long domain from near its origin by pre-monsoon and monsoon river flows in 12-months post event. The study also showed bed-load and suspended sediments traveling up to 85 km from the event source, which have wider implications to water quality in downstream. Continuous monitoring of sediments and water fluxes using web-based sensors, are essential for safeguarding the ecology of downstream region as well as the health of reservoirs and dams. Therefore, study on fluvial dynamics is crucial for assessing the water availability, management, and protection from devastating flash floods during monsoon.

The June 2013 Kedarnath calamity was caused by GLOF, moraine failure, and insistent rainfall, which inundated 5500 villages, killed 6000 people, detained more than 1 lakh pilgrims in peak summer, and destroyed huge properties and structures. This also led to more than 10,000 small, medium and large landslides in the UK Himalaya. The GLOF's are caused by multiple factors like glacier thinning or recession, sediment/water discharge, lithology, structures, climatic variability, moraine collapse, rainfall, etc. By studying these parameters, we can monitor the glaciers and associated lakes in a comprehensive manner. The drone- or satellite-based techniques can be developed for mapping lake-bathymetry and volume of lake water, as well as to estimate the glacier's thickness and volume of water stored within the glaciers-ice in inaccessible regions. However, the ground penetrating radar and sonar survey can be carried out in the accessible area for the estimation of glacier's thickness and volume of lake-water respectively. The geotechnical, geophysical or geoengineering surveys, can provide strengths of moraine-dammed walls of

glacial lakes against breaching. The rate of water accumulation, amount of downslope, infrastructure and habitation in downstream are acute factors for assessing the glacier-lake related hazards. The hydro-meteorological stations are to be deployed at higher elevations to monitor air temperature, humidity, precipitation, wind speed, wind direction, glacier melt and flow, sediments discharges etc. The elevation dependent warming and its impact to melting of glaciers, need to be modelled. Controlled puncturing or spillways of glacial-lakes, tunneling, laying pipelines inside and pumping or siphoning off water, can be thought of as a remedial measure from GLOF disaster.

The Bhilangana lake in the Tehri-Garhwal region of UK Himalaya, situated at ~4750 m height, has grown to ~0.40 km^2 area in the last 55 years. The associated Khatling glaciers have been observed thinning as per the study made by the scientists of Wadia Institute of Himalayan Geology The air temperature gradient (0.79^OC/decade) has been increased noticeably in the past decade as compared to the average temperature gradient (0.28^OC/decade) over the last three decades. Again, downslope of this region is more than 20 degrees. Thus, close monitoring and assessment of the lake is need of the hour to avert any disaster due to GLOF, as have been observed by complete outburst of Chorabari lake in 2013. This may lead to cascading effects - landslides, landslide lakes outburst floods, debris flow, etc.

The debris flows in the mountainous regions have been caused by landslides, glacial/snow avalanches and floods. The Malpa (Pithoragarh) landslide is one of the worst rain-induced landslides that wiped away entire Malpa village, and generated ~1 million m^3 of rock fall and debris flow. The landslide killed ~ 220 people including 60 pilgrims travelling to Tibet as a part of 'Manas Sarovar Yatra'. A debris flow occurred in the foreland of Gangotri glacier by its former tributary Meru Bamak glacier in July 2017. The Meru Bamak stream was completely dissected that exposed ice-cored left lateral moraines. The study brought out deposition of ~6.5 million m^3 of debris in frontal region of the Gangotri glacier as fan-type. A sharp increase of suspended sediments reaching up to ~3 km downstream, was also noticed. The recession of Gangotri glacier, degraded ice-cored moraine, loose sediments in front of Meru Bamak, and continuous rainfall might have played role to such debris flow. However, it did not incur any disaster due to absence of habitation and structures at nearby area.

The 2003 landslide in sparingly vegetated Varunavrat Parbat, on right bank of the Bagirathi river with Uttarkashi town at its foot, was triggered mainly by the rainfall that was much above the normal, and partly by the groundwater and anthropogenic activities. The debris slide at the top and rock fall in the middle started on the day rainfall ceased, and continued for the next 15 days. The clay-filled joint structures, rock types and degree of slopes were other factors. In similar topographic setting, the 1500 mm of rainfall in monsoonal months, as reported for the Varunavrat landslides, can be considered threshold for landslides. The landslides can be forewarned by coupling slope instability with the rainfall threshold in a vulnerable slope region by establishing a network of web-based sensors like rain gauges, piezometers, inclinometers, extensometers, InSAR, etc., and real-time data assimilation and development of landslides IEWS using IoT based or AI/ML algorithms.

It is to be mentioned that abundant moisture in the atmosphere and increase in land/sea temperatures have been responsible for the torrential rainfall in July-August (2023) in both, the Himachal and UK Himalayas. The confluence of SW monsoon from the Arabian Sea and weak westerly disturbances from the Mediterranean Sea moving eastward has intensified rainfall in the Himalayan region. The warming of atmosphere due to CO_2 or other GHG emission increases the capacity of holding more moisture in the air leading to cloudburst or heavy and sudden rainfall at focused region in the Himalayan regions. The elevated Himalaya acts as a barrier that pushes the moisture-content air upward and get cooled at higher height, leading to condensation and moderate to heavy rainfall in the Himalayan terrain.

The landslides in hilly areas and flash floods in plains have been accredited mainly to the climatic factor – concentrated rainfall over a short span of time, as well as slow but continuous normal rainfall over a longer period of time. The other factor is the land degradation – the top most part, made up of incompetent rocks, is highly weathered under the influence of climate change. The third factor is the anthropogenic stresses like deforestation, unauthorized construction, slope instability due to toe cutting in unscientific way, improper drainage system that allows percolation of water from house-hold kitchen and toilet into the subsurface. The rain water makes the top loose soil saturated and heavy, and underground percolation in a haphazard manner, accelerates the mass movement over the plane of weakness in slope areas causing the landslides under gravity.

For remediation of disaster due to flash floods, pragmatic check dam policy and rational shifting of people from flood-prone riverbanks to safe and stable areas is suggested. It is necessary to develop the flood early warning and alert system by deploying water level sensors, rain gauge sensor, hydrometric gauge, cameras etc. that can be radio-linked with the central station. Installation of Doppler radar and lightning sensors would also aid in monitoring, and can be an effective strategy for damage control. Based on habitation, geomorphology, presence of infrastructure and other natural features for a given region, different scenario of flash floods or

snow avalanches, can be created with different amount of rain or snow precipitation, which will provide precautionary measure to local government authorities in such a moment.

The warming of Himalaya at a faster rate than any other places on the globe in the present climate change situation, is aggravating the geological hazards further. The indicators of climate change on the Himalayan perspectives are visible as glaciers mass loss, expansion and formation of glacier lakes, upward shifts of tree-line and snow-line, rainfall occurrences at higher elevation, and reduction of snow covered area and its early melting. It is projected to face the consequences of further warming with possible rise of 2.6 to 4.6^{O} C by the end of 21st century and complete disappearances of glaciers, if the temperature continues to rise without any control. Again, the Himalaya is stressed by the cascading effects due to tectonic forces leading to earthquakes to landslides to the formation of temporary lakes over streams, followed by their sudden breaching to flash floods. The slope regions of high altitude Himalayas, are becoming weak due to erosion and weathering caused by freezing and thawing processes, and degraded by forest fires. The hassles are worsened additionally by the anthropogenic loads by illegal civil constructions on un-stabilized slopes, habitation over riverbanks and riverbeds, and infrastructure built without proper environment impact assessment. The climate change has not only intensifying the geo-hazards but also posing threat to water scarcity for agricultural and drinking purposes, disruption to hydropower generation due to changes of river dynamics, health insecurities due to heatwaves and pollution, loss of biodiversity and ecosystem, and disturbances to livelihoods and tourism sectors. The future precipitation patterns are also not very clear with some models suggesting augmented rainfall, while others expect diminutions, emphasizing the need for localized assessment.

It must be pointed out that energy is the main driver for socio-economic growth of any country. It is mainly the fossil fuels (coal, oil and natural gas) that supply 80% of the world's gigantic energy requirement till date. However, burning of fossil fuels emanate CO_2, which has been ascribed to the global warming and climate change. The coal produces the maximum amount of CO_2, followed by oil, and the least amount by natural gas. To meet the UN's initiatives of carbon neutrality by 2050 and net zero carbon by 2070 in order to limit further rise of temperature by 1.5 to 2.0^{O} C, we need to make a (i) breakthrough into the renewable or green energy sectors; or (ii) intensifying gradual transition to low-carbon and environment-safe fuels through gasification of coal/oil and development of hybrid technology for synergising two or more different kind of energy resources; or (iii) fortifying carbon capture, utilisation and sequestration experiments by innovative catalytic chemical reaction in which captured carbon can be converted either into usable products like carbonates and methanol, and/or used for enhanced oil recovery and production of marine gas-hydrates by CO_2-CH_4 molecular substitution.

The Himalaya is stressed under the influence of climate change resulting into melting of glaciers and snow fields impacting water availability and agricultural practices, altering weather patterns, land degradation, enlarged geological and hydrological disasters and disruption to ecosystems. Additional stresses are built by the anthropogenic activities. To address such complex issues necessitates a multi-dimensional approach, comprehension of hill-specific challenges and technological barriers for sustainability, integration of scientific understanding with local knowledge, strengthening adaptation and mitigation efforts including the nature based solution (NbS), engagement of native communities, and promoting local and global partnership to build resilience, warrant sustainable future, and secured safe living in the Himalaya.

To comprehend the geological hazards due to flash floods and provide plausible remediation, we need to identify the most vulnerable zones based on geoscientific investigation. Secondly, a network of web-based sensors is to be established at the hotspots for transmission of data from field to processing centre in enabling long term monitoring through analysis and assimilation of data using AI/ML or IoT. The next step is to develop an IEWS to alert and safeguard the people and properties against the disasters. Once the alert system is fully functional in a catchment, similar network can be deployed at other hazard-prone basins or areas of the Himalaya. The system would be designed by deploying different kinds of sensors for diverse types of geo-hazards due to landslides, glaciers/glacier lakes related threats, and floods. It is to be clarified that the investment for development and deployment of IEWS is much more economic than the cost involved in rehabilitation and restructuring, and damages to homes and infrastructure. The loss of invaluable lives cannot be equated in terms of money.

The Himalaya possesses plethora of resources: glaciers and snow field, springs and riverine system, precious minerals and ores, geothermal, hydrocarbon and hydro-power energy resources, medicinal plants, tourist attraction etc. that can be harnessed for the socio-economic growth, agro-cultural development, and strategic advancement but by following certain guidelines and abiding by mountain-specific building codes. A balance between the exploitation of these resources for economy and optimal conservation of the Himalayan fragile ecosystem, must be implemented. Adaptation to NbS like, (i) plantation, vegetation and restoration of forests for protection of slopes and reduction of soil erosion that can reduce the probability of risks due to landslides, (ii) refurbishment of

wetland and degraded riverbanks, and maintenance of natural drainage system to control the floods, (iii) rejuvenation of springs and groundwater recharge areas for mitigation of water scarcity and (iv) implementation of sustainable agroforestry and integrated farming for resilience of ecosystem, are to be made effective by empowering local communities for ensuring long-term success.

The traditional knowledge like usage of light-weight construction materials; implementation of limited storied buildings, and satellite townships instead of having populace around one business town; strict implementation of heavy penalty against unauthorised construction and deforestation; impervious drainage system that will not allow random infiltration of waste water into the subsurface; building retaining walls, wire-mesh, insertion of bolts and shotcrete for arresting slope failure; slope stability assessment before any construction or hill-cutting in a slope region; stringent codes on muck disposal after rock cutting; non-exposure to highly vulnerable areas; disaster-resilient building or retrofitting old buildings; periodic assessment of load bearing capacity at different scales; environment impact assessment, etc. are some of the other measures, which can be considered for mitigation and way forward. We have to sensitize the locals on how to live with the disasters; inculcate fundamental education on the causes and consequences of disasters; build trained manpower for disaster management - preparedness, response, restoration; draw attention of stakeholders to scopes and opportunities for alleviation of challenges; build climate-adaptable and disaster resilient future; and figure out the sustainable growth. The traditional practices, adaptation capacity for resilience, and invaluable knowledge of local communities must be fostered for firming readiness mechanisms and addressing inherent vulnerabilities, which can prepare better for and recover from increasing risks of the UK Himalaya posed by disasters and climate change. It is to be stated that the major hindrances to the adaptation and adoption of several strategies and way forward are the dearth of funds, deficiency of knowledge, absence of technology and lack of mandatory policy

Kalachand Sain
JC Bose National Fellow
CSIR-National Geophysical Research Institute,
Uppal Road, Hyderabad-500007, India
Email: kalachandsain7@gmail.com

J. Ind. Geophys. Union, 30(1) (2026), 6-20
https://doi.org/10.71122/JIGU.30(1)2026.002

Crust-mantle seismic structure along Jakhau-Mandvi DSS Profile: A geodynamic perspective

K. Chandrakala* and Prakash Kumar
CSIR- National Geophysical Research Institute, Uppal Road ,
Hyderabad- 500 007, India
*corresponding Author: chndrbhat@gmail.com

ABSTRACT

Kutch rift basin situated in the northwestern part of the Deccan volcanic province, is characterised by sustained intermediate to deep crustal earthquake activity since historical times, unheard in other global stable terrains. This region underwent through several geotectonic, thermal and magmatic episodes in the past, whose signatures are manifested in various forms including the complex and heterogeneous crust-mantle velocity structure. In order to delineate hydrocarbon-rich Mesozoic sediments and underlying basement configuration, seismic refraction and wide-angle reflection data was acquired along the four Deep Seismic Sounding profiles. In the present study, we reprocessed the seismic data along one of these profiles, shot across the southwestern part of the Kutch region, that runs from Jakhau to Mandvi on the west coast. Our study delineated occurrence of a six-layered sequence above the granitic–gneissic basement (Vp: 5.90–6.00 km/s), with their thicknesses varying from 5.5 to 8 km. It includes, Tertiary sediments (Vp: 2.0 km/s), Deccan basalts (Vp: 4.70 km/s), upper low velocity Mesozoic sediments (Vp: 3.3 km/s), Mesozoic limestone (Vp : 5.1 km/s) followed by Mesozoic volcanics (Vp: 5.50 km/s) and another low velocity Mesozoic sediments (Vp: 5.30 km/s). It is underlain by mid-crustal layer (Vp: 6.30-6.40 km/s) located at depths of around 8 to 12.5 km, which is further underlain by a relatively thinner lower crustal layer (Vp: 6.80-6.90 km/s). Below this layer, we also delineated two distinct underplated magmatic layers (Vp: 7.20 -7.50 km/s) above the Moho, characterize by velocity 7.7-8.0 km/s. Moho is delineated at an extremely shallow depths from 25 to 35 km. Conspicuously, we also depicted a frozen mantle magma chamber (Vp: 8.0 km/s), in the uppermost mantle, which coincides with the location of Katrol Hill Fault. It appears that this region has undergone persistent magmatism, massive subcrustal erosion and asthenospheric upwarping.

Keywords: Kutch seismic zone, Mesozoic sediments, Deccan volcanic province, Magmatic underplating, Frozen mantle magma chamber, Crust-mantle seismic velocity structure, Geodynamics.

INTRODUCTION

Precambrian Indian shield has been associated with a number of rifting episodes, continental breakups and multiple plume interactions that have severely modified its crust-mantle structure on a large scale, (Pandey, 2020). It contains several rift valleys, mega shear zones and lineaments, which have remained active since at least Mesoproterozoic period (Rogers and Callahan, 1987). Consequent to such changes, it has been experiencing moderate-to-large intraplate seismic activity since historical times, which is unheard in other global stable regions. GPS and seismological studies have clearly revealed high strain rates over many parts of the Indian terrain (Talwani and Gangopadhyay, 2001; Paul et al., 2001), compared to much lower strain rates elsewhere in other stable continental regions (Johnston, 1994).

Kutch rift region, located in NW part of Indian subcontinent, is one such region, which is seismically quite active and where intermediate to deep crustal earthquakes of varying magnitudes, keep on occurring. Similar events have also been reported from other global rift zones, like Amazonian (Brazil), East African (Africa), Baikal (Russia), Rio Grande (North America), Narmada-Son (India) and Reelfoot (New-Madrid, USA) (Mukherjee, 1942; Mooney et al., 1983; Prodehl et al., 1994; Johnston, 1996; Liu and Zoback, 1997; Singh et al., 1999; Kruger et al., 2002; Wilson et al., 2003; Gao et al., 2004). Nevertheless, the Kutch region remains a unique site of sustained intraplate seismicity for a long time. Rajendran and Rajendran (2001) reported some 15 historical and recent earthquakes of magnitude 5 to 6 that took place in this region earlier. This was also substantiated by paleo-seismological studies, which confirmed such occurrences since 325 BC (Rajendran et al., 2008). In fact, during last couple of hundred years alone, it has witnessed three large earthquakes (besides numerous moderate events) like, 1819 Kachchh (Mw: 7.8), 1956 Anjar (Mw: 6.0) and 2001 Bhuj (Mw: 7.7), the last one causing widespread damage and killed more than 20,000 people (Chung and Gao, 1995; Gupta et al., 2001; Rajendran and Rajendran, 2001; Rajendran et al., 2008; Mandal and Pandey, 2010, 2011; Pandey, 2020).

Geotectonically, this region severely suffered through many tectonic, thermal and magmatic episodes including Deccan volcanism, scars of which are amply manifested in the form of complex and heterogeneous crust-mantle velocity structure, as revealed by seismological and other geological and geophysical studies (Biswas, 1987; Gambos et al., 1995; Kayal et al., 2002; Mandal, 2006, 2007; Mandal and Pujol, 2006; Mandal and Chadha, 2008; Mandal and Pandey, 2010, 2011). In order to delineate Mesozoic sediment thickness, basement configuration and shallow crustal seismic structure, seismic refraction and wide-angle reflections data was acquired along four DSS profiles, (i) Jakhau-Mandvi, (ii) Mandvi-Mundra, (iii) Mundra –Adesar, and (iv) Hamipur-Halvad, by CSIR-National Geophysical Research Institute, Hyderabad (India) during 1996-1997. These profiles trend NW-S, W-E, SW-NE and N-S directions respectively and cut across several geotectonic units of the region.

Prasad et al., (2010) provided basement structure along these profiles, while preliminary seismic-reflection images of the

crust was given by Sarkar et al., (2007). Earthquake tomographic and seismic refraction studies have earlier also indicated presence of crustal intrusives and thick underplated magmatic layer at lower crustal levels, as well as below the Moho (Sarkar et al., 2007; Kayal et al., 2002; Mandal and Chadha, 2008; Mandal and Pandey, 2010, 2011). In the present study, we made an attempt to delineate the detailed shallow and deep crustal-upper most mantle seismic structure along the Jakhau-Mandvi profile, shot across the NW-SE segment of the Kutch basin (Figure 1). This study has provided a new light on the geodynamic evolution of the western Indian region.

REGIONAL GEOLOGY AND TECTONICS

The seismically active east–west trending intra-continental Kutch rift basin, is located between 22° 30' and 24° 30' N and 68° and 72° E in the Kutch district of Gujarat, India (Figure 1) (Biswas, 2005; Mandal and Pandey, 2010, 2011). This severely faulted basin, which is about 400 km in length and 150 km in width, has a typical geometry of an asymmetric rift basin, which is bounded by Nagar Parkar fault (NPF) in the north and the North Kathiwar Fault (NKF) in the south (Merh, 1995; Biswas, 2005). It is characterized by three main uplifted blocks (Island Belt, Kutch Mainland and Wagad) with intervening grabens and half-grabens. The Other major faults in the region are, the E–W trending Allah Bund fault, Island Belt Fault, Kutch Mainland Fault and Katrol Hill fault (KHF). A meridional/median high zone forms the another striking feature. This basin is slightly tilted towards the south and contains about 3–5 km thick young Tertiary and Mesozoic sediments that overly Precambrian basement (Biswas, 1987). It preserves the longest record of the Mesozoic succession in the western India, which are often folded, faulted, uplifted, and intruded by 66 Ma Deccan volcanics (Biswas, 1987, 2005). Besides, it is also characterised by a series of east–west trending uplifted structures, formed as a result of crustal movements of discrete basement blocks along the pre-existing ancient faults, which may have association with the concealed Delhi orogenic belt trends.

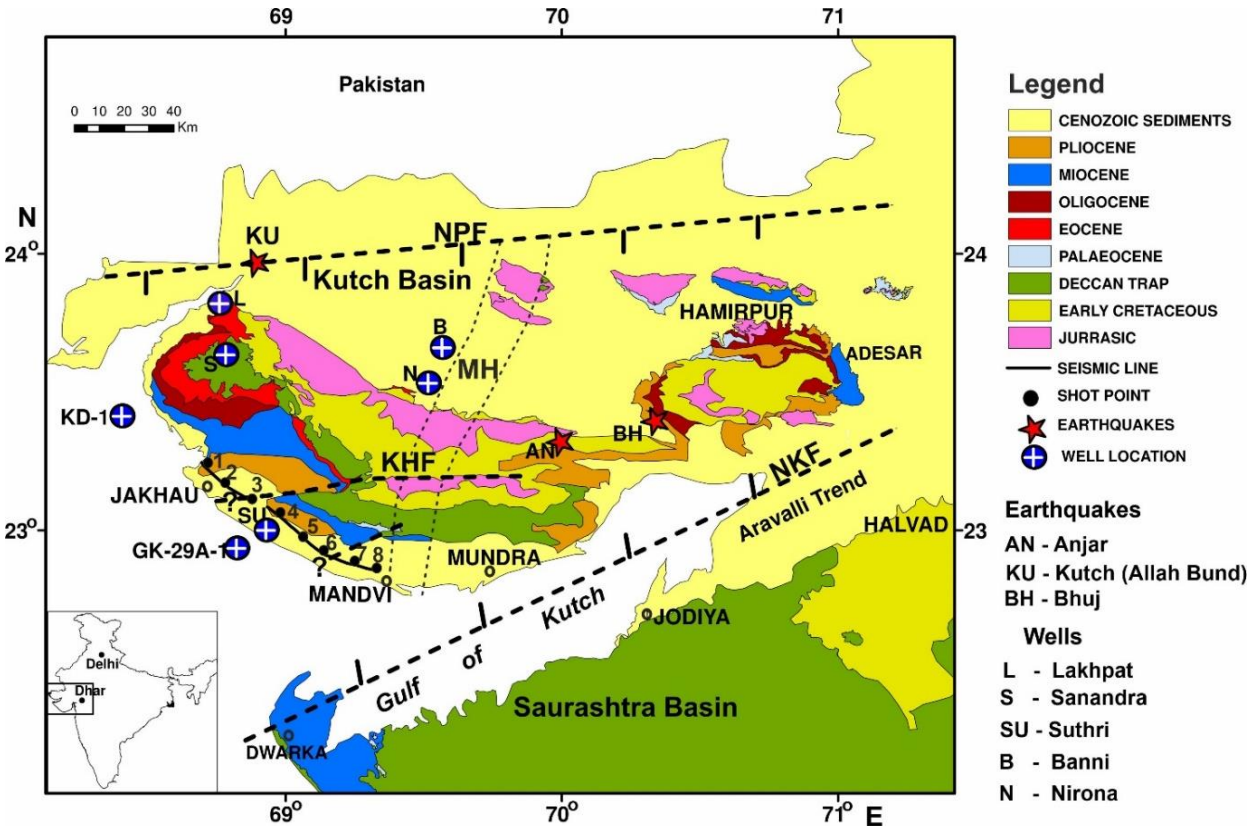

Figure 1. Geological and tectonic map of Kutch basin along with the location of the seismic refraction and wide-angle reflection profile. Solid blue circles encircling '+' represents well locations. L: Lakhpat; S: Sanandra; Su: Suthri; B: Banni; N: Nirona. Major earthquakes are shown with red stars and their names are represented by AN: Anjar Earthquake (1956); BH: Bhuj Earthquake (2001); KU : Kutch Earthquake (1819) (Allah bund Earthquake). Faults are shown with black dashed lines. NPF- Nagar Parkar Fault; NKF: North Kathiawar Fault; KHF-Katrol Hill Fault; MH: Median high. The black solid circles with numbers indicate Shot Points. NPF and NKF are considered the northern, southern boundaries of the Kutch rift basin.

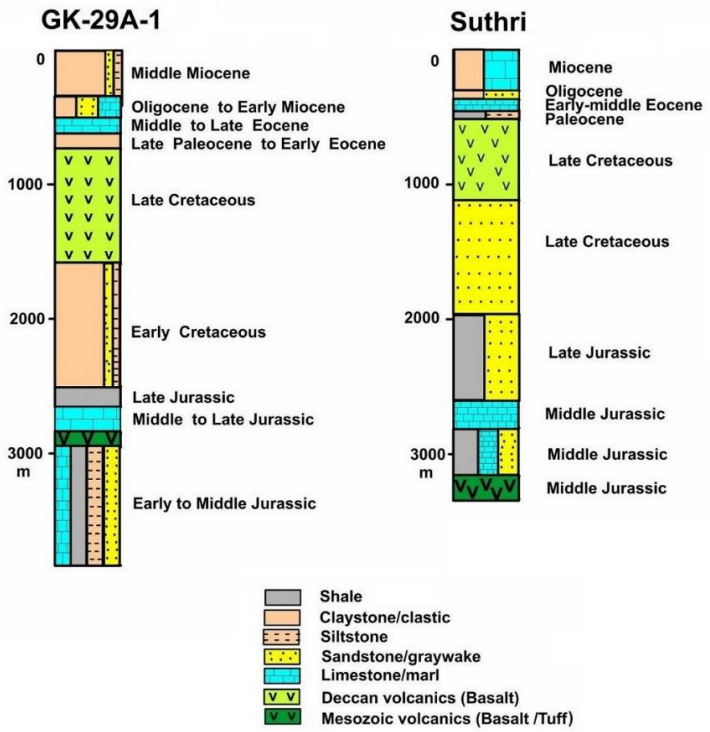

Figure 2. Lithostratigraphic sections encountered in the drilled deep wells, located over onshore and offshore regions. Their locations are shown in Figure 1 (Singh et al., 1997; DGH, 2015)

This basin is also severely affected by 66 Ma Deccan volcanism, as well as Jurassic magmatism, which occurred during Antarctica-Africa rifting phase related to the east Gondwana breakup period, as evidenced by their occurrences at subsurface depths in GK 29A-1, Suthri, Lakhapt and Lodhika drilled boreholes (DGH, 2015). The lithostratigraphy of the region, as pearced by GK 29A-1 and Suthri boreholes, are shown in Figure 2. Similarly, small patches of Deccan volcanics can be seen exposed close to its south-west periphery, west of Anjar. On its eastern side, it is separated from the Cambay rift while on its western side, it extends into offshore areas of the Arabian sea. Geodynamically, this region is also affected by the NE–SW compressive stress, consequent to collision of Indian and Eurasian plates. Being an ancient rift basin, it has been persistently active prior to and during the Deccan volcanic episode (Biswas, 1987) and India –Eurasia collision as well.

SEISMIC STUDIES

Data Acquisition

The seismic refraction / wide angle reflection data along Jakhau - Mandvi (NW-SE) profile was acquired by the Controlled Source Seismic (CSS) group of CSIR- National Geophysical Research Institute, using two 60 channel Texas Instrument model DFS-V recording systems (NGRI, 2000). Data was recorded with a spread length of 11.9 km and geophone spacing of about 100 m. Each spread was recorded with a number of shot points of varying offsets 10 to 50 km. Shot holes were drilled to a depth of 20 m, with 10 m of hole to hole distance in a rectangular / triangular pattern. Each shot is loaded on average with 50 kg high energy explosives (Open Case Gelignite 83 mm/Telgex LD 83 mm). To enhance the signal, four to six geophones of natural frequency 4.5 Hz were connected in series and bundled at each geophone position. A notch filter (with 50 Hz frequency) was kept in operation to minimize the effects of power line pick up. Data was recorded in both analog as well digital form up to 20 seconds. Due to logistic reasons, there was a gap in data acquisition, which was shown in the surface coverage map (Figure 3).

Data processing

The Jakhau – Mandvi profile consists of 8 shot points, with good quality recorded data, as is evident from the field seismograms of the shot points SP2 and SP7 (Figure 4 a, b). The signal-to-noise ratio of the first arrivals is good across most of the sections. Strong reflection phases are very clear at offset of 20 to 60 km from the shot location. From this figure, a travel time jump in the first arrival refraction times is clearly noticeable, which indicates that the refractions are not reaching to the surface for a particular time window, and this delay in time, appears as a skip on the seismograms. Such shift in first arrival travel times (skip) occur due to certain geological conditions.

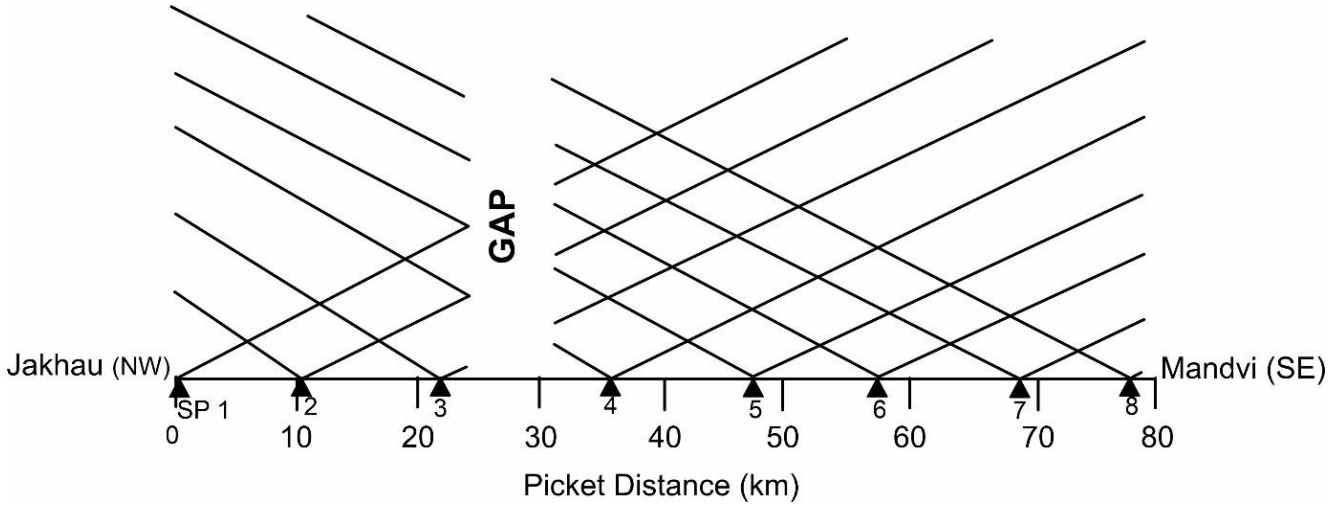

Figure 3. Schematic diagram of the surface coverage along the Jakhau-Mandvi seismic profile.

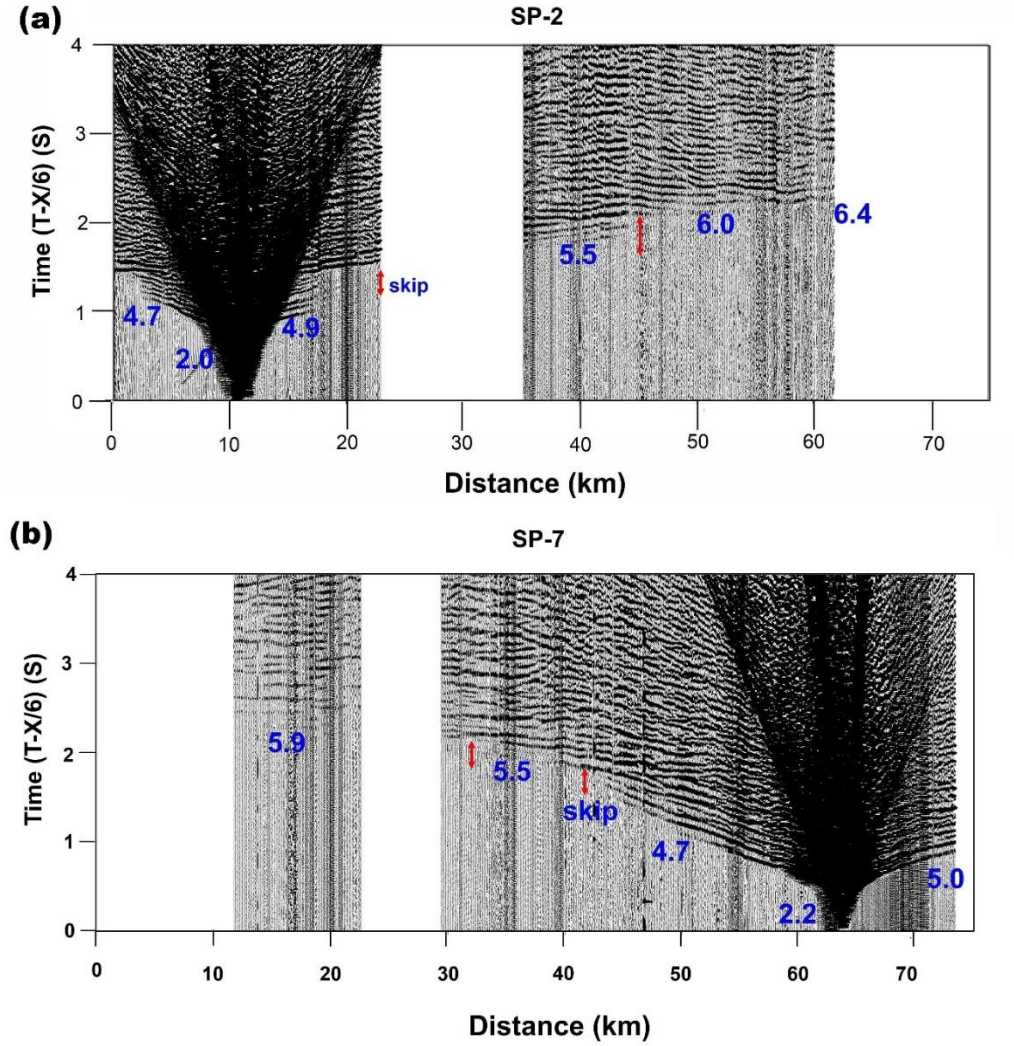

Figure 4. Shot gathers of shot points, **(a)** SP 2 and **(b)** SP 7, along the Jakhau – Mandvi seismic profile. Various phases and corresponding velocities are marked with number (km/s). Skip in the travel time is marked with red arrow (not to scale), which is ascribed to the presence of low velocity layer.

Theoretically, the necessary condition in seismic refraction method is that the velocities of all the underlying layers should increase with depth. In such cases, the first arrival refraction from each layer appear as a continuous segment, without any break. If there is a break or jump in the first arrivals, then it usually occurs in two cases: (i) if the velocity of a layer is lower than that of the overlying layer, no critically refracted waves will be generated from the top of the low-velocity layer (Dobrin, 1976) and this layer is not detected in the first-arrival time-distance plot (Whiteley and Greenhalgh, 1979; Lutter et al., 1994; Tewari et al., 1995; Dixit et al., 2000; Koteswara Rao et al., 2004, Kolluru and Behera, 2025) (ii) The other possibility of skip could be due to a fault. Importantly, we have noticed presence of skip in all the seismograms in every shot point data; SP 2 and SP 7 being shown in Figure 4. Thus, the skip occurrence due to a fault is not tenable, as a fault is a localized phenomena. Thus, based on the seismic data, the skip in the present study in considered due to presence of a low velocity only.

Similarly, to strengthen our assumption, we have looked in to the two drilled bore wells, one located near the present studied profile (Suthri around 10 km from SP4) and the other one, GK 29A-1 situated in the nearby onshore region (Figures 1 and 2). Based on the lithostratigraphy of the drilled bore wells (Figure 2), the Tertiary sediments is defined as layer-1; Deccan basalt, layer-2; sandstone, layer-3; limestone, layer-; dolerite /trachyte/tuff/basalts/volcanic, layer-5; and stringers of sandstone, shale and limestone that sits above the basement as layer-6. These rock formations (layers) are assigned with seismic velocities, which are derived from the first arrival travel times from the seismograms (Figure 4). Further, based on the drilled lithology and the hidden layers from the seismic studies, we have assigned low velocity layers to the Mesozoic sediments, that exist below the Deccan volcanic (traps), as well as Mesozoic volcanics (Figure 2). These inputs are used for modelling of crustal seismic structure.

The first arrival travel times are picked up from seismograms to calculate true and apparent velocities (Figure 4). The travel time data from the all the shot points, reveals presence of a thin sedimentary layer with velocity varying from 1.9 - 2.2 km/s. Since this velocity is measured from the direct arrival times, it represents the true velocity of the exposed Tertiary sediments. Similarly, the measured apparent velocities are assigned to the corresponding rock formation based on well log data. The first LVL (layer-3) is correlated with Mesozoic sandstone, which is exposed at the surface near Dhrangadhra region of Saurashtra. It is characterized by velocity 3.8 km/s (Chari, 1974; Uniyal, 1985; Prasad et al., 1985). DSS studies carried out earlier along Tikor-Wankaner-Mangrol profile, has also reported a velocity of 3.1 km/s for the exposed Mesozoic sandstone (NGRI, 1998). Based on these velocities and lithostratigraphic thicknesses (~ 300 m) as obtained from the borehole results, we assign a velocity 3.3 km/s to match the travel time data. Presence of such sediments are also reported from the Banni, Danduka, Lodhika (Dixit et al., 2000) and GK-29A-1 borewells (Figure 2). A similar LVL (layer-6) above the basement, is also being reported here for the first time, that was not reported in earlier studies (Pandey et al., 2009; Prasad et al., 2010; Prasad et al., 2013). Also during modelling, it was found necessary to introduce a low velocity layer to match the observed data

Data modelling

To derive 2-D velocity model, we have used raytracing technique developed by Zelt and Smith, (1992) and Zelt (1999), which uses efficient ray tracing equations (Zelt and Ellis, 1988*)*. In this approach, the model is defined as a sequence of layers separated by boundaries. In each layer, the upper boundary and lower boundary is defined by P-wave velocity. During ray tracing, the model is discretized into irregular trapezoidal cells with dipping interfaces, and velocity is linearly interpolated within each cell using the P-wave velocities at its four corner points. A smooth layer boundary simulation is used to avoid scattering and focusing of ray paths. Based on dominant frequency (20 Hz) of the data, we assign uncertainties of 100 ms for the first arrival travel times, as signal is not strong enough due to the absorption of energy from the volcanic rocks. The detailed methodology is given in Chandrakala et al. (2015, 2023).

The modelling have been carried out by preparing an initial 1-D velocity model that has been derived from all the shot point data. This model has been refined until there is satisfactory agreement between the observed and calculated travel times. The top layer, which is exposed at the surface gives the true velocity of the formation. We followed layer stripping method, where the interface between the first and second and the velocity of second layer, are calculated by inverting travel time data. Thereby, we have derived the shallow depth section till the basement. The ray diagrams and corresponding travel time matches are shown in Figure 5.

Similarly, for deriving deeper depth section, we utilize the reflection data. We have picked up prominent reflection phases from each shot points. Reflections from the Moho is limited to only a few shot points due to the small profile length. Shot gathers of the shot point SP 1 is shown in Figure 6, which indicates the quality of the signals. In this record section, one can notice the strong reflection phase which looks like a continuous scratch over the seismograms, which is observed in a time window around 4 – 6 s (reduced travel time) and at a distance of 30 to 55 km from the shot location, that represent the reflections from the Moho (Figure 6)

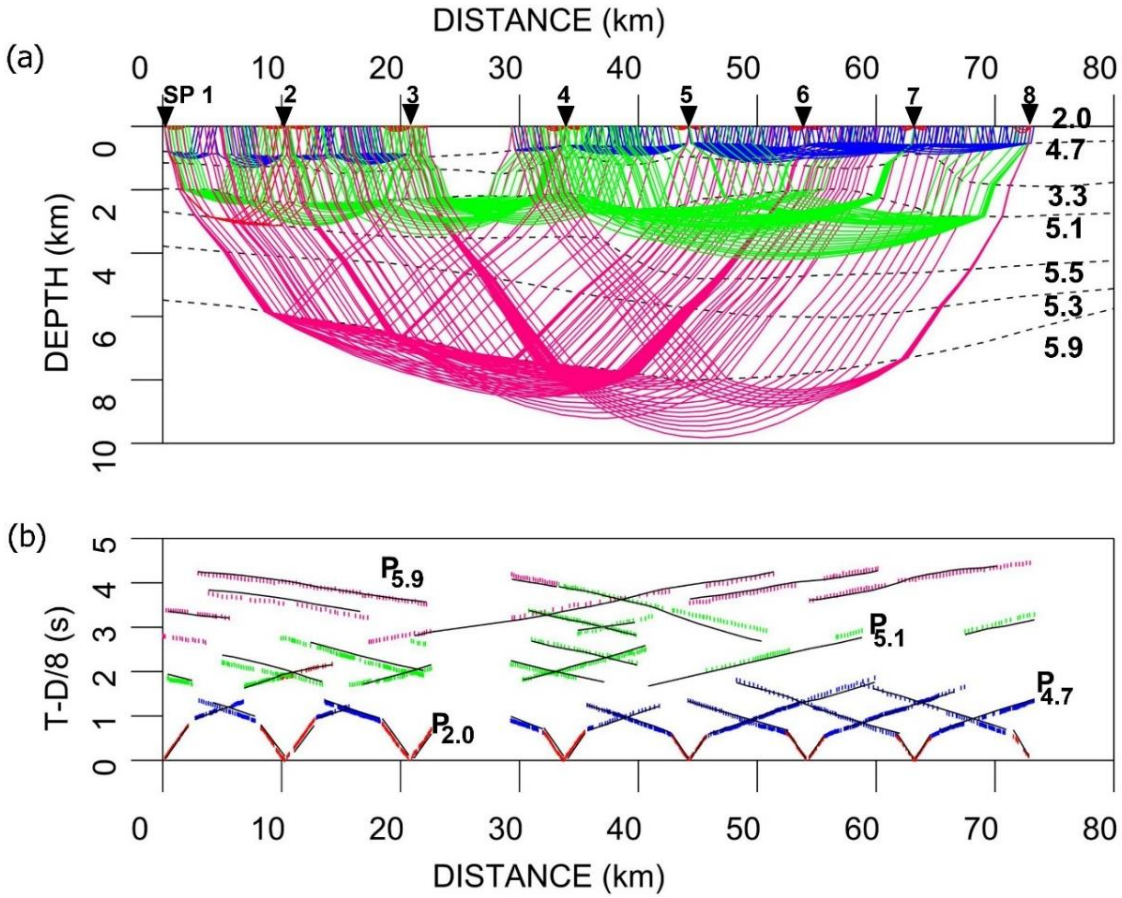

Figure 5. (a) Ray diagram showing the subsurface coverage by the refracted rays through the final derived velocity model. The numbers represent the velocity in km/s. **(b)** The comparison between the observed (vertical bars) and theoretical (solid lines) travel times for all the phases plotted in reduced travel time of velocity 8.0 km/s for clarity. The refraction travel time data is represented by various colours for various phases. Subscript represents refracted velocities.

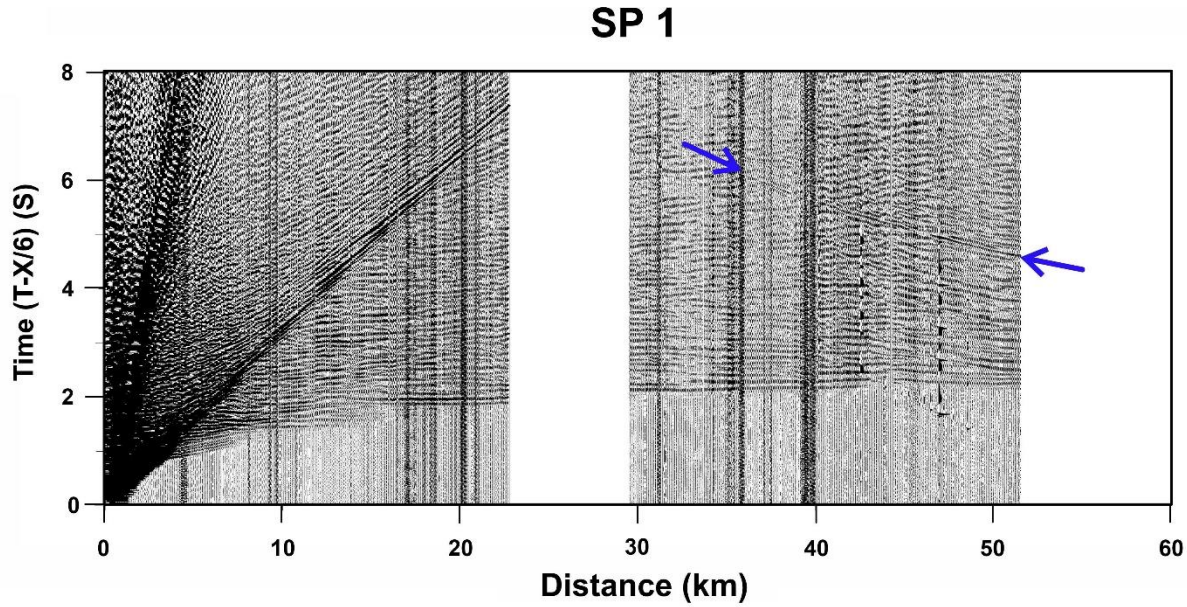

Figure. 6 Trace-normalized seismogram for shot point SP 1 shown with a reduction velocity of 6.0 km/s. Strong reflection phase from the Moho is indicated by blue arrow.

To improve the signal-to-noise ratio, we used the band pass filter (2-8-18-22 Hz) and isolated the signal from ground roll to enhance the quality of the data **(**Figure 7a). Once the reflections phases are identified, we have carried out modeling to match these reflection phases, as mentioned earlier. Due to the small profile length, the deeper section is prepared solely on the basis of reflection phases, as it lacks refractions from the deeper depths. The velocities for deeper depths have been considered from the nearby seismic studies *(*Kaila et al., 1980, 1990; Surya Prakasa Rao and Tewari 2005). The model has been modified until we obtained satisfactory agreement between the observed and calculated travel times for all the shot points.

The derived final model has been checked by comparing the relative amplitudes of observed phases to those with theoretical ones for each shot point by using ray theory code (Zelt and Smith, 1992). It can be seen from the record sections that there is a reasonably good agreement between the synthetic and the observed seismograms (Figure 7).

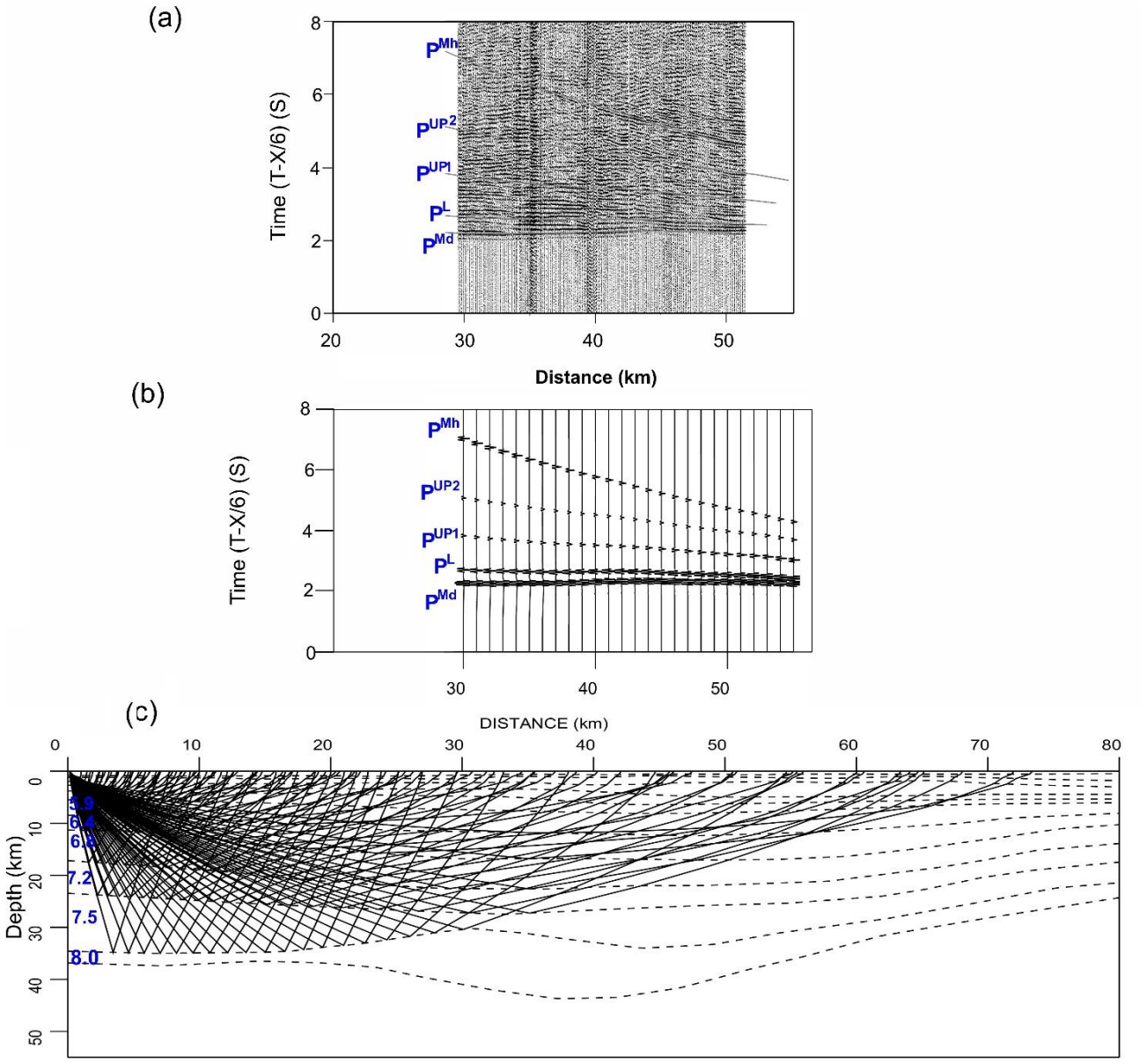

Figure 7. (a) Trace-normalized seismogram of shot point SP 1 with a reduction velocity of 6.0 km/s. Grey line represents theoretically calculated travel times through derived velocity model, which is overlapped on the seismogram to compare with the observed, and **(b)** the corresponding synthetic seismogram in the same distance range. **(c)** Ray diagram showing the subsurface coverage by reflected rays from various crustal layers. All distances marked on the X-axis are from 'zero' position of the model. Reflections from the top of the mid crust, lower crust, first and second underplated magmatic layers and the Moho, are represented by P^{Md} , P^{L} , P^{UP1} , $P^{UP2,}$ and P^{Mh} respectively. The numbers represent velocity in km/s.

The Moho usually produces a strong, coherent reflected phase in seismic records due to the significant change in acoustic impedance (density and velocity contrast). This reflection phase can be a sharp, discrete event or a band of reflectivity. In the present study, we have noticed sharp and coherent phases in shot points SP 1, SP 7 and SP 5 (Figures 6 and 8). We have further noticed that these strong reflection phases occur in a time window around 4 – 6 s (reduced travel time) and at a distance of 30 to 55 km from the shot location. Globally, such Moho reflection phases in the continental crust are usually observed around 10 - 14 s (two-way travel time), where as in the regions associated with crustal extension or rifting, the Moho can be located at around 7 to 9 s. Nevertheless in our case, the estimated two way time is around 4 – 6 s, that would indicate that the Moho is at much shallower depths.

Floating reflectors

While modeling the observed strong Moho reflection phases, we found it necessary to introduce floating reflectors, as it needed different Moho depths for the shot points SP1, 5 and 7. The reciprocity of the travel time and coherence of the signal indicated that these reflection phases are from the Moho boundary only (Figure 6, 8). In shot point SP 1, the theoretically generated reflections from the Moho are at a deeper depth of around 30-35 km and it matches well with the observed phase (Figure 7). Similarly, for SP 7, the Moho depth is relatively shallower than the SP 1, with different dip (Figure 8 b). But for SP 5, to match these Moho reflections, it requires relatively deeper depth. Due to limitations of this method, within the short distances, such reflections cannot be generated to match the observed data. Thus to match these reflection phases, we introduce floating structures using the algorithm from Zelt and Smith (1992) in order to constrain the geometry of these reflectors. Usually, such floating reflectors are introduced once velocities have been well resolved. Since, the floating reflecting boundaries are interfaces with no associated velocity discontinuity, it is called floating, where rays can reflect in addition to the layer boundaries. In the present study, we identify that these boundaries, occur below the Moho with continuation to shallow depths towards SP 1 (Figure 8a). In similar situations, floating reflectors has earlier been introduced by many workers worldwide (Epili and Mereu, 1991; Mooney and Meissner, 1992; Zelt and Forsyth, 1994; Zelt et al., 1994; Zelt and White, 1995; Luosto, 1997; Zelt,1999; Chandrakala et al., 2023). Location of the introduced floating reflectors and their corresponding match with the observed data, is included in Figure 8a b. In SP 7, theoretically generated reflections from the floating reflectors matches well with the observed phases (Figure 8 b). We show in Figures 9 and 10, the shallow and deep crustal velocity model as derived from the first arrival refraction and wide-angle reflection data and drilled borewell lithology.

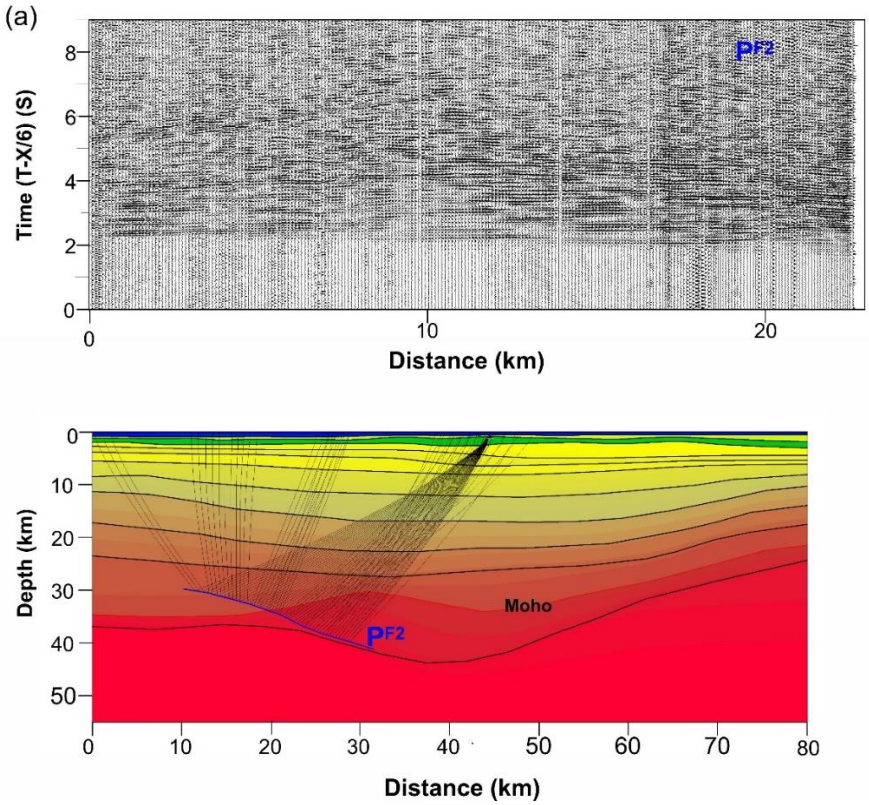

Continued…

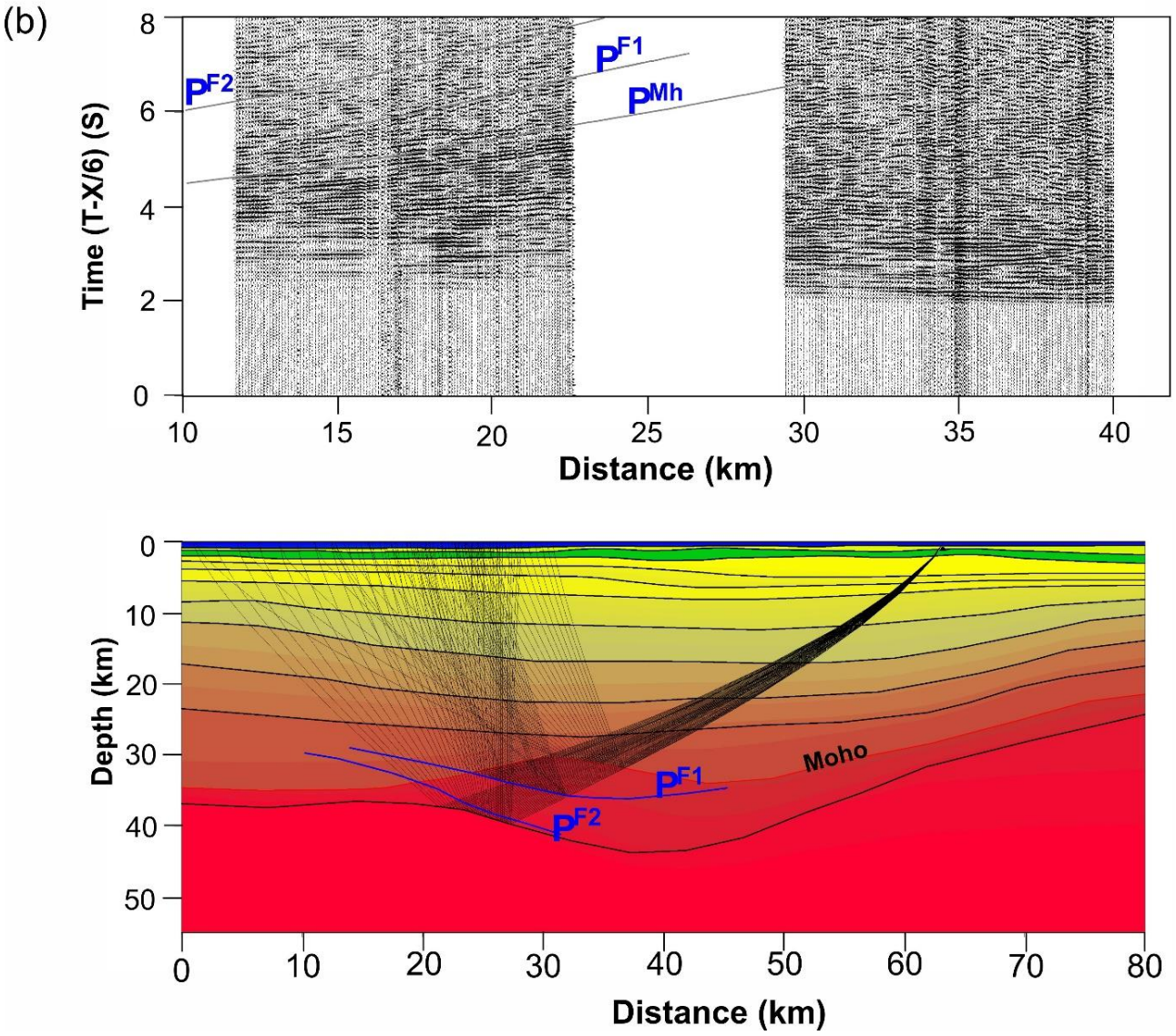

Figure 8. Trace-normalized seismogram of shot points **(a)** SP 5 and **(b)** SP 7, shown with a reduction velocity of 6.0 km/s. Theoretically calculated reflection phases from the Moho (P^{Mh}) and floating reflectors (P^{F1} and P^{F2}) are overlapped on the seismograms to show the match. All the distances marked on the x-axis are with reference to the zero position of the model.

RESULTS

Shallow crustal seismic structure

Figure 9 reveals presence of six distinct layers above the Precambrian granitic-gneissic basement, characterized by velocity 5.90 to 6.00 km/s. The first layer corresponds to exposed Tertiary sediments, exhibiting a very low average velocity of 2.0 km/s and has a thickness varying from 400 m to 900 m above the Deccan basaltic layer (Vp: 4.60-4.80 km/), which has a variable thickness. Deccan basalt is only about 300 m thick below Jakhau, compared to about 1400 m below the Mandvi, located at the eastern end of the profile, which is more than the maximum drilled thickness of about 1250 m in the Koyna seismic zone, located in the Western Ghats region (Mishra et al., 2017**)**. Below this layer, occurs a 1000 to 1300 m thick low velocity layer (LVL), with velocity 3.30 km/s, which corresponds to Mesozoic sandstone. It conforms with the drilled well information (Figure 2). It is underlain by relatively higher velocity Mesozoic limestone (Vp: 5.10 km/s) which overlie a thick (1000-2000 m) Mesozoic volcanic layer that has a considerably higher velocity of 5.50 km/s compared to Deccan volcanic layer (Vp: 4.7 km/s). It is further underlain by another Mesozoic sedimentary LVL layer, characterised by a velocity of 5.30 km/s. Its thickness varies from 1000 m to 2500 m. This layer directly rests over the Precambrian granitic-gneissic basement. We delineated two fault zones, located between SP 3 and SP 5, and SP 6 and 7. The first one may corresponds to Katrol Hill Fault.

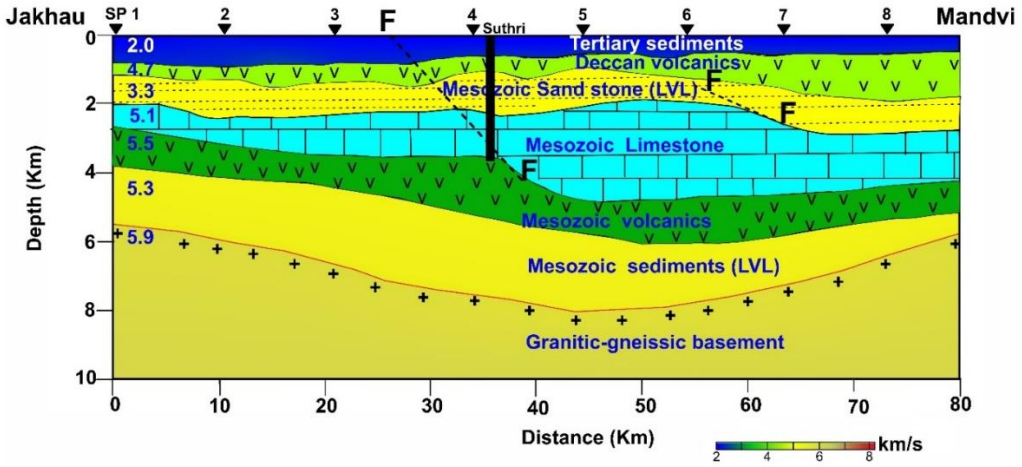

Figure 9. Shallow crustal seismic velocity section along the Jakhau – Mandvi seismic profile. Inverted triangle represents the shot point location. Red line represents the basement. Dash line indicates location of delineated faults (F). Velocities in different crustal layers are in km/s. Location of Suthri well, which falls in the closed vicinity of the profile, is also shown.

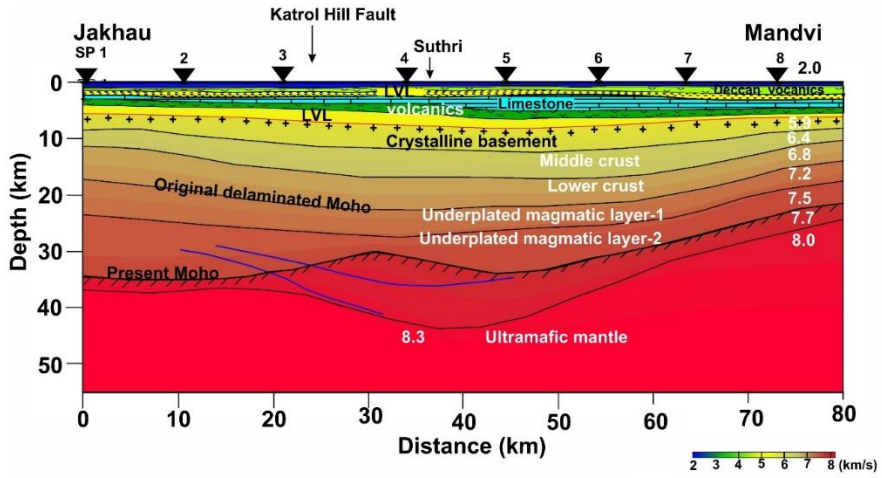

Figure 10. Final crustal seismic velocity depth section along Jakhau–Mandvi DSS profile. Inverted triangle represents the shot point location. The basement is shown by red line. Blue line indicates floating reflectors. Velocities in different crustal layers are in km/s.

Deeper crustal seismic structure

The deeper crustal section, as shown in Figure 10**,** indicates that the depth to the Precambrian granitic-gneissic basement (5.9-6.0 km/s) along the profile varies about 5.5 km to 8 km, maximum being observed between SP 4 and SP 6. It rests over a mid-crustal layer characterize by velocity of 6.30-6.40 km/s and its depth varies from 8 to 12.5 km from the surface. It is underlain by the mafic lower crust (Vp: 6.80-6.90 km/s) which has a much smaller thickness of 4.5 to 6.5 km only. The derived model further exhibits the occurrence of two distinct underplated magmatic layers, around 8 to 17 km thick. It is quite thick below Jakhau and relatively thinner below SP 3 to SP 5, which coincides with the Katrol Hill Fault. The top magmatic layer (UP1) is characterised by a velocity 7.20 km/s, while the bottom one (UP2), has a much higher velocity of 7.50 km/s. Such high velocities at the base of the crust would represent a zone of severe crust-mantle thermal interaction.

Further, the Moho is characterized by a velocity of 7.7 - 8.0 km/s. Moho is conspicuously shallow at the depth of 25 km near Mandvi (Vp: 7.7 km/s) compared to about 35 km near Jakhau (Vp: 8.0 km/s). There is a noticeable upwarping of the Moho to about 30 km below SP 4. Importantly, our study also delineated presence of a frozen mantle magma chamber (Vp: 8.0 km/s) below the Moho in the uppermost mantle, which occurs below SP 3 to SP5. Its bottom is bounded by the normal ultramafic mantle (8.3 km/s) at 43 km depth (Figure 10). It coincides with the location of Katrol Hill Fault. It may have been formed due to mantle upwelling caused by strong crust-mantle thermal interaction.

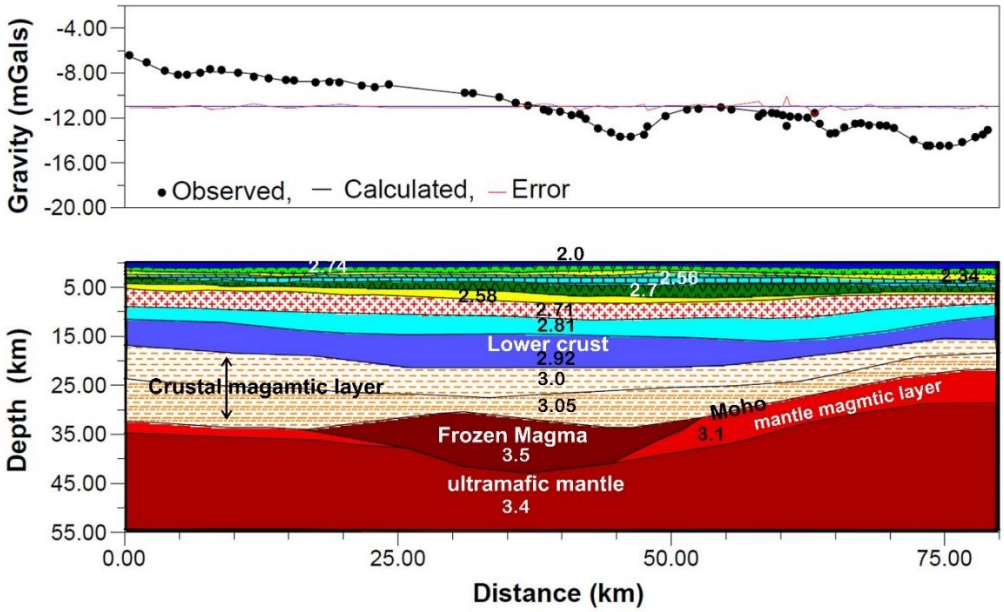

Figure 11. Comparison of observed and computed gravity response over the derived crustal density model, based on the seismic structure imaged along Jakhau –Mandvi DSS profile. The density values are in g/cm^3.

GRAVITY MODELLING

We also made an attempt to model the gravity field along the studied profile using the seismic constraints from the present study. Over this region, the gravity data was acquired with 5 mGal interval during 1997-1999. For the present study, we used the Bouguer gravity values along this profile from NGRI (2000) (Figure 11), which shows a large regional variation from NW to SE. To carry out two-dimensional gravity modelling, we use GM-SYS software (Geosoft Oasis Montaj, 2004). In this method, the response is calculated based on the algorithms of Talwani et al. (1959), Talwani and Heirtzler (1964) and Won and Bevis (1987). Following that, inversion calculations are made using algorithm of Marquardt (1963). The number of iterations (close to reality) with less RMS error provides the best-fit model. We converted derived crustal seismic structure into density using the velocity-density relationship of Nafe and Drake (1957) and Ludwig et al. (1970). The values of the input parameters and depth of the each layers have been accordingly changed to minimize the difference in a least square sense between the observed and computed Bouguer gravity fields. The derived gravity model is shown in Figure 11**,** which corroborates well with the obtained seismic image

DISCUSSIONS

Sediment thickness and crust-mantle structure

The shallow crustal section (Figure 9**)** revealed presence of six distinct layers above the granitic-gneissic basement (Vp: 5.90 to 6.00 km/s) with a maximum estimated thickness of 8 km. It is comprised of Tertiary sediments, Deccan basaltic layer, Mesozoic Limestone and two low velocity Mesozoic sedimentary layer (LVL). These Mesozoic sediments extend further into the Gulf of Kutch, where its reported thickness is between 2 and 4 km (Gopala Rao et al., 2021). Apart from this, sedimentary section also contains a 1 – 2 km thick Mesozoic volcanic layer, characterized by a relatively higher velocity (Vp: 5.5 km/s) than the overlying Deccan volcanics (Vp: 4.7 km/s). Its presence has been substantiated by the drilled-boreholes GK-29A-1 and Suthri (Figure 2), apart from Danduka and Lodhika wells in the Saurasthra region. In the Lodhika borehole, its drilled thickness is more than 500 m thick. This magmatic layer appears related to magmatism associated with Jurassic LIP (Large Igneous Province), which was formed during the India-Africa-Antarctica breakup (Leat, 2008). It may be thus surmised that even the Kutch and Saurashtra regions of western India, were severely affected by east Gondwana breakup, as also evidenced by the presence of subsurface Mesozoic volcanics and widespread thick magma underplating across the Moho (Figure 10). In this region, Moho is at extremely shallow depths due to subcrustal erosion and asthenospheric upwarp (Mandal and Pandey, 2010; 2011; Pandey, 2020). Magmatic extrusive activity during early Tertiary and Jurassic periods, is well reflected into regional uplifting and positive gravity anomalies over the Kutch and Saurashtra regions (NGRI 1998, 2000). Possibly, this region is still under going quaternary uplifting and substantial neotectonic activity, as indicated by recurring seismic activity. Being an ancient rift basin, it has been persistently active prior to and even during the Deccan volcanic episode (Biswas, 1987), as well as India –Eurasia collision. Currently, this region has been included in zone VI in the Earthquake hazard zone map (IS 1893, Part 1, 2025), which is comparable to Himalayan arc seismicity. This region is also

strongly affected by the NE–SW compressive stress generated due to collision of Indian and Eurasian plates.

Anomalous shallowing of Moho

Consequent to the upwarping of the asthenosphere, the crust–mantle thermal interaction and subsequent sub crustal erosion, the Moho beneath this region is also seems to be severely affected. We found a conspicuously shallow Moho (only 25 km) near Mandvi, which has a quite lower Moho velocity (Vp: 7.7 km/s), compared to that found below the normal ultramafic mantle (Vp: > 8.0 km/s). Similarly, it is about 35 km deep near Jakhau. Recent studies based on multi-channel seismic reflection data and gravity modeling, Gopala Rao et al. (2021) derived a Moho thickness between 15 and 18 km in Gulf of Kutch region. Similarly, Chopra et al. (2014), analysed the crustal seismic structure of Gujarat through tele seismic receiver function studies. In their study, two of their seismic stations Naliya (NAL, 23.33°N, 68.83°E) and Gadhshisha (GDS, 23.10° N, 69.34°E) falls close to our seismic profile. It is interesting to see that they also found a shallow Moho thickness of 26.5 and 30.5 km respectively for these two stations. It appears that the Gulf of Kutch may be rifting and percolating to the main land of Gujarat due to persistent magmatism, massive sub crustal erosion and asthenospheric upwarping.

Massive magma underplating

A significant part of the lower crust worldwide is often seen stacked- up by the mantle-derived reworked magmatic rocks, consequent to the lower crustal and hot lithospheric mantle interaction (Rudnick and Fountain, 1995; Gao et al., 1998; Pandey et al., 2013; Pandey, 2020). Figure 10 indicates that the studied region too is underplated by an unprecedented thick layer of accreted magmatic rocks, just above the Moho. It is located at a depth between 15 and 23 km all along the profile. The crustal magmatic layer is about 8 to 17 km thick from place to place. It is characterised by two distinct velocities, 7.20 km/s in upper magmatic layer (UP1) and a much higher velocity 7.50 km/s in the lower magmatic layer (UP-2). Besides, we also found a lens-type mantle magmatic body at the base of the crust in the uppermost part of the mantle as well, which extends below SP 3 to SP 6. This region coincides with the Katrol Hill Fault. We attribute this body to a frozen magma chamber. This body is quite thick at about 12 to 13 km below SP 3 to SP 4. It has a high modelled density of 3.5 g/cm^3 representing contribution from the deeper hot mantle interaction.

Our findings are well supported by the detailed receiver functions studies carried out by Mandal and Pandey (2010, 2011). They used teleseismic events from 14 broadband seismic network, deployed over the Kutch seismic zone and obtained One-dimensional velocity model for the Vp and Vs derived from the three dimensional velocity tomograms below the 2001 Bhuj earthquake region. They reported 10 km thick underplated magmatic layer between the depth of 24 and 34 km above the Moho, which is further followed by 8 km thick differentiated Mantle magmatic layer between 34 and 42 km, characterized by velocity of 7.75-8.11 km/s which compares favourably with Vp: 8.0 km/s obtained for the mantle magma layer below SP3 to SP 6. Haldar et al. (2022) also carried out receiver functional studies in the Kutch and Saurashtra region and found the presence of mafic/ultramafic material in the crust-mantle transition zone. Below the central part of the Kutch region, estimated heat flow (61.3 mW/m^2), the Moho temperature (630° C) and Mantle heat flow (43 mW/m^2) are also quite high (Vedanti et al., 2011; Pandey et al., 2017). Consequently, below this region, the LAB is highly upwarped to a shallow depth of around 63 to 70 km only (Mandal and Pandey, 2011; Pandey et al., 2017; Pandey, 2020).

CONCLUSIONS

Reprocessing of the seismic data along Jakhau-Mandvi profile, reveals an extremely unusual crust-mantle structure underneath. It provided some significant results about the evolutionary nature of this seismically active region. The following major conclusions can be drawn from the present study:

1. The shallow crustal seismic section contains six-layered sequence (i) Tertiary sediments (1.9 - 2.2 km/s), (ii) Deccan basalts (4.70 km/s), (iii) low velocity Mesozoic sediments - I (3.30 km/s), (iv) Mesozoic limestone (5.1 km/s), (v) Mesozoic volcanic (5.50 km/s), and (vi) low velocity Mesozoic sediments-II (5.30 km/s) above the crystalline basement that occurs at the depths of about 5.5 km to 8 km. It is followed by a mid-crustal (Vp: 6.30-6.40 km/s) and a relatively thin lower crustal layer (Vp: 6.80-6.90 km/s).

2. We find presence of two distinct underplated magmatic layers associated with varying velocities (Vp: 7.20 -7.50 km/s), with their thickness ranging from 8 to 17 km, indicating a strong crust- mantle thermal interaction and massive subcrustal erosion due to mantle upwelling.

3. Moho is found to be at an extremely shallow depths of about 25 km near Mandvi, and 35 km near Jakhau.

4. Further, we also found a frozen mantle magma chamber (Vp: 8.0 km/s), which is located just below the Moho and coincides with the location of Katrol Hill Fault.

Acknowledgements

The permission accorded by the Director, CSIR- National Geophysical Research Institute, Hyderabad to publish this

work is gratefully acknowledged. We sincerely thank Dr. O. P. Pandey, Chief Editor of the Journal of Geophysical Union (JIGU) and the two anonymous learned reviewers for their immensely helpful comments that greatly improved the quality of our paper. KC thanks the Department of Science and Technology (New Delhi) for the financial support to carry out this study through a project SR/WOS-A/EA-62/2021(G). We acknowledge Mrs. K. Renuka for her assistance in seismic data processing. We owe our sincere thanks to the DSS field persons for acquiring high quality seismic data.

Authors Contribution

K. Chandrakala: Data curation, methodology, seismic and gravity modelling, conceptualization, interpretation, original draft writing, Prakas Kumar: Guiding the research work, review and editing.

Data Availability

Basic data is available with CSIR- NGRI, Hyderabad.

Compliance with Ethical standards

No conflict of interest and authors adhere to copyright norms.

REFERENCES

Biswas, S.K., 1987. Regional framework, structure and evolution of the western marginal basins of India. Tectonophysics, 135, 302–327.

Biswas, S.K., 2005. Special section: Intraplate seismicity a review of structure and tectonics of Kutch basin , western India, with special reference to earthquakes. Curr. Sci., 88, 1592–1600.

Chandrakala, K., Pandey, O. P., Prasad, A. S. S. S. R. S. and Sain, K., 2015. Seismic imaging across the Eastern Ghats Belt-Cuddapah Basin collisional zone, southern Indian Shield and possible geodynamic implications. Precamb. Res., 271, 56–64.

Chandrakala, K., Pandey, O.P., Mandal, B and Prasad, A.S.S.S.R.S., 2023. Complex Crust-Mantle Seismic Structure below North Cuddapah Basin-Eastern Ghats Collisional Belt, South Indian Shield: Regional geodynamics and East Antarctica Correlation. J. Asian Earth Sci., 248, 105606. DOI: 10.1016/j.jseaes.2023.105606.

Chari, K.V., 1974. Refraction and seismic survey in Viramgam, Surendranagar, Wadhwan, Sayla, Chotila, Saurashtra, Gujarath, ONGC Rep (unplublished).

Chopra, S., Chang, T.M., Saikia, S., Yadav, R.B.S., Choudhury, P. and Roy, K.S., 2014. Crustal structure of the Gujarat region, India: New constraints from the analysis of teleseismic receiver functions. J. Asian Earth Sci., 96, 237-254. doi.org/10.1016/j.jseaes.2014.09.023.

Chung, W.Y. and Gao, H., 1995. Source parameters of the Anjar earthquake of July 21, 1956, India and its seismtectonic implications for the Kutch rift basin. Tectonophysics, 242, 281–292.

DGH, 2015. National Data Repository, Directorate General of Hydrocarbons(DGH), MoPNG, Government of India (https://www.ndrdgh.gov.in/NDR/?page_id=742)

Dixit, M. M., Vani, N. S., Sarkar, D., Khare, P. and Reddy, P. R., 2000. Velocity inversion in the Lodhika area, Saurashtra peninsula, Western India. First Break, 18, 499-504. doi.org/10.1046/j.1365-2397.2000.00109.x.

Dobrin, M. B. 1976. Introduction to geophysical prospecting (3rd ed.). McGraw-Hill.

Epili, D. and Mereu, R.F., 1991. The Grenville Front Tectonic Zone: Results from the 1986 Great Lakes onshore seismic wide-angle reflection and refraction experiment. J. Geophys. Res., 96, 16335–16348.

Gambos, A.M., Powell Jr. W.G. and Norton, I.O., 1995. The tectonic evolution of western India and its impact on hydrocarbon occurrences: an overview. Sediment. Geol., 96, 125–130.

Gao, G., Luo, T.C., Zhang, B.R., Zhang, H.F., Han, Y.W., Zhao, Z.D. and Hu, Y.K., 1998. Chemical composition of the continental crust as revealed by studies in east China. Geochim. Cosmochim Acta, 62, 1959-1975.

Gao, S.S., Kelly, H., Liu, H. and Chen, C., 2004. Significant crustal thinning beneath the Baikal rift zone: new constraints from receiver function analysis. Geophys. Res. Lett., 31, L20610:1–L20610:4.

Geosoft Oasis Montaj. 2004. GM-SYS version 7.0 Gravity and magnetic modeling software user guide. Northwest Geophysical Associates Inc.

Gopala Rao, D., Krishna, K.S., Harinarayana, T., Veeraswamy, K., Abdu Azeez, K. K., Ismaiel, M., Chaubey, A. K., and Srinivas, K.and Sreejith, K.M., 2021. Crustal structure of the Gulf of Kachchh, northwest India. J. Earth Syst. Sci., 130, 1-16.
doi.org/10.1007/s12040-021-01623-0.

Gupta, H. K., Harinarayana, T., Kousalya, M., Mishra, D.C., Indra Mohan, Puranachandra Rao, N., Raju, P.S., Rastogi, B.K., Reddy, P.R. and Sarkar, D., 2001. Bhuj earthquake of 26th January, 2001. J. Geol. Soc. India, 57, 275–278.

Haldar, C., Prakash Kumar, Pandey, O.P., Sain, K. and Kumar, S., 2022. Lower crustal intraplate seismicity in Kachchh region (Gujarat, India) triggered by crustal magmatic infusion: Evidence from shear wave velocity contrast across the Moho, Geosyst. Geoenviron., 1(3), doi.org/10.1016/j.geogeo.2022. 100073.

IS 1893, Part 1, 2025. Design earthquake hazard and criteria for earthquake-resistant design of structures-Code of practice Part 1: General provision (seventh revision).

Johnston, A.C., 1994. Seismotectonic interpretations and conclusions from the stable continental region seismicity data base, Chapter 4. In: The Earthquakes of stable continental regions , Vol. 1, Assessment of large earthquake potential, prepared by A.C. Johnston et al., prepared for Electric Power Research Institute, Calif. (USA), p.4-1 to 4-103.

Johnston, A.C., 1996. Seismic moment assessment of earthquakes in stable continental regions. Geophys. J. Int., 124, 381–414.

Kaila, K. L., Tewari, H. C. and Sarma, P. L. N., 1980. Crustal structure from deep seismic sounding studies along Navibandar-Amreli profile in Saurashtra, Mem. Geol. Soc. India, 3, 218–232.

Kaila, K. L., Tewari, H.C., Krishna, V.G., Dixit, M.M., Sarkar, D. and Reddy, M. S., 1990. Deep seismic sounding studies in the north Cambay and Sanchor basins, India, Geophys. J. Int., 103, 621–637

Kayal, J.R., Zhao, D., Mishra, O.P., De, R. and Singh, O.P., 2002. The 2001 Bhuj earthquake: tomographic evidence for fluids at the hypocenter and its implications for rupture nucleation. Geophys. Res Lett., 29, 2152–2155.

Kolluru, R. and Behera, L. (2025). Imaging intra-volcanic Mesozoic sediments and shallow crustal configuration from traveltime inversion of long-offset seismic data in

Saurashtra basin, India. J. Ind. Geophys. Union, 29(4), 218-235.

Koteswara Rao, P., Dixit, M.M., Khare, P., Kesava Rao, G., Raju, S., Sain, K., Murthy, A.S.N., Sarma, V.Y.N., Prasad, ASSSRS, Sridher, V., Reddy, M.S., Reddy, P. R. and Sarkar, D., 2004. Hidden Mesozoic Sediments – Searching with Seismic Refraction Tool. 5th Conference & Exposition on Petroleum Geophysics, pp 81-84.

Kruger, F., Scherbaum, F., Rosa, J.W.C., Kind, R., Zetsche, F. and Hohne, J., 2002. Crustal and upper mantle structure in the Amazon region., Brazil. determined with broadband mobile stations. J. Geophys. Res., 107 (B10) ESE 17-1–17-12.

Leat, P.T., 2008. Ferrar Large Igneous Province, Antarctica. In: The Geol. Soc. London, Special Publ., 302, 45–66.

Liu, L. and Zoback, M.D., 1997. Lithospheric strength and intraplate seismicity in the New Madrid seismic zone. Tectonics, 16, 585–595 .

Ludwig, W. J., Nafe, J. E. and Drake, C. L., 1970. Seismic refraction. In A. E. Maxwell (Ed.), The Sea (pp. 53–84). New York: Wiley-Interscience.

Luosto, U., 1997. Structure of the Earth's Crust in Fennoscandia as Revealed from Refraction and Wide-Angle Reflection Studies. Geophysica, 33, 3–16.

Lutter, W.J., Catchings, R.D. and Jarchow, C.M., 1994. An image of the Columbia Plateau from inversion of high-resolution seismic data. Geophysics, 59, 1278–1289.

Mandal, P., 2006. Sedimentary and crustal structure beneath Kachchh and Saurashtra regions, Gujarat, India. Phys. Earth Planet. Int., 155(3–4), 286–299.

Mandal, P., 2007. Sediment Thicknesses and Qs vs. Qp relations in the Kachchh rift basin, Gujarat, India using Sp converted phases. Pure Appl. Geophys., 164, 135–160.

Mandal, P. and Pujol, J., 2006. Seismic imaging of the aftershock zone of the 2001 Mw 7.7 Bhuj earthquake, India. Geophys. Res Lett., 33. doi: 10.1029/2005GL025275 .

Mandal, P. and Chadha, R.K., 2008. Three-dimensional velocity imaging of the Kachchh seismic zone, Gujarat, India. Tectonophysics, 452, 1–16.

Mandal, P. and Pandey, O.P., 2010. Relocation of aftershocks of the 2001 Bhuj earthquake: a new insight into seismotectonics of the Kachchh seismic zone, Gujarat, India. J. Geodyn., 49, 254–260.

Mandal, P. and Pandey, O. P., 2011. Seismogenesis of the lower crustal intraplate earthquakes occurring in Kachchh, Gujarat, India. J. Asian Earth Sci., 42, 479–491.

Marquardt, D. W., 1963. An algorithm for least squares estimation of non-linear parameters. J. Soc. Industrial Appl. Math., 11, 431–441.

Merh, S.S., 1995. Geology of Gujarat. Geological Society of India, 170pp.

Mishra, S., Vyas, D., Nikalje, D., Warhade, A. and Roy, S., 2017. A 1251m-thick Deccan flood basalt pile recovered by scientific drilling in the Koyna region, western India. J. Geol. Soc. India, 90, 788–794.

Mooney, W. D. and Meissner, R., 1992. Multi-genetic origin of crustal reflectivity: a review of seismic reflection profiling of the continental lower crust and MOHO, In: Fountain, D. M., Arculuta, R., Kay.(Eds) Continental lower crust, Elsevier Sci., 45-79.

Mooney, W.D., Andrews, M.C., Ginzburg, A., Peters, D.A. and Hamilton, R.M., 1983. Crustal structure of the northern Mississippi embayment and a comparison with other continental rift zones. Tectonophysics 94, 327–348.

Mukherjee, S.M., 1942. Seismological features of the Satpura earthquake of the 14th March 1938. Pro. Indian Acad. Sci., 16, 167–175.

Nafe, J.E. and Drake, C.L., 1957. Variation with depth in shallow and deep water marine sediments of porosity, density and the velocities of compressional and shear waves. Geophysics, 22, 523-552.

NGRI, 1998. Integrated geophysical studies for Hydrocarbon exploration Saurashtra, India. NGRI Technical report No. NGRI-98-EXP-237.

NGRI, 2000. Integrated Geophysical Studies for Hydrocarbon Exploration, Kutch, India. Technical Report: NGRI 2000-EXP-296. pp. 1–195.

Pandey, D., Singh, S., Sinha, M. and MacGregor, L., 2009. Structural imaging of Mesozoic sediments of Kachchh, India, and their hydrocarbon prospect. Marine Petrol. Geol., 26, 1043–1050.

Pandey, O. P., 2020. Geodynamic Evolution of the Indian shield: Geophysical Aspects. Springer Nature, Switzerland, 349pp .

Pandey, O.P., Vedanti, N., Srivastava, R.P. and Uma, V., 2013. Was Archean Dharwar Craton ever stable? A seismic perspective. J. Geol. Soc. India, 81, 774–780.

Pandey, O. P., Vedanti, N. and Srivastava, R, P., 2017. Complexity in Elucidating Crustal Thermal Regime in Geodynamically Affected Areas: A Case Study from the Deccan Large Igneous Province (Western India). J. Geol. Soc. India, 90 (3), 289–300.

Paul, J., Burgmann, R., Gaur, V.K., Bilham, R., Larson, K.M., Ananda, M.B., Jade, S., Mukal, M., Anupama, T.S., Satyal, G. and Kumar, G., 2001. The motion and active deformation of India. Geophys. Res. Lett., 28, 647-650.

Prasad, A.S.S.S.R.S., Sain, K. and Sen, M.K., 2013. Imaging sub basalt Mesozoics along Jakhau-Mandvi and Mandvi-Mundra profiles in Kutch sedimentary Basin from seismic and gravity modeling. Geohorizons, 51-55.

Prasad, B. R, Venkateswarlu, N., Prasad, A. S. S. S. R. S., Murthy, A. S. N. and Sateesh, T., 2010. Basement configuration of on-land Kutch basin from seismic refraction studies and modeling of first arrival travel time skips. J. Asian Earth Sci., 39(5), 460–469.

Prasad, S., Bapat, R.D. and Singh, R.B., 1985. Evolving a methodology for exploration of subtrappean Mesozoic sediments in Saurashtra-Phase-III . Acquistion, Processing and interpretation of data of Refraction Lines 2-1-1R and 201-2R of field season 1983-1984, ONGC Rep (unpublished).

Prodehl, C., Keller, G.R. and Khan, M.A., 1994. Crustal and upper mantle structure of the Kenya rift. Tectonophysics, 236, 1–483.

Rajendran, C.P. and Rajendran, K., 2001. Characteristics of deformation and past seismicity associated with the 1819 Kutch Earthquake, Northwestern India. Bull. Seismol. Soc. Am., 91 (3), 407–426.

Rajendran, C.P., Rajendran, K., Thakkar, M. and Goyal, B., 2008. Assessing the previous activity at the source zone of the 2001 Bhuj earthquake based on the near- source and distant paleoseismological indicators. J. Geophys. Res., 113 B05311, doi:10.1029/20 06JB0 04845.

Rogers, J.J.W. and Callahan, E.J. 1987. Radioactivity, heat flow and rifting of the Indian continental crust. J. Geol., 95, 829–836.

Rudnick, R.L. and Fountain, D.M., 1995. Nature and composition of the continental crust: a lower crustal perspective. Rev. Geophys., 33, 267–309.

Sarkar, D., Sain, K., Reddy, P.R., Catchings, R.D., Mooney, W.D., Stein, S. and Mazzotti, S., 2007. Seismic-reflection images of the crust beneath the 2001M = 7.7 Kutch (Bhuj) epicentral region, western India. In: Continental Intraplate Earthquakes: Science, Hazard, and Policy Issues. Geol. Soc. America, 425, 319–327 .

Singh, D., Alat, C.A., Singh, R.N. and Gupta, V.P., 1997. Source rock characteristics and hydrocarbon generating potential of Mesozoic sediments in Lodhika Area, Saurashtra Basin, Gujarat, India. Proceedings Second Int. Pet. Conference & Exbn. Petrotech-1997, New Delhi, India, pp 205-220.

Singh, S.K., Dattatrayam, R.S., Shapiro, N.M., Mandal, P., Pacheco, J.F. and Midha, R.K., 1999. Crustal and upper mantle structure of Peninsular India and source parameters of the May 21, 1997, Jabalpur earthquake., Mw = 5.8.: results from a new regional broadband network. Bull. Seismol. Soc. Am., 89, 1632–1641.

Surya Prakasa Rao, G. and Tewari, H. C., 2005. The seismic structure of the Saurashtra crust in northwest India and its relationship with the Réunion Plume, Geophys. J. Int., 160, 18–330.

Talwani, M. and Heirtzler, J. R., 1964. Computation of magnetic anomalies caused by two dimensional bodies of arbitrary shape. In G. A. Parks (Ed.), Computers in the mineral industries, Part 1. Stanford University Publication, Geological sciences, 9, 464–480.

Talwani, P. and Gangopadhyay, A., 2001. Tectonic framework of the Kachchh earthquake of 26 January 2001. Seism. Res. Lett., 72(3), 336–345.

Talwani, M., Worzel, J. L. and Landisman, M., 1959. Rapid gravity computations for two dimensional bodies with application to the Mendocino submarine fracture zone. J. Geophys. Res., 64, 49–59.

Tewari, H. C., Dixit, M. M. and Murty, R. K.,1995. Use of traveltime skips in refraction analysis to delineate velocity inversion1. Geophys. Prospect., 43(6), 793-804.

Uniyal, S.D., 1985. Operational report on refraction survey in Amreli-Kodinar area of Saurashtra, Gujarat state, ONGC Report. (unbpublished)

Vedanti, N., Pandey, O.P., Srivastava, R.P., Mandal, P., Kumar, S. and Dimri, V.P., 2011 Predicting heat flow in the 2001 Bhuj earthquake (Mw=7.7) region of Kachchh (western India), using an inverse recurrence method. Nonlin. Process. Geophys., 18, 611-625.

Whiteley, R.J. and Greenhalagh, S.A., 1979. Velocity inversion and shallow seismic refraction method. Geoexploration, 17, 125-141.

Wilson, D., Aster, R. The RISTRA Team, 2003. Imaging crust and upper mantle seismic structure in the southwestern United States using teleseismic receiver functions. Lead. Edge, 22, 232–237 .

Won, I. J. and Bevis, M., 1987. Computing the gravitational and magnetic anomalies due to a polygon: Algorithms and Fortran subroutines. Geophysics, 52, 232–238.

Zelt, C. A., 1999. Modeling strategies and model assessment for wide-angle seismic travel time data. Geophys. J. Int., 139, 183–204.

Zelt, C. A. and Ellis, R. M., 1988. Practical and efficient ray tracing in two dimensional media for rapid travel time and amplitude forward modeling. Canadian J. Expl. Geophys., 24, 16–31.

Zelt, C. A. and Smith, R. B., 1992. Seismic travel time inversion for 2-D crustal velocity structure. Geophys. J.Int.,108, 16–34.

Zelt, C.A. and Forsyth, D.A., 1994. Modeling wide-angle seismic data for crustal structure: Southern Grenville province. J. Geophys. Res. 99 (B6), 11687–11704.

Zelt, C.A. and White, D.J., 1995. Crustal structure and tectonics of the southeastern Canadian Cordillera. J. Geophy. Res. Solid Earth, 100 (B12), 24255–24273.

Zelt, C.A., Forsyth, D.A., Milkereit, B., White, D.J., Asudeh, I., and Easton, R.M., 1994. Seismic structure of the Central Metasedimentary Belt, southern Grenville Province. Can. J. Earth Sci., 31, 243–254.

Received on: 17-12-2025; Revised on 24-12-2025; Accepted on 24-12-2025

J. Ind. Geophys. Union, 30(1) (2026),21-34
https://doi.org/10.71122/JIGU.30(1)2026.003

Insights into crustal structure of Aravalli-Delhi Fold Belt and adjoining Bundelkhand craton-Marwar block from gravity models: Significance for Precambrian tectonics in NW India

Om Prakash, Niraj Kumar, A. K. Pandey, **K. N. D. Prasad and A. P. Singh***
CSIR-National Geophysical Research Institute, Uppal Road, Hyderabad-500007 (India)
Corresponding Author: apsingh_ngri@yahoo.com

ABSTRACT

The 2.5D crustal density structure is modelled using complete Bouguer anomaly along two W-E profiles across the Marwar block, Aravalli-Delhi Fold Belt (ADFB), and the Bundelkhand craton, constituting the north-western edge of the Indian Shield. The rock density closely mimics the litho-tectonic units that preserve the Archean-Proterozoic evolutionary history. The Bouguer anomaly along the profiles, corresponds to significant variation in crustal structure, with Moho depth varying from 34 to 40 km under the Marwar block, ~45 km under high-relief ADFB and <42 km under the Bundelkhand craton. A high-density (2.78 g/cm^3) 6-8 km thick sill in the upper crust and a 10-12 km thick high-density (3.05 g/cm^3) body as the mantle underplating at the Moho, represent the source conduit of the Neoproterozoic Malani Igneous Suite in the Marwar block. The significant lithological variation within the 8-10 km thick upper crust with a 12-13 km thick elongated high-density (3.05 g/cm^3) basaltic body with a diffused Moho signature, possibly representing the mantle underplating due to orogenic root delamination under the ADFB. The lateral variation in the crustal structure across the craton suggests the orogenic reworking during the early-mid Proterozoic and mantle upwelling in an extensional regime during the Neoproterozoic in the ADFB and Marwar lock.

Keywords: Northwestern India, 2.5D Gravity modelling, Crustal density structures, Geodynamics, Aravalli-Delhi Fold Belt, Bundelkhand craton

INTRODUCTION

The Aravalli-Delhi Fold Belt (ADFB) together with the adjoining Bundelkhand craton towards the east and Marwar block towards the west, represents the north-western edge of the Indian shield (Figure 1), possessing a reasonably well-conserved rock record of nearly three billion years (~3.6 to ~0.75 Ga) of earth's evolutionary history (Deb and Sarkar, 1990; Bhushan, 1995; Sharma, 2009; Sharma and Mondal, 2019; Jain et al., 2020). The overlapping rock records, cryptic domain boundaries, and overprinted magmatic events make their spatiotemporal disposition enigmatic. Based on the accretion and reworking over time, the Precambrian tectonics and the crustal growth of the ADFB and adjoining regions are preserved. A knowledge of the crustal structure and reconstruction of spatiotemporal tectono-magmatic events enables detailed comparisons between models and observations. Some investigations using seismic (Rao et al., 2000; Krishna and Rao, 2010; Mandal et al., 2014, 2018), magnetic (Bansal and Dimri, 2005), and gravity methods (Mishra et al., 2000; Porwal et al., 2006; Naganjaneyulu and Santosh, 2012; Dwivedi et al., 2019**)** have been made to delineate the deep crustal structure across the central and northern part of the ADFB to speculate on the geodynamic evolution of northwestern India. In the southeastern part, the ADFB is bordered by the Bundelkhand massif basement, which is overlain by a sedimentary sequence of the Proterozoic Vindhyan Super Group. In certain parts, this sequence is covered by extensive Late Cretaceous Deccan volcanics. Whereas towards the west of ADFB, lies the Late Proterozoic Marwar Supergroup sequence of acidic volcanics, sedimentary succession, and the Mesozoic Jaisalmer sediments deposited in an extensional rift setting. The amalgamation of the complex geological setup is illuminated by pronounced seismicity, which is feeble in the central part and extensive towards the northern part of the ADFB **(**Figure 1**).** Unlike the central and northern parts, the southern part of the ADFB and its adjoining region lacks regional geophysical modelling of the crustal structure to understand the tectonic juxtaposition of syn- to post-tectonic orogenic events and, therefore, was chosen for the present study.

Unlike the seismic method, gravity models do not provide a unique solution. However, when constrained by seismic and other geophysical data, they yield a robust crustal structure that may represent a better litho-tectonic setup. We therefore modelled the high-resolution gravity data with constraints for the seismic structures that have been used to derive 2.5D density models of the deep crustal geometry of the southern ADFB and bordering geological units (Figure 1). We modelled the density structure of the crust across ADFB along two gravity profiles, where Profile 1 is constrained by the seismic structure of the region (Tewari et al., 1997; Krishna and Rao, 2010; Mandal et al., 2014, 2018). The crustal density structure along Profile 2 has been extended based on regional structures and the density interface from Profile 1. We aim to provide (i) a detailed 2.5D crustal density structure across the three tectonic domains, and examine a possible evolutionary and geodynamic link between the mafic and ultramafic rocks on the surface as well as in the deep crust.

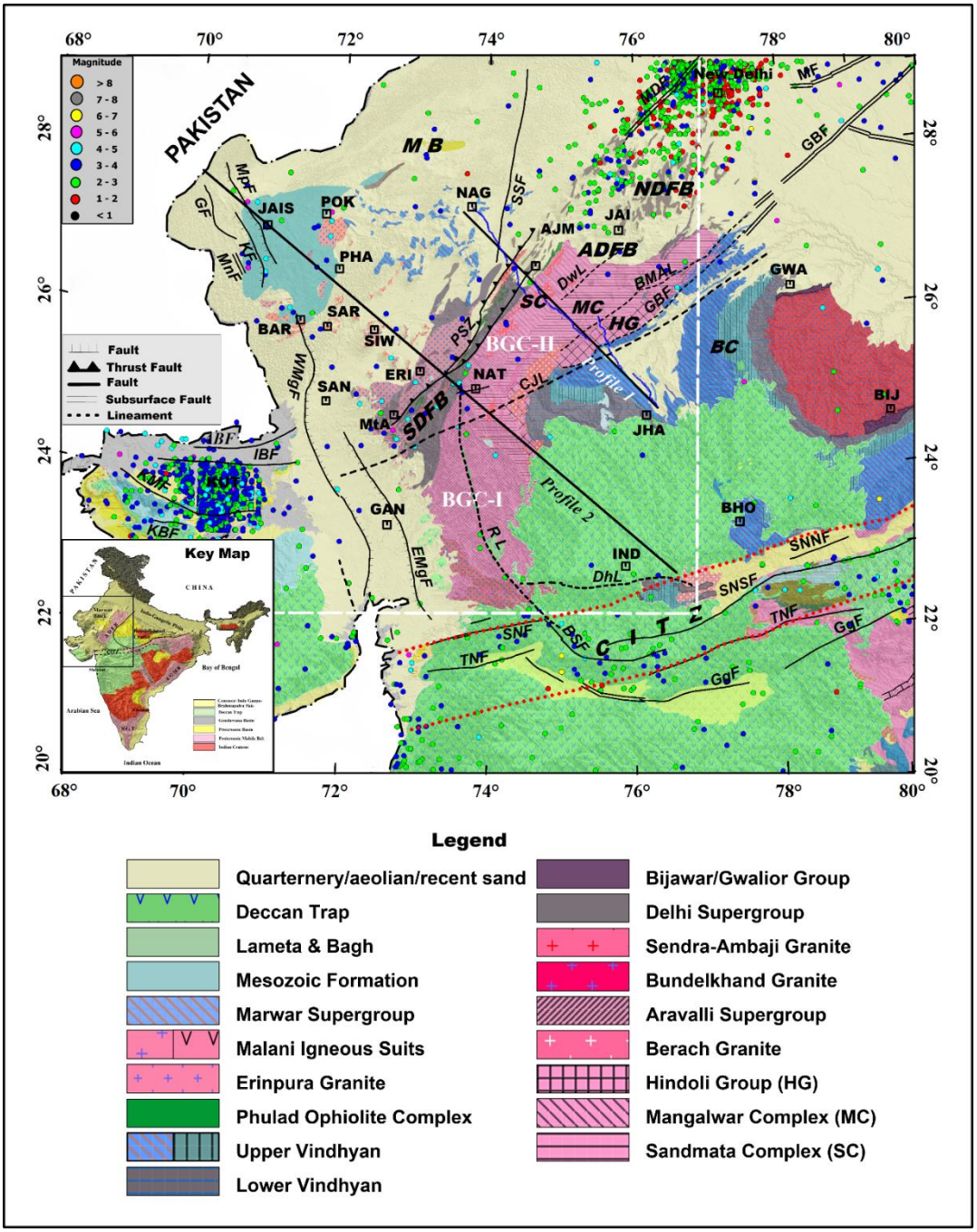

Figure 1. Generalised geology (GSI, 1998) and tectonic map (GSI, 2000) of north-western India encompassing Bundelkhand craton, Aravalli-Delhi Fold Belt, and Marwar block. Location of the seismic line (in blue) along with two gravity profiles selected for 2.5D density modelling across the ADFB (Figs. 4 and 5) is also shown. White dashed lines mark the study area. Abbreviations used for places are AJM: Ajmer, BAR: Barmer, BHO: Bhopal, BIJ: Bijawar; ERI: Erinpura; GAN: Gandhi Nagar, GWA: Gwalior, IND: Indore, JAI: Jaipur, JAIS: Jaisalmer, JHA: Jhalawar, KUT: Kutch, MtA: Mount Abu; NAG: Nagaur, NAT: Nathdwara, PHA: Phalsund, POK: Pokharan, SAN: Sanchore, SAR: Saranu, SAU: Saurashtra. Abbreviations used for geological/tectonic provinces are ADFB: Aravalli-Delhi Fold Belt; BC: Bundelkhand craton; CITZ: Central Indian Tectonic Zone; HG: Hindoli Group of rocks; MB: Marwar block; MC: Mangalwar Complex; NDFB: North Delhi Fold Belt; SDFB: South Delhi Fold Belt. BGC-I and BGC-II are the Banded Gneissic Complex of ADFB. Abbreviations used for faults and lineaments are ABF: Allah Bund Fault, BMAL: Bharatpur-Mount Abu Lineament, CJL: Chambal-Jahazpur Lineament; BSF: Barwani Sukta Fault, DhL: Dhar Lineament, DwL: Delwara Lineament, EMgF: Eastern Marginal Fault, GBF: Great Boundary Fault, GF: Ghotaro Fault, GgF: Gawaligarh Fault, IBF: Island Belt Fault, KBF: Katrot Bhuj Fault; KF: Kantli Fault, KMF: Kutch Mainland Fault; KF: Konoi Fault, MDF: Mahendragarh-Dehradun Fault, MnF: Manshuriyan Fault, MpF: Manpiya Fault, PSZ: Phulad Shear Zone, RL: Rakhabdev Lineament, SNF: Son-Narmada Fault, SNNF: Son-Narmada Narth Fault, SNSF: Son-Narmada South Fault, WMgF: Western Marginal Fault. Igneous rocks are the Deccan Traps, Malani Igneous Suite, Rakhabdev Ultramafic Suite, and Phulad Ophiolite Complex.

REGIONAL GEOLOGY

The North-western Indian craton is a collage of three tectonic domains, namely the Bundelkhand craton, the Marwar block and the Aravalli-Delhi Fold Belt (Figure 1), all of which preserve the records of crustal evolution from Archaean to Neoproterozoic that involved multiple accretion and syn- to post-tectonic magmatic events (Sharma, 2009; Sharma and Mondal, 2019; Pandey, 2020).

Bundelkhand craton

The Bundelkhand craton, also known as the Bundelkhand Granite Massif or Bundelkhand Granitoid Complex, comprises granitic gneiss complexes of Archaean age (Figure 1). The craton is divided into three discrete litho-tectonic units: (i) ~3.5 Ga highly deformed gneiss-greenstone assemblages; (ii) ~2.5 Ga undeformed multiphase granitoid plutons; and (iii) mafic dyke swarms and other intrusions (Basu, 1986; Sharma and Rahman, 2000). The Bundelkhand craton is traversed by younger mafic dykes trending NW-SE, ENE-WSW, and NE-SW directions (Pati and Singh, 2020). The Bijawar and Gwalior basins (1.8-1.9 Ga) represent two isolated and narrow peripheral basins, where sediment deposition occurred over the Bundelkhand cratonic basement. The extensive Proterozoic sedimentation over the Bundelkhand craton continued with two distinct sequences of the Lower (1.6-1.9 Ga) and the Upper Vindhyan Supergroups (0.9-1.075 Ga) (Deb et al., 2002), which are unconformably overlain by the Neogene Himalayan foreland alluvium of the Ganga basin towards the north and the Deccan volcanics towards the southwest. The Great Boundary Fault separates the Bundelkhand craton from the ADFB (**Figure 1**) (Naqvi and Rogers, 1987; Sinha-Roy, 2000).

Aravalli-Delhi Fold Belt

Aravalli-Delhi Fold Belt (ADFB), extending between the Son-Narmada graben and the Central Indian Tectonic Zone to the Indo-Gangetic plain, is a collage of three Proterozoic fold belts with distinct evolutionary history (Figure 1). The Archaean Aravalli Complex towards the east and the Meso-Neoproterozoic Delhi Complex towards the west (Mondal, 2019; Jain et al., 2020; Ghosh et al., 2023). The Aravalli Supergroup is subdivided into Banded Gneissic Complex-I (BGC-I) towards the east and southeast and BGC-II towards the north of the Nathdwara. BGC-II is constituted of the Sandamata Complex towards the west and the Mangalwar Complex towards the east (Ahmad et al., 2018). The Archaean Sandamata Complex is situated in the middle of the ADFB, flanked by the Paleoproterozoic Mangalwar Complex towards the east and the Meso-Neoproterozoic Delhi Complex towards the west (Mondal, 2019; Jain et al., 2020). The western contact of the Sandamata Complex with the Delhi Complex is distinguished by an NNE-SSW trending sub-vertical to steeply southeast-dipping Mylonitic tectonic mélange zone, whereas the eastern contact with the Mangalwar Complex is marked by the Delwara dislocation (shear) zone (Sinha-Roy and Malhotra, 1989).

The prevailing rock records encapsulated in these three major blocks of ADFB have a distinct history of evolution and mineralisation (Bhowmik and Dasgupta, 2012; Fareeduddin and Banerjee, 2020). The ADFB evolved out of episodic oceanic crust-continent interactions within the craton under ensialic regimes from the Early Archaean (ca. ~3.5 Ga) to Neoproterozoic (ca. ~0.75 Ga) (Sinha-Roy et al., 1995; Sharma, 2009; Bhowmik and Dasgupta, 2012). The evolution of the Proterozoic ADFB started with a phase of extension at about 2.15 Ga ago and was completed following the accretion of crustal blocks by 1.15 Ga ago (Sinha-Roy, 1988; Roy, 1990; Sugden et al., 1990; Sharma, 2009; Bhowmik and Dasgupta, 2012).

Marwar block

The volcano-sedimentary sequence of the Marwar block is constituted of the silicic lavas (sporadically bimodal at the base), granite, and felsic and mafic dykes of the Neoproterozoic Malani Igneous Suite, which rest unconformably on the Delhi Supergroup (Pandit et al., 1999; Bhushan, 2000). The Phulad Shear Zone represents the suture along which patchily deformed Neoproterozoic granitoids of the Marwar block accreted to the ADFB (Chatterjee et al., 2017). The epilogue of the tectonic evolution was marked by profuse granitic activity at 1015 ± 4.4 Ma and 966 ± 3.5 Ma, especially around Erinpura and Mt. Abu along the junction of the Marwar block-south Delhi Fold Belt (Dharma Rao et al., 2013). The Pokharan boulder bed of the Vendian age and the Ediacaran to Cambrian Marwar Supergroup red-bed and evaporitic sequences were deposited over the Malani Igneous Suite rocks after a hiatus (Torsvik et al., 2001). The Mesozoic Gondwana fragmentation led to the development of the Jaisalmer, Barmer, and Bikaner-Nagaur basins during the Jurassic, which are now covered by widespread Quaternary sediments and wind-blown dunes of the Thar Desert (Figure 1).

Tectonic evolution

The evolution and accretionary history of the crustal growth of various micro-blocks of the northwestern Indian craton (Marwar-ADFB-Bundelkhand) is variously debated (Bhowmik and Dasgupta, 2012; Fareeduddin and Banerjee, 2020). The notable tectono-magmatic and metamorphic episodes in the ADFB are typified by the Banded Gneissic Complex (BGC) (ca. 3.0 Ga), the Aravalli orogeny (ca. 1.8 Ga) towards the east, the Delhi orogeny (ca. 1.1 Ga) towards the west, and post-Delhi silicic magmatism (ca. 0.85-0.75 Ga) of

Malani Igneous Suite (Dharma Rao et al., 2013). The Neoproterozoic time interval (1.1-0.9 Ga) represents the amalgamation of the Rodinia supercontinent, which broke up 0.75-0.63 Ga ago (Meert et al., 2013). The Phulad granite is considered as a stitching pluton during this suturing at 0.81-0.82 Ga (Chatterjee et al., 2020). The post-tectonic bimodal magmatic event, namely the Malani Igneous Suite in the Marwar block, took place about 0.77-0.75 Ga ago (Gregory et al., 2009; Ashwal et al., 2013; de Wall et al., 2018; Wang et al., 2018). The intervening granites have yielded an age of ~0.735 Ga, indicating a brief magmatic event in the region.

GRAVITY DATA

For the understanding of the Proterozoic tectono-magmatic signatures, a complete Bouguer anomaly map of the region has been prepared from 8504-station data at ~5 km intervals (which was used to prepare the gravity map series of India, GSI-NGRI, 2006), 441 gravity data recorded at a station interval of about 1 km along the Nagaur-Jhalawar profile (Profile 1) (Mishra et al., 2000), and an additional 2525 station gravity data acquired at an interval of about 2-3 km over the Malani Igneous Suite (Prakash et al., 2020) (Figure 2). Gravity readings of all three data sets were tied to an available absolute gravity base at Sheo (Qureshy and Warsi, 1972), and the Geodetic Reference System 1980 was used to compute normal (theoretical) gravity in the procedure to reduce the observed gravity data to Bouguer anomalies. A crustal density of 2.67 g/cm^3 was used for the Bouguer and terrain corrections (Hinze et al., 2013).

The amplitude of the Bouguer anomaly ranges from +52 to -92 mGal in the studied regions, with a long linear gravity 'high' (+5 mGal) seen over the high relief region of the ADFB. A positive gravity anomaly over ADFB is an unusual feature, as the elevated region is typically expected to have a negative Bouguer anomaly due to isostatic compensation of the topography. The positive Bouguer gravity anomaly was earlier interpreted as a horst-like feature in the basement at a depth of over 11 km (Reddi and Ramakrishna, 1988a, b).

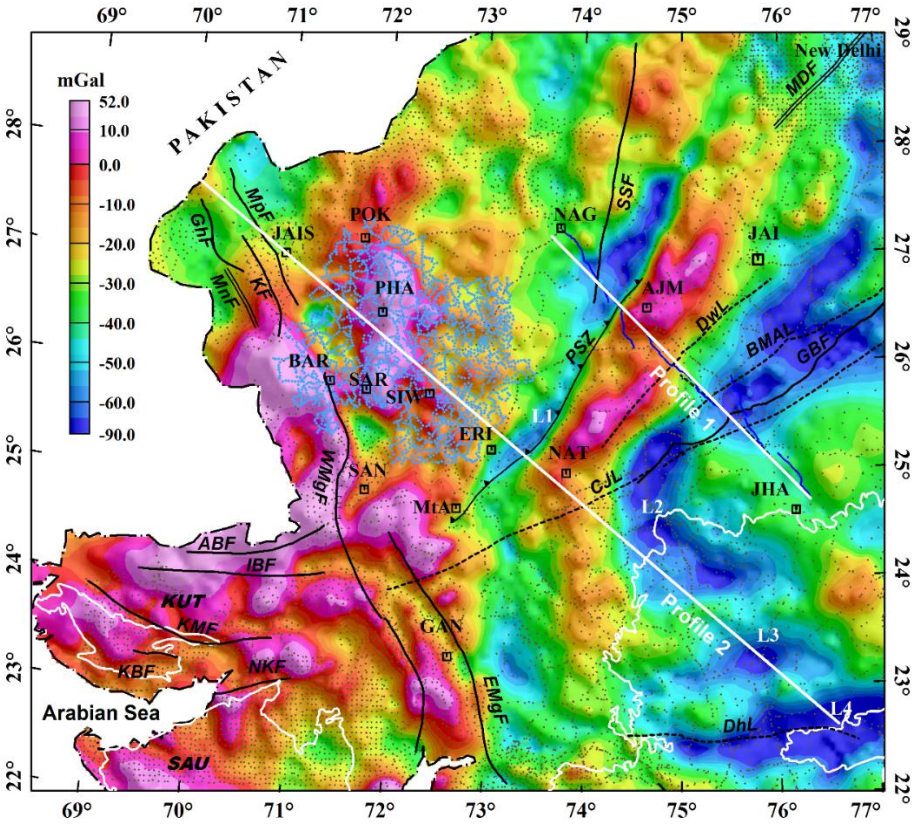

Figure 2. Complete Bouguer anomaly map (in mGal) of north-western India is based on more than 11470 terrestrial gravity station data points indicated by light black (8504 old gravity data points from GSI-NGRI 2006), dark blue (441 old gravity data points, collected along the Nagaur-Jhalawar seismic profile, from Mishra et al. 2000), and light blue stars (2525 new data points from Prakash et al. 2020). The flanking lows (L1 and L2) of -60 mGal on either side of the Aravalli-Delhi Fold Belt coincide with the Erinpura granite and Marwar supergroup towards the west and the Berach granite and Hindoli group of rocks towards the east. Gravity lows L3 and L4 are located over the trap-covered Vindhyan basin. White lines indicate profile locations along which vertical density cross-sections across the Aravalli-Delhi Fold Belt are modelled (shown in Figures 4 and 5). NKF: North Kathiawar Fault. Other abbreviations are the same as those given in **Figure 1.**

In contrast, Qureshy (1971) opined that the source of high gravity must be rooted deep in the crust, possibly in the high-density intruded mafic mantle material in the upper crust, which caused the Aravalli uplift (Qureshy, 1981). Recent seismic studies, however, rule out the possibility of a high-density inhomogeneity at shallow depths (Tewari et al., 1997; Krishna and Rao, 2010).

Based on the observed high seismic velocity (V_p=7.3 km/s), a high-density igneous body at the base of the crust was proposed as a source for the high gravity anomaly over the ADFB (Mishra et al., 2000; Kumar et al., 2020). The flanking gravity lows (L1 and L2) of amplitude -60 mGal on either side of the ADFB gravity high (Figure 2) coincide with the Ambaji/ Erinpura granite to the west and the Berach granite and Hindoli Group rocks to the east. The steep gravity gradients are interpreted to represent the deep crustal breaks, which channeled the syenites and Phulad granites in the region. According to Mishra et al. (2000), the steep gradient between the central high and the contiguous lows to either side indicates faulted contacts of the ADFB with the Marwar block to the west and the Bundelkhand craton to the east.

The range of Bouguer anomaly within the Marwar block varies from +52 to -60 mGal (Figure 2), indicating a broad association with the exposed litho-units (Figure 1). For example, the most notable north-south trending gravity high of peak value +52 mGal centred over the Saranu-Phalsund-Pokharan region and a gravity high of peak value +40 mGal to the west of Barmer encompassing the Malani Igneous Suite (Prakash et al., 2020). Another short-wavelength positive Bouguer anomaly attaining a peak value of +11 mGal is positioned at the eastern margin of the Siwana Ring Complex. Several dispersed gravity-high anomaly peaks, which have various trends that do not show any apparent association with the exposed geology, may be related to the basement highs or ridges (Dutta, 1983). Another interpretation is that many of these gravity highs are caused by ascending lower crust or upper mantle magmatic rocks (Krishna Brahmam, 1993; Roy, 2003). The SE-NW trending gravity low in the Sanchore-Barmer-Jaisalmer basins suggests they are interconnected with the Cambay graben to the south (Krishna Brahmam, 1993). Other significant gravity lows in the Marwar block, which descend to -20 to -25 mGal in areas where no plausible geological body is exposed, may indicate the presence of subsurface granites (Reddi and Ramakrishna, 1988a, b).

The Bouguer anomaly over the western part of the Bundelkhand craton varies from -10 to -92 mGal. The gravity high around Jhalawar and radiating in the south-west, west, and north-west directions corresponds with the ENE-WSW Central India Tectonic Zone, and Deccan Traps may be associated with sub-trappean high-density Bijawar Group (comprising meta-sediments with basic/ultra-basic intrusive) (Mishra and Ravikumar, 2014). The high gravity could also be attributed to lower Proterozoic volcanic deposits beneath the Vindhyan sediments (Qureshy and Warsi, 1975). The curvilinear gravity low (L2) encompasses the Berach granite, Hindoli Group, and the Vindhyan sediments. In contrast, the gravity lows (L3 and L4) around the Indore region may be due to subtrappean Vindhyan sediments. The geometries of various density inhomogeneities in the Bouguer anomaly map, produced by the Proterozoic tectono-magmatic events, are modelled by a 2.5D crustal density structure along two gravity profiles (Figure 2).

Density variation

The geometry, depth, and density of the causative body are the major factors that govern the inherent ambiguity in gravity modelling. The available densities of the major lithologies exposed in the study area, and their laboratory-measured densities, are listed in Table 1. The densities of the majority of the Archaean and Proterozoic formations that overlie the BGC, acting as the basement of the ADBF, are variable, ranging from 2.65 to 2.75 g/cm³. Granitic rocks on the western flanks of the ADFB, including Ambaji/ Erinpura granites, have a density of 2.62 g/cm^3. In contrast, the density of the Precambrian Phulad formation, which may represent the basic volcanic of an ophiolite mélange, is higher than the densities of other granites (Mishra et al., 2000, and references therein). Low but variable density values characterise the Siwana granite (2.57-2.77 g/cm^3), Jalore granite (2.48-2.61 g/cm^3), and Malani rhyolite (2.43-2.86 g/cm^3), whereas high-density values (2.70-2.75 g/cm^3) characterise the Siwana rhyolite (Table 1) (Prakash et al., 2020). The density variation in different granitic samples probably arises from differences in the proportion of minerals and the phase transformation of minerals during metamorphism, a common phenomenon in metamorphic processes during orogenesis. Rocks with the same chemical composition can exhibit significant variations in density due to differences in the pressure they experience.

In the Marwar block, we divide the early Oligocene deposits into the Marwar supergroup (comprising sandstone, shale, limestone, and evaporites) with a density of 2.30 g/cm^3 and an upper sand and soil unit with a density of 2.0 g/cm^3 (Prakash et al., 2020). Proterozoic sediments in the Vindhyan Basin are sub-divided into a Lower Vindhyan sequence (2.85 g/cm^3) and an Upper Vindhyan sequence (2.55 g/cm^3) in the southern part of the graben (Das et al., 2007). Due to its mafic composition, the Bijawar Group of rocks has a higher density (2.85-2.95 g/cm^3) than the sediments of the Vindhyan Supergroup (Kailasam, 1976; Das et al., 2007). The relatively thin Bagh Group of rocks in the Vindhyan Basin has a density of about

2.35-2.40 g/cm^3 (Das et al., 2007). The Deccan Trap on the surface is allocated a density of 2.78 g/cm^3 (Prasad et al., 2018, 2021). The seismic velocities observed along the Nagaur-Jhalawar Profile-I (Tewari et al., 1997; Krishna and Rao, 2010; Rao and Krishna, 2013) are used to constrain the sub-surface density distribution of associated crustal layers (Figure 3) (Barton, 1986).

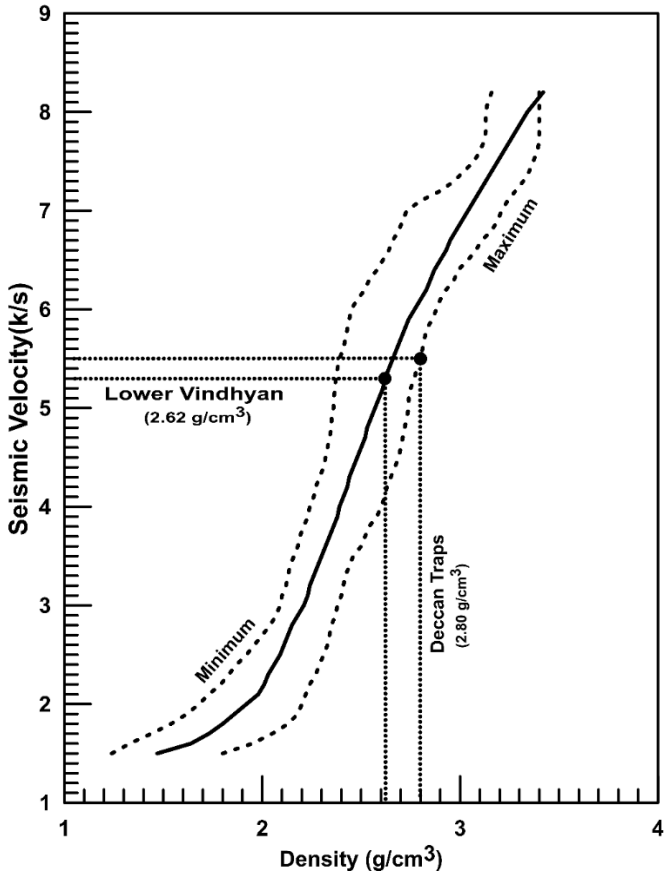

Figure 3. The relationship between seismic velocities and the densities of rocks, as given by Barton (1986).

Table 1. Measured density values of some of the intrusive rock formations. The older rock of ADFB appears to have overlapping density values. However, their histogram suggests that the maximum number of samples lies in the range of 2.65 to 2.70 g/cm^3.

Rock type	No. of sample	Density (g/cm^3)	Source	Density used (g/cm^3)
Malani rhyolite	21	2.43-2.86	Prakash et al. (2020)	2.62
ADFB granite	--	2.40-2.60	Ramakrishna and Rao (1981)	2.62
Lameta / Bagh bed	--	2.35-2.40	Das et al. (2007)	2.40
Upper Vindhyan	--	2.55	Das et al. (2007)	2.55
Lower Vindhyan	--	2.62	Barton (1986)	2.62
Erinpura granite	--	2.60-2.65	Mishra et al. (2000)	2.62
Deccan Traps	--	2.65-2.80	Prasad et al. (2018)	2.80
Bijawar	--	2.80-2.95	Das et al. (2007)	2.85
Middle crust	--	2.80	--	2.80
Lower crust	--	2.90-2.95	--	2.89
Underplated layer	--	3.0-3.1	--	3.05
Upper mantle	--	3.30	--	3.30

GRAVITY MODELLING

Nagaur-Jhalawar (Profile-I)

A wide-angle reflection seismic profile along the Nagaur-Jhalawar transect (Figures 1 and 2), which cuts across the ADFB, was acquired between 1991 and 1993 (Tewari et al., 1997). The seismic refraction/ wide-angle reflection data (Tewari et al., 1997; Krishna and Rao, 2010) imaged an imbricated crustal structure with ~38-40 km deep reflective Moho under the Marwar block (Figure 4) (Mandal et al., 2014). The Moho could not be identified beneath the ADFB due to poor reflectivity in the seismic images at the expected depth of investigations (Tewari et al., 1997; Mandal et al., 2014), and the crustal thickness was estimated to be between 45 and 50 km across the ADFB. The high-velocity (7.3 km/s) laminar lower crustal layers with a total thickness of ~10-12 km, covering both the Delhi and Sandamata complexes, are conjectured to signify the possible presence of mafic intrusions (Tewari et al., 1997; Mandal et al., 2014). The P_{MS} interface, observed at 29 km depth beneath the Ajmer broadband station, is also reported to be the top of the anomalous high-velocity layer (Ravi Kumar et al., 2001). The reprocessed seismic data, together with the synthetic seismogram modelling of the reflected phases, have delineated a lamellar structure overlying the Moho at a depth of ~ 46±1 km underneath the ADFB (Krishna and Rao, 2010), and also the crustal-scale south Delhi Thrust dipping in 25°-30° SE direction. The common reflection surface study imaged the Jahazpur Thrust under the Sandamata Complex, which becomes listric at the Moho (Mandal et al., 2014). An NW-dipping Chambal Thrust has been imaged from 9- to 30-km depth under the Bundi-Kota segment (Mandal et al., 2018). The depth-migrated seismic section delineated the Moho structure in the Vindhyan Basin reveals a crustal thickness ranging from 40 to 44 km towards the east (Mandal et al., 2018).

Projection of the seismic layers (Figure 4) onto the gravity profile extracted along a straight line from the gravity anomaly map (Figure 2) shows that the significant seismic reflectors correlate with the major gravity features (Figure 5). We completed 2.5D forward modelling of the gravity data along the reprocessed seismic section of Mandal et al. (2014, 2018). Gravity data at an equal interval of 2 km were extracted along a straight profile (Profile 1) from the composite gravity map (Figure 2). The *a priori* model geometry is extended in both directions by 10000 km to avoid the edge effects. Initially, minor modifications are made to the density and geometry of the *a priori* crustal density model. To arrive at the final crustal density model, which is similar to the seismic model and generates a response matching the observed gravity anomalies, a couple of small mafic bodies are also inserted (Figure 5).

On the western flank of the ADFB, the gravity low (L1) is partly modelled as Ambaji granite in the Delhi/ Marwar block. The Marwar block towards the west is apparently the major source of the low L1, which is modelled in terms of Quaternary sand, soil, and Oligocene Marwar supergroup (2.30 g/cm^3) near the surface, below which is the Malani Igneous Suite (2.62 g/cm^3) that lies above the Delhi Supergroup as the basement. Although the succession beneath the Erinpura/ Ambaji granite in the Marwar block is seismically transparent, gravity modelling suggests that the granites (density 2.62 g/cm^3) extend up to ~10.5 km in depth. The Delhi Supergroup, Sandmata granulitic complex, and Mangalwar complex of the ADFB also extend to a similar depth of ~10.5 km. Based on the mapped surface geology (e.g., granulites) and given tectono-magmatic events (e.g., basic volcanic of an ophiolite mélange) (Sinha-Roy et al., 1995; Mishra et al., 2000), a couple of high-density intrusive rock units are inserted in ADFB to match the short-wavelength gravity anomalies. The Hindoli Group of rocks (ρ=2.68 g/cm^3) of the ADFB is modelled as a thin tabular body reaching up to a depth of ~9 km.

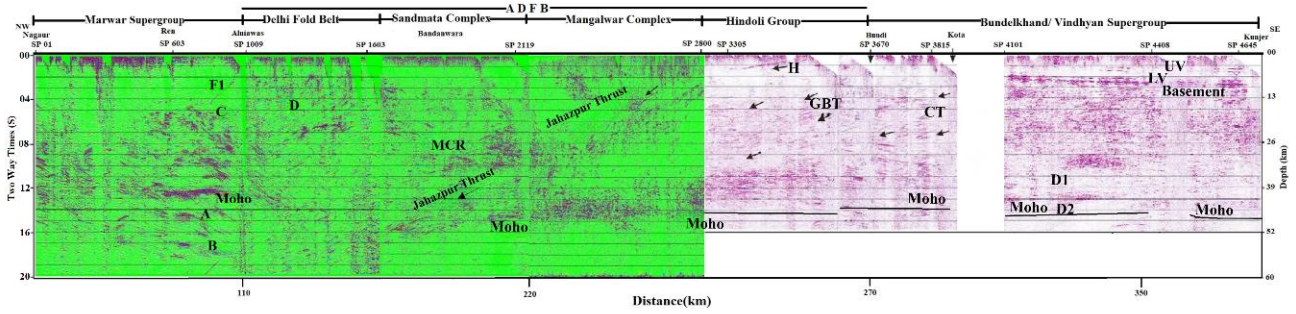

Figure 4. Common reflection surface stack section of the Marwar Basin- ADFB-Vindhyan Basin along the seismic line "Nagaur-Jhalawar Profile-I" (modified after Mandal et al., 2014, 2018). 'A' and 'B' represent the sub-crustal reflections beneath the Marwar block. MCR: mid-crustal reflectors in ADFB, GBT: Great Boundary Thrust, CT: Chambal Thrust. Moho and Jahazpur faults are also shown for ready reference; 'C' and 'D' represent oppositely dipping reflections, and F1 represents the boundary fault. 'A' and 'B' represent upper mantle reflections; UV = Upper Vindhyan sediments (650-1100 Ma); LV = Lower Vindhyan sediments (1100-1700 Ma); D1 and D2 are two diffraction tails; Shallow reflector-H represents the basement for the Hindoli group of rocks.

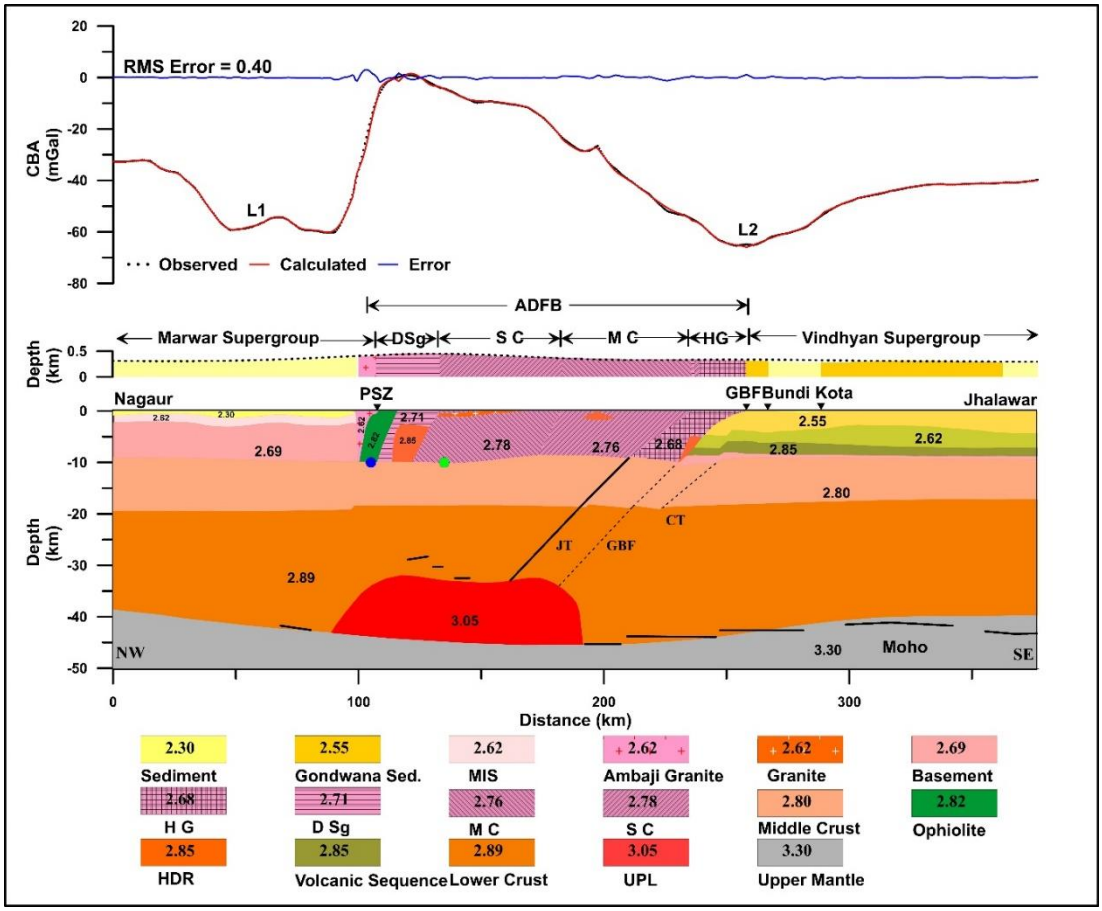

Figure 5. 2.5D crustal density (in g/cm^3) structure along the Nagur-Jhalawar seismic Profile-I, keeping our model as close as possible to the seismic constraints used. A high-density (3.05 g/cm^3) lower crustal body in ADFB is modelled at the base of the crust. The extent of the Marwar block, ADFB, and Bundelkhand craton is displayed on topography. Thick black solid lines indicate the seismically defined Moho, high-velocity layer (7.3 km/s), and Jahazpur thrust (JT). Abbreviations are the same as those given in Figure 1. Note the change in the exaggeration of the vertical scale at sea level.

The rocks of the Hindoli Group are described as granite-andesite in composition with a lower density of 2.68 g/cm^3, which explains the Bouguer gravity low (L2). A maximum depth of 6-7 km is modelled for the Upper Vindhyan rocks, a thickness of ~1.5 km is modelled for the Lower Vindhyan rocks, and the granitic gneiss basement is at a depth of 9.0 km (Figure 5). The cumulative thickness of the Lower Vindhyan is estimated to be ~1.7 km (Soni et al., 1987; Mandal et al., 2018).

The gravity modelling along Profile-I indicates considerable inhomogeneity in the upper crust due to lithological variation in different crustal blocks. The deeper layers of the modelled crustal density structure conform to the seismic section. Besides the Jahazpur thrust, the NW-dipping Great Boundary thrust to the west of Bundi and another subsurface Chambal fault to the east of Bundi are modelled up to the basement depth. The modelled crustal thickness in the Marwar block varies from ~39 km at Nagaur to ~42 km close to the ADFB zone. In the highly elevated ADFB area, the crust has a thickness of approximately 45 km, including a ~13 km thick high-density layer at its base. The crustal thickness beneath the Vindhyan Basin is ~42 km, and the lower crust has a uniform density, suggesting that its composition is homogeneous.

Jaisalmer-Indore (Profile-II)

The second gravity profile, chosen parallel to the first one, passes through the Malani Igneous Suite of the Marwar block, and the Deccan Traps covered the Vindhyan Basin of the Bundelkhand craton (Figure 1). The second most seismically active region after Delhi is covered in this profile. A layered crustal structure, similar to Nagaur-Jhalawar seismic Profile-I, is assumed across the ADFB. Additional information, such as seismic (Kumar et al., 2000), seismological (Sharma et al., 2018), MT (Nagajaneyuly and Santosh, 2012), and gravity (Mishra and Ravikumar, 2014; Prakash et al., 2020), is used to constrain the modelling in the two flanking cratonic regions. In addition to laboratory measurements to obtain density values of exposed Malani volcanic rocks, a few measured density values in the literature (Table 1) are assigned to the local geological units accordingly. An initial geometry of the crustal

structure is inserted into the GMSYS (Geosoft, 2015) modelling program, and the calculated response is compared with the Bouguer anomaly observed along this profile. Portions of the initial geometry and average densities assigned to new geological bodies were then varied in order to achieve a match of the model gravity response with the observed Bouguer anomaly. A few geologically and tectonically reasonable concealed bodies of small wavelengths were added again to minimise the RMS error. The results of 2.5D density modelling of the Bouguer anomaly to determine the deep crustal structure across the three tectonic domains are shown in Figure 6. The RMS error between the observed and calculated model response is < 0.7 mGal, implying that the *a priori* model, based on the model derived along the neighbouring Profile-I, provides reasonable constraints for gravity modelling. Several significant features have been recognised from both the inferred gravity models (Figures 4 and 5).

DISCUSSION

Shallow crustal structure

The seismic section down to the granite-gneiss basement depth at the eastern end of the profile consists of four layers: a ~500 m thick Deccan Traps and another ~400 m thick Mesozoic sediments with an average velocity of 3.7 km/s (Kaila et al., 1985). It is followed by approximately 1.5 km of Vindhyan sediment and 5 km of Bijawar metasediments. Initially, the gravity low (L4) was interpreted to be caused by the subtrappean Vindhyan sediments overlying the Archaean basement (Nayak et al., 1986). This possibility was later ruled out based on the observed velocity of the subtrappean layer and the exposed Vindhyan sediments (Kumar et al., 2000). For the given layer thickness, an optimal density value of 2.36 g/cm^3 was suggested to match the observed gravity anomaly (Singh and Meissner, 1995). Given that the measured density of even Upper Vindhyan sediments is 2.55 g/cm^3, the inverted density (2.36 g/cm^3) possibly indicates a 500 m thick low-density sedimentary layer of Lameta or Bagh beds (Das et al., 2007) exposed in nearby regions (Figure 1). Though no seismic control is available to help constrain modelling of the adjoining gravity low (L3), the presence of the same low-density sedimentary layer can be a possible explanation. The two relative gravity highs in the eastern segment of the profile necessitate the presence of a high-density mafic body. The two gravity highs are attributed to the subtrappean Bijawar Group, which comprises meta-sediments with basic/ultra-basic intrusives (Mishra and Ravikumar, 2014). A thin (200-400 m) layer of upper and lower Vindhyan sediment is modelled throughout this region (Kumar et al., 2000).

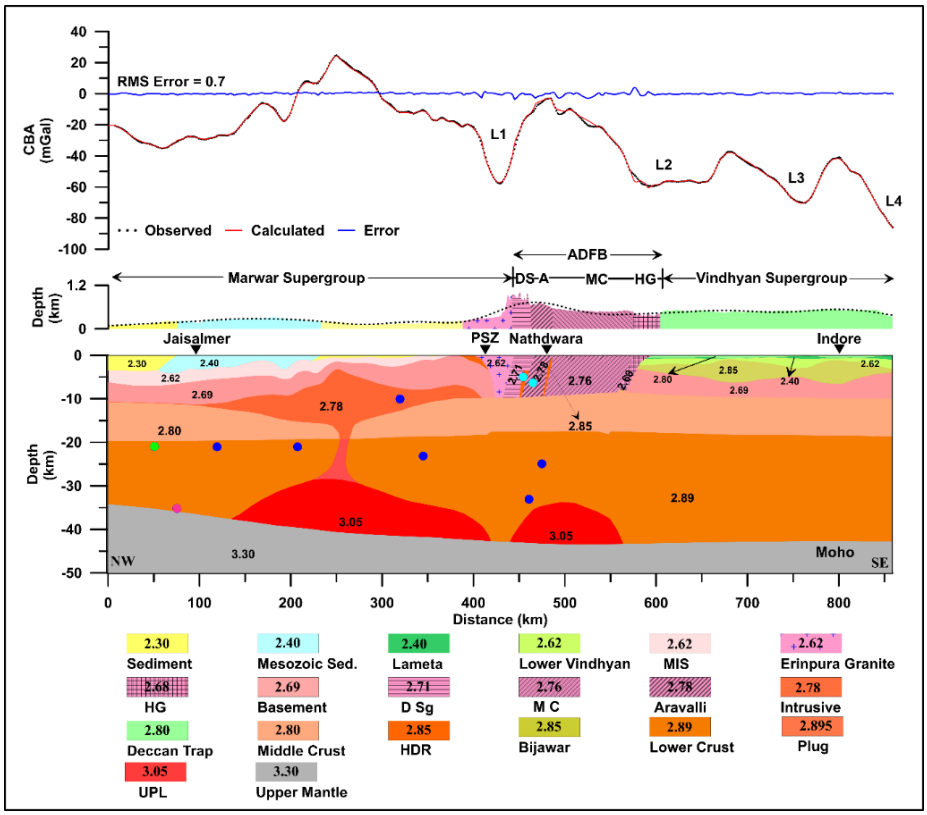

FIGURE 6. 2.5D crustal density (in g/cm^3) structure modelled along the Jaisalmer-Indore Profile-II. Two high-density bodies at the base of the crust beneath the Marwar block and ADFB, respectively, are modelled. The extent of the Marwar block, ADFB, and the Bundelkhand craton is displayed on topography. For abbreviations, see Figure 1. Note the change in the exaggeration of the vertical scale at sea level.

The near-surface crust under the ADFB has been modelled as several metasedimentary blocks extending to depths of about 9.4-10.8 km (Figures 4 and 5). A number of basic rocks in these metasedimentary sub-blocks may also be inferred, which increases the mean density to a maximum of ~2.78 g/cm^3. Our model further demonstrates that the sub-blocks of ADFB and its sub-vertical western boundary with the Marwar block dip steeply towards the west. The magmatic sills/dykes that intruded into the metasedimentary formations of various sub-blocks extend to a depth of 2 to 9 km (Figures 4 and 5).

The low gravity anomaly (L1) over the Marwar block indicates the presence of a sizeable felsic body underneath the Sendra-Ambaji (Mesoproterozoic)/ Erinpura-Phulad (Neoproterozoic) granite to the west of ADFB (Figure 6). Our gravity modeling suggests that these felsic bodies have a typical density of 2.62 g/cm³, which may indicate a granite-dacite composition. The modelled granite body is a rootless, tabular body extending to a depth of ~10 km, and its margins dip steeply inward. Malani Rhyolites, exposed in the Marwar block, are best represented as a thin layer (of density 2.62 g/cm^3) with a maximum thickness of ~3.0 km overlying the high-density (2.69 g/cm^3) basement rocks of the Delhi Fold Belt. A particularly interesting feature of the model in this area is a 6-8 km thick high-density (2.78 g/cm^3) lens-shaped body that significantly contributes to the high Bouguer gravity anomaly (Figure 6). This body of probable intermediate to mafic composition emplaced in the upper crust may be a product of early magmatic activity associated with the Malani Igneous Suite (Prakash et al., 2020, and references therein).

Deep crustal structure and Moho geometry

Along the Nagaur-Jhalawar Profile-I, a 10-12 km thick high-velocity (V_p = 7.30 km/s) layer at the base of the crust has been documented underneath the ADFB by seismic studies (Tewari et al., 1997; Mandal et al., 2014). The P_{MS} interface observed at a depth of 29 km beneath the Ajmer broadband station is also reported to be the top of the atypical crustal layer (Ravi Kumar et al., 2001). Gravity modelling along this seismic profile also indicates a thick crust (~45 km) and a high-density (3.05 g/cm^3) dome-shaped body above the Moho zone (Figure 5). A high-velocity (7.3 km/s)/density (3.05 g/cm^3) layer in the lower crust with a seismically transparent upper mantle may be characteristic of magmatic underplating above the Moho (Thybo and Artemieva, 2013). However, without sufficient seismic refraction profiles, it is challenging to determine the lateral extension of the high-velocity body under the ADFB or ascertain its spatial distribution in the adjoining Marwar block. Our gravity modelling of Profile 2 establishes that the high-density (3.05 g/cm^3) mafic body in the lower crust persists from the central up to the southern part of the ADFB (Figure 6). A similar body was also modelled in the gravity profile with increasing Moho depth towards the northern extension of the ADFB (Dwivedi et al., 2019). The crustal configuration derived by inverting regionalised group velocity dispersion data (Sharma et al., 2018) in the Saurashtra region indicates an almost flat Moho lying at about 37-39 km depth in the south of the ADFB. The thick crust (~45 km) with abnormally high Vp (7.30 km/s) in the central part of ADFB was hypothesised as crustal thickening through magmatic underplating and fractionation of basaltic mantle magma (Mandal et al., 2014).

The crust in the adjoining tectonic domains, the Marwar block and the Bundelkhand craton, is characterised by typical Moho geometry with no signatures of modification along Profile-I. Despite the Deccan basalt at the surface, the crust beneath the Bundelkhand craton remains unmodified along Profile 2. However, a significant amount of crustal modification through ascending parent Malani Igneous Suite magma (of density 3.05 g/cm^3) is observed to accumulate in the lower crust, forming a deep crustal mush zone, some of which then ascended to a shallow depth in the Marwar block to feed the Malani Igneous Suite extrusion. The derived crustal density structures indicate high-density magmatic infiltration from the mantle into the lower crust at two discrete locales with distinct tectonic settings for the crustal modifications, namely beneath the orogenic belt of ADFB and the intraplate region of the Marwar block, where the Malani Igneous Suite is emplaced in the upper crust.

Tectonic implications of the model geometry

Accretion of the three tectonic domains and magmatic infiltration within the continental crust point towards Precambrian crustal modification and destruction, both at domain margins and intraplate regions of north-western India (Figure 7). The crustal growth of the Bundelkhand-ADFB-Marwar protocontinent began in the Archaean by rifting followed by accretion, orogenesis, and intermittent magmatism (Fareeduddin and Banerjee, 2020). The growth of ADFB is hypothesized as an outcome of either episodic oceanic crust-continent interactions or their evolution within the craton under ensialic regimes (Sinha-Roy, 1988; Sinha-Roy et al., 1995; Sharma, 2009; Bhowmik and Dasgupta, 2012; Pandey, 2020). The amalgamation of the Bundelkhand-ADFB-Marwar protocontinent started with the collision of the three blocks first along the Great Boundary Fault and subsequently along the Phulad Shear zone during the Proterozoic (Sinha-Roy et al., 1995). At the outset, the collage of the ADFB was accreted to the Bundelkhand craton along the Great Boundary Fault, up-thrusting the Mangalwar complex over the Hindoli-Jahazpur block (Sinha-Roy and Malhotra, 1989; Tewari and Kumar, 2003; Dey et al., 2019). The crustal-scale Jahazpur Thrust along the Great Boundary Fault defines the boundary of the westward subduction of the Bundelkhand craton (Mandal et al.,

2018). Similarly, the NE-SW trending Phulad Shear Zone defines the terrane boundary between the Delhi Fold Belt and the Marwar block (Chatterjee et al., 2017, 2020; de Wall et al., 2022). The SE-dipping sub-crustal reflections observed in the Trans-Aravalli regions are interpreted as a relic subduction zone (Figure 4) and indicate the continental collision between the Marwar-ADFB domains (Mandal et al., 2014). The time of accretion of the Marwar block with the ADFB-Bundelkhand protocontinent was suggested as ~1.0 Ga (Kaur et al., 2021) to >0.8 Ga (Chatterjee et al., 2017, 2020).

The sharp gravity gradients on either side of the ADFB (Figure 2) corroborate the faulted contacts with adjoining domains within the craton, which have distinct crustal structures (Mishra et al., 2000). Our model (Figures 5 and 6) supports the accretion of the Bundelkhand-ADFB-Marwar blocks as a subduction-collision complex during the early Neoproterozoic (Bhowmik and Dasgupta, 2012). The Neoproterozoic crustal shortening of the ADFB between the adjoining blocks would have resulted in the crustal thickening with an elevated topography and a deeper Moho along its strike. A reflection-free lower crust, together with a strong reflector at ~30 km on top of the high-velocity layer containing a lensoid high-density (3.05 g/cm^3) magmatic layer just above the Moho (Figures 5 and 6) under the thicker crust of the ADFB represents the imprint of sequential bivergent collision and subsequent modification by rising of hot mantle material to fill the gap as magmatic underplating in the Archaean crust during Late Neoproterozoic. A similar dynamic crustal modification occurs through high-density basaltic magmatic underplating above the Moho across the orogenic belts (Thybo and Artemieva, 2013; Mandal et al., 2014; Dwivedi et al., 2019).

In active asthenosphere melt, a significant part of the rising mantle material solidifies as an underplate at the crust base, whereas large volumes of fractionated primary magma of rhyolitic composition reach the surface through the anatectic crust (Ayalew et al. 2019; Ernst et al., 2019). The delineated high-density bodies in the Marwar block indicate that the cumulates of the primary magma associated with Malani Igneous Suite are present at two levels: namely, a high-density (3.05 g/cm^3) ultrabasic body at the Moho (34 to 40 km depth) and another of granitic density (2.78 g/cm^3) at a depth of ~9 km.

The high-density lower crustal ultramafic layer delineated in the present case is observed to occur in two distinct tectonic settings (Figure 7). To visualise the differential degree of deformation and exhumation across the components of the NW Indian craton, we plotted an average geotherm observed at the surface based on the metamorphic grade of rocks observed in the litho-tectonic unit (Figure 7). It is clear that the Archean BGC formations constitute the base of the orogenic belt. Sedimentation in the extensional regime, followed by collision and deformation during ~1.8 Ga, is observed in the Aravali belt. The granulite-amphibolite grade rocks from the lower-mid crust were exhumed until 1.4-1.3 Ga. The adjacent Vindhyan basin received sedimentation in the shallow foreland basin over the underthrusting Bundelkhand Gneissic Complex since 1.4 Ga (Raza et al., 2009), which remained undeformed since, and the basin did not experience metamorphism, possibly representing ~200°C diagenetic temperature. The locus of deformation and exhumation remained confined to the Aravali belt, with over 20 km across the Great Boundary Fault, which has remained a steeply dipping terrane boundary since then. Towards the western margin of the Aravali orogenic belt, the rocks of the Delhi Fold Belt were deposited during the early rifting phase of the Rodinia orogeny, followed by deformation and exhumation of the medium-grade metamorphic rocks from a depth of ~550°C geotherm, suggesting intense deformation. The Neoproterozoic Phulad/Erinpura granite intrusion along the Phulad Shear Zone (PSZ), west of ADFB, represents the beginning of the Rodinia dispersal, which climaxed with the emplacement of the variegated rocks of Malani Igneous Suite during ~0.75 Ga. The recent seismicity in the southern ADFB and adjoining areas represents the reactivation of an older tectonic boundary under the influence of the present plate tectonic regime, and it remains confined to shallow structures. We speculate that the lower-middle crust has stratified due to the prolonged thermal equilibration since the Neoproterozoic period, obliterating the density contrast across the orogenic root zone, though the boundary between the ADFB and Bundelkhand along the Great Boundary Fault and Jahazpur Thrust is distinctly reflected in seismic signature (Tewari et al., 1997; Mandal et al., 2014).

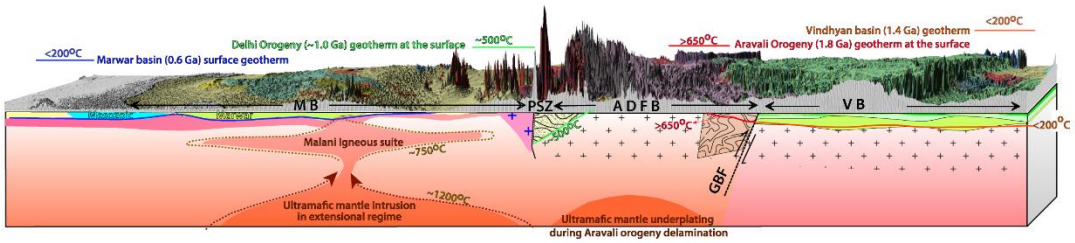

FIGURE 7. A schematic diagram for the evolution of the derived crustal density model of the Marwar-ADFB-Bundelkhand protocontinent. Abbreviations are the same as those given in **Figure 1**.

CONCLUSIONS

The Precambrian crustal growth of north-western India has involved a series of terrane accretions and modifications through mantle magmatism. The 2.5D gravity model, aided by geological and other geophysical constraints, represents the density structure of the litho-tectonic units and provides a realistic crustal structure for discussing the geodynamic evolution. The derived crustal density structure reinforces the bivergent collision hypothesis for ADFB evolution. Some major conclusions, derived from our data analysis and regional data review, are given below:

(i) The elevated ADFB has a thicker crust of ~45 km depth with a defused Moho boundary marked by the presence of a high-density magmatic mantle underplating above the Moho.

(ii) The crustal modification of the Marwar block during Late Neoproterozoic Rodinia dispersal was associated with mantle magmatic extrusion and progressive lower crustal melting, resulting in felsic rhyolitic magmatism of the Malani Igneous Suite.

(iii) The Bundelkhand craton and Vindhyan Basin, to the east of ADFB, largely remained stable with no crustal modification throughout the ADFB and Marwar block deformation.

ACKNOWLEDGEMENTS

We thank the Director, CSIR-NGRI, for his encouragement and permission to publish this work. We sincerely appreciate the colleagues of Gravity Group for the gravity data and rock sample collection, as well as the computational expertise that greatly assisted this research. We highly appreciate the insightful comments and suggestions of the learned reviewers, which helped improve the manuscript's flow and content. The acquisition of the ground gravity data was supported under CSIR-NGRI's INDEX Program (PSC-0204). The present work is part of the Ph.D. work of OP, who thanks the UGC Research Fellowship. APS acknowledges the financial support by CSIR, New Delhi, in the form of Emeritus Scientist [21(1144)22/EMR-II]. This publication is CSIR-NGRI contribution # NGRI/Lib/2020/ Pub-214.

Authors credit statement

Om Prakash: Gravity data collection, processing, modelling and making of figures; A.P. Singh: Conceptualisation, overall supervision and paper finalisation; Niraj Kumar: Gravity data collection, validation and paper draft; K.N.D. Prasad: Gravity data collection and curation, and Anand K. Pandey: Geological and geodynamic input, draft improvisation

Data Availability

Gravity data used in this study is proprietary of CSIR-National Geophysical Research Institute, Hyderabad, and governed by its data sharing policy

Compliance with ethical standards

The authors declare that they have no known competing financial interests or personal relationships that could have appeared to influence the work reported in this paper, and they adhere to copyright norms

References

Ahmad, I., Mondal, M.E.A., Bhutani, R. and Satyanarayanan, M., 2018. Geochemical evolution of the Mangalwar Complex, Aravalli Craton, NW India: insights from elemental and Nd-isotope geochemistry of the basement gneisses. Geosci. Front., 9(3), 931-942.

Ashwal, L.D., Solanki, A.M., Pandit, M.K., Corfu, F., Hendriks, B.W.H., Burke, K. and Torsvik, T.H., 2013. Geochronology and geochemistry of Neoproterozoic Mt. Abu granitoids, NW India: regional correlation and implications for Rodinia paleogeography. Precamb. Res., 236, 265-281.

Ayalew, D., Pik, R., Bellahsen, N., France, L. and Yirgu, G., 2019. Differential fractionation of rhyolites during the course of crustal extension, western Afar (Ethiopia rift). Geochem., Geophys., Geosyst., 20, 571-591.

Bansal, A.R. and Dimri, V.P., 2005. Depth determination from a non-stationary magnetic profile for scaling geology. Geophys. Prosp., 53, 399-410.

Barton, P.J., 1986. The relationship between seismic velocity and density in the continental crust: a useful constraint? Geophys. J. Royal Astron. Soc., 87(1), 195-208.

Basu, A.K., 1986. Geology of parts of the Bundelkhand Granite Massif, central India. Geol. Surv. India Spec. Pub., 117, 61-124.

Bhowmik, S.K. and Dasgupta, S., 2012. Tectono-thermal evolution of the banded gneissic complex in central Rajasthan, NW India: present status and correlation. J. Asian Earth Sci., 49, 339-348.

Bhushan, S.K., 1995. Late Proterozoic continental growth: implications from geochemistry of acid magmatic events of west Indian craton, Rajasthan. Geol. Soc. India Mem., 34, 339-355.

Bhushan, S.K., 2000. Malani Rhyolites: a review. Gondwana Res., 3(1), 65-77.

Chatterjee, S.M., Choudhury, M.R., Das, S. and Roy, A., 2017. Significance and dynamics of the Neoproterozoic (810 Ma) Phulad Shear Zone, Rajasthan, NW India. Tectonics, 36(8), 1432-1454.

Chatterjee, S.M., Sarkar, A.K., Roy, A. and Manna, A., 2020. Mid-Neoproterozoic tectonics of northwestern India: evidence of stitching pluton along 810 Ma Phulad Shear Zone. Tectonics, 39(1), e2019TC005902.

Das, L.K., Naskar, D.C., Roy, K.K., Majumdar, R.K., Choudhury, C. and Srivastava, S., 2007. Crustal structure in central India from gravity and magnetotelluric data. Curr. Sci., 92(2), 200-208.

Deb, M. and Sarkar, S.C., 1990. Proterozoic tectonic evolution and metallogenesis in the Aravalli-Delhi Orogenic Complex, northwestern India. Precamb. Res., 46(1-2), 115-137.

Deb, M., Thorpe, R. and Krstic, D., 2002. Hindoli group of rocks in the eastern fringe of the Aravalli-Delhi Orogenic Belt-Archean secondary greenstone belt or Proterozoic supracrustals? Gondwana Res., 5(4), 879-883.

de Wall, H., Pandit, M.K., Don Hauser, I., Schöbel, S., Wang, W. and Sharma, K.K., 2018. Evolution and tectonic setting of the Malani-Nagarparkar Igneous Suite: a Neoproterozoic silicic-

dominated Large Igneous Province in NW India-SE Pakistan. J. Asian Earth Sci., 160, 136-158.

de Wall, H., Regelous, A., Tomaschek, F., Bestmann, M., Hahn, G. and Sharma, K.K., 2022. Tonian evolution of an active continental margin-A model for Neoproterozoic NW India-SE Pakistan-E Oman linkage. Precamb. Res., 381, 1080-1102.

Dey, B., Das, K., Dasgupta, N., Bose, S., Hidaka, H. and Ghatak, H., 2019. Zircon U-Pb (SHRIMP) ages of the Jahazpur granite and Mangalwar gneiss from the Deoli-Jahazpur sector, Rajasthan, NW India: a preliminary reappraisal of stratigraphic correlation and implications to crustal growth. In: Mondal MEA (ed) Geological Evolution of the Precambrian Indian Shield. Society of Earth Scientists Series. Springer, Cham, 514 p.

Dharma Rao, C.V., Santosh, M., Kim, S.W. and Li, S., 2013. Arc magmatism in the Delhi fold belt: SHRIMP U-Pb zircon ages of granitoids and implications for Neoproterozoic convergent margin tectonics in NW India. J. Asian Earth Sci., 78, 83-99.

Dutta, A.K., 1983. Geological evolution and hydrocarbon prospects of Rajasthan Basin. In: Bhandari, L.L., Venkatchala, B.S., Kumar, R., Nanjudaswamy, S., Garg, P. and Srivastava, D.C., (Eds.), Petroliferous Basins of India, Petroleum Asia J., 4, 93-100.

Dwivedi, D., Chamoli, A. and Pandey, A.K., 2019. Crustal structure and lateral variations in Moho beneath the Delhi fold belt, NW India: insight from gravity data modelling and inversion. Phys. Earth Planet. Inter., 297, 106317.

Ernst, R., Liikane, D., Jowitt, S., Buchan, K. and Blanchard, J., 2019. A new plumbing system framework for mantle plume-related continental large igneous provinces and their mafic-ultramafic intrusions. J. Volcanol. Geoth. Res., 384, 75-84.

Fareeduddin and Banerjee, D.M., 2020. Aravalli Craton and its mobile belts: an update. Episodes. J. Int. Geosci., 43(1), 88-108.

Geosoft, 2015. OASIS Montaj Version 8.4: a user-friendly software for processing and interpretation of geophysical data. Geosoft Incorporation, Toronto, Canada.

Ghosh, S., D'Souza, J., Goud, B.R. and Prabhakar, N., 2023. A review of the Precambrian tectonic evolution of the Aravalli Craton, northwestern India: Structural, metamorphic and geochronological perspectives from the basement complexes and supracrustal sequences. Earth-Science Rev., 232 (2022), 104098.

Gregory, L.C., Meert, J.G., Bingen, B.A., Pandit, M.K. and Torsvik, T.H., 2009. Paleomagnetism and geochronology of the Malani Igneous Suite, north-west India: implications for the configuration of Rodinia and the assembly of Gondwana. Precamb. Res., 170(1-2), 13-26.

GSI, 1998. Geological Map of India on a 1:2 million scale. Geol. Surv. India, Kolkata, India.

GSI, 2000. Seismotectonic Atlas of India and its Environs. Geol. Surv. India, Kolkata, India.

GSI-NGRI, 2006. Gravity Map Series of India, Geol. Surv. India and Nat. Geophys. Res. Inst., Hyderabad, India.

Hinze, W.J., von Freese, R.R.B. and Saad, A.H., 2013. Gravity and Magnetic Exploration: Principles, Practices, and Applications. Cambridge University Press, U.K., 512 p.

Jain, A.K., Banerjee, D.M. and Kale, V.S., 2020. Tectonics of the Indian Subcontinent. Springer Nature, Switzerland, 576 p.

Kaila, K.L., Reddy, P.R., Dixit, M.M. and Rao, P.K., 1985. Crustal structure across the Narmada-Son lineament, central India, from deep seismic soundings. J. Geol. Soc. India, 26, 465-480.

Kailasam, L.N., 1976. Geophysical studies of the major sedimentary basins of the Indian craton, their deep crustal structures and evolution. Tectonophysics, 36(1-3), 225-245.

Kaur, P., Zeh, A. and Chaudhri, N., 2021. Archean to Proterozoic (3535-900 Ma) crustal evolution of the central Aravalli banded gneissic complex, NW India: new constraints from zircon U-Pb-Hf isotopes and geochemistry. Precamb. Res., 359, 106179.

Krishna Brahmam, N., 1993. Gravity and seismicity of Jaisalmer region, Rajasthan. Curr. Sci., 64(11 -12), 837-840.

Krishna, V.G. and Rao, V., 2010. Velocity modeling of a complex deep crustal structure across the Mesoproterozoic south Delhi fold belt, NW India, from joint interpretation of coincident seismic wide-angle and near-offset reflection data: an approach using unusual reflections in wide-angle records. J. Geophys. Res.: Solid Earth, 116(B1). doi.org/10.1029/2009JB006660

Kumar, N., Singh, A.P. and Tiwari, V.M., 2020. Gravity anomalies, isostasy and density structure over Indian continent. Episodes, J. Int. Geosci., 43(1), 609-621.

Kumar, P., Tewari, H.C. and Khandekar, G., 2000. An anomalous high-velocity layer at shallow crustal depths in the Narmada zone, India. Geophys. J. Int., 142(1), 95-107.

Mandal, B., Sen, M.K., Rao, V.V. and Mann, J., 2014. Deep seismic image enhancement with the common reflection surface (CRS) stack method: evidence from the Aravalli-Delhi fold belt of north-western India. Geophys. J. Int., 196(2), 902-917.

Mandal, B., Vaidya, V.R., Sen, M.K., Periyasamy, K. and Sarkar, D., 2018. Common reflection surface stack imaging of the Proterozoic Chambal valley, Vindhyan basin and its boundary fault in the north-west India: constraints on crustal evolution and basin formation. Tectonics, 37, 1393-1410.

Meert, J.G., Pandit, M.K. and Kamenoy, G.D., 2013. Further geochronological and paleomagnetic constraints on Malani (and pre-Malani) magmatism in NW India. Tectonophysics, 608, 1254-1267.

Mishra, D.C. and Ravikumar, M., 2014. Proterozoic orogenic belts and rifting of Indian cratons: geophysical constraints. Geosci. Front., 5(1), 25-41.

Mishra, D.C., Singh, B., Tiwari, V.M., Gupta, S.B. and Rao, M.B.S.V., 2000. Two cases of continental collisions and related tectonics during the Proterozoic period in India: insights from gravity modelling constrained by seismic and magnetotelluric studies. Precamb. Res., 99(3-4), 149-169.

Mondal, M.E.A., 2019. Geological Evolution of the Precambrian Indian Shield. Springer International Publishing AG, Switzerland, 749 p.

Naganjaneyulu, K. and Santosh, M., 2012. Tracing the Proterozoic continental collision in NW India: a geophysical approach. Geol. J., 47(2-3), 114-129.

Naqvi, S.M. and Rogers, J.J.W., 1987. Precambrian Geology of India. Oxford University Press, New York, 223 p.

Nayak, P.N., Dutta, K.K., Ravishanker and Sehgal, M.N., 1986. Geological and geophysical studies vis-à-vis result of DSS profiles in central India: an analysis. In: Kaila KL, Tewari HC (eds) Deep Seismic Soundings and Crustal Tectonics, AEG Publication, Hyderabad, India, pp. 83-97.

Pandey, O.P., 2020. Geodynamic Evolution of the Indian Shield: Geophysical Aspects. Springer Nature Switzerland AG Publication, pp. 349.

Pandit, M.K., Shekhawat, L.S., Ferreira, V.P., Sial, A.N. and Bohra, S.K., 1999. Trondhjemite and granodiorite assemblages from west of Barmer: probable basement for Malani magmatism in western India. J. Geol. Soc. India, 53, 89-96.

Pati, J.K. and Singh, A.K., 2020. Bundelkhand Craton. Proceed. Indian Nat. Sci. Acad., 86(1), 55-65.

Porwal, A., Carranza, E.J.M. and Hale, M., 2006. Tectonostratigraphy and base-metal mineralisation controls, Aravalli province (western India): new interpretations from geophysical data analysis. Ore Geol. Rev., 29(3-4), 287-306.

Prakash, O., Singh, A.P., Prasad, K.N. D., Rao, B.N. and Pandey, A.K., 2020. Remnant plume head under Neoproterozoic Malani Igneous Suite, western India. Tectonophysics, 792**,** 228576.

Prasad, K.N.D., Singh, A.P. and Tiwari, V.M., 2018. 3D Upper crustal density structure of the Deccan Syneclise, central India. Geophys. Prospect., 66(8), 1625-1640.

Prasad, K.N.D., Singh, A.P., Rao, P.R., Prakash, O. and Begum, S.K., 2021. Multistage magmatic intrusion in Narmada-Tapti region, India: insights from geopotential modelling. J. Earth Syst. Sci., 130, 1-28.

Qureshy, M.N., 1971. Relation of gravity to elevation and rejuvenation of blocks in India. J. Geophys. Res., 76(2), 545-557.

Qureshy, M.N., 1981. Gravity anomaly, isostasy and crust-mantle relations in the Deccan Trap and contiguous regions, India. In: Subba Rao KV, Sukheswala RN (eds) Deccan Volcanism. Geol. Soc. India Mem., 3, 184-197.

Qureshy, M.N. and Warsi, W.E.K., 1972. Gravity bases established in India by N.G.R.I.-Part-II. Geophys. Res. Bull., 10(3-4), 141-152.

Qureshy, M.N. and Warsi, W.E.K., 1975. Role of regional gravity in a concept-oriented exploration programme: some inferences from a study in a shield area of central India. J. Geol. Soc. India, 16, 44-54.

Ramakrishna, T.S. and Rao, K.V.S.B., 1981. A geophysical study of the environment of base-metal belts and related deep geological features to guide mineral exploration in Rajasthan. Part II Surveys, Geol. Surv. India Rep. (unpublished).

Rao, V. and Krishna, V., 2013. Evidence for the Neoproterozoic Phulad suture zone and genesis of Malani magmatism in the NW India from deep seismic images: implications for assembly and breakup of the Rodinia. Tectonophysics, 589, 172-185.

Rao, V., Rajendra Prasad, B., Reddy, P. and Tewari, H., 2000. Evolution of Proterozoic Aravalli-Delhi fold belt in the northwestern Indian shield from seismic studies. Tectonophysics, 327(1-2), 109-130.

Ravi Kumar, M., Saul, J., Sarkar, D., Kind, R. and Shukla, A.K., 2001. Crustal structure of the Indian shield: new constraints from teleseismic receiver functions. Geophys. Res. Lett., 28(7), 1339-1342.

Raza, M., Khan, A. and Khan, M.S., 2009. Origin of Late Palaeoproterozoic Great Vindhyan basin of north Indian shield: geochemical evidence from mafic volcanic rocks. J. Asian Earth Sci., 34, 716-730.

Reddi, A.G.B. and Ramakrishna, T.S., 1988a. Bouguer Gravity Atlas of Western India (Rajasthan-Gujrat) shield. Geological Survey of India Publication, Kolkata, India.

Reddi, A.G.B. and Ramakrishna, T.S., 1988b. Subsurface structure of the shield area of Rajasthan-Gujarat as inferred from gravity. In: Roy AB (ed) Precambrian of the Aravalli Mountain. Geol. Soc. India Mem., 7, 279-284.

Roy, A.B., 1990. Evolution of the Precambrian crust of the Aravalli mountain range. In: Naqvi SM (ed) Precambrian Continental Crust and its Economic Resources. Elsevier Publication, Amsterdam, pp. 327-348.

Roy, A.B., 2003. Geological and geophysical manifestations of the Reunion plume-Indian lithosphere interactions-evidence from northwest India. Gondwana Res., 6(3), 487-500.

Sharma, J., Kumar, M.R., Roy, K.S. and S. Roy, P.N., 2018. Seismic imprints of plume-lithosphere interaction beneath the northwestern Deccan volcanic province. J. Geophys. Res.: Solid Earth, 123(12), 10,831-10,853.

Sharma, K.K., Rahman, A., 2000. The Early Archaean-Paleoproterozoic crustal growth of the Bundelkhand craton, northern Indian shield. In: Deb M (ed) Crustal Evolution and Metallogeny in the Northwestern Indian Shield, Narosa Publishing House, New Delhi, pp. 51-72.

Sharma, R.S., 2009. Cratons and Fold Belts of India. Springer Publications, Switzerland, 304 p.

Sharma, R.S. and Mondal, M.E.A., 2019. Evolution of the Indian shield: a new approach. In: Mondal MEA (ed) Geological Evolution of the Precambrian Indian Shield, Springer Publication, pp. 17-38.

Singh, A.P. and Meissner, R., 1995. Crustal configuration of the Narmada-Tapti region (India) from gravity studies. J. Geodyn., 20(2), 111-127.

Sinha-Roy, S., 1988. Proterozoic Wilson Cycles in Rajasthan, NW India. Geol. Soc. India Mem., 7, 95-108.

Sinha-Roy, S., 2000. Precambrian terrain evolution in Rajasthan. Geol. Surv. India Spec. Pub. Ser., 55(1), 275-286.

Sinha-Roy, S. and Malhotra, G., 1989. Structural relations of Proterozoic cover and its basement: an example from the Jahazpur belt, Rajasthan. J. Geol. Soc. India, 34(3), 233-244.

Sinha-Roy, S., Malhotra, G. and Guha, D.S., 1995. A transect across Rajasthan Precambrian terrain in relation to geology, tectonics and crustal evolution of south-central Rajasthan. In Sinha-Roy S., Gupta K.R. (eds) Continental Crust of Northwestern and Central India. Geol. Soc. India Mem., 31, 63-90.

Soni, M.K., Chakraborty, S. and Jain, V.K., 1987. Vindhyan Supergroup. Geol. Soc. India Mem., 6, 87-138.

Sugden, T.J., Deb, M. and Windley, B.F., 1990. The tectonic setting of mineralisation in the Proterozoic Aravalli-Delhi orogenic belt, NW India. In: Naqvi S.M. (ed) Precambrian Continental Crust and its Economic Resources. Elsevier, Amsterdam, pp. 367-390.

Tewari, H.C. and Kumar, P., 2003. Deep seismic sounding studies in India and its tectonic implications. In: Mita Rajaram (ed.) Geophysics: Window to Indian Geology. J. Virtual Expl., 12, 30-54.

Tewari, H.C., Dixit, M.M., Rao, N.M., Venkateshwarlu, N. and Rao, V.V., 1997. Crustal thickening under the Paleo-Meso-Proterozoic Delhi fold belt in NW India: evidence from deep reflection profiling. Geophys. J. Int., 129(3), 657-668.

Thybo, H. and Artemieva, I.M., 2013. Moho and magmatic underplating in continental lithosphere. Tectonophysics, 609, 605-619.

Torsvik, T.H., Carter, L.M., Ashwal, L.D., Bhushan, S.K., Pandit. M.K. and Jamtveit, B., 2001. Rodinia redefined or obscured: palaeomagnetism of the Malani Igneous Suite (NW India). Precamb. Res., 108(3-4), 319-333.

Wang, W., Cawood, P.A., Pandit, M.K., Zhou, M.F. and Zhao, J.H., 2018. Evolving passive and active-margin tectonics of the Paleoproterozoic Aravalli basin, NW India. Geol. Soc. Am. Bull., 131, 426-443.

Received on: 10-09-2025; Revised on: 07-11-2025; Accepted on: 10-11-2025

J. Ind. Geophys. Union, 30(1) (2026), 35-44
https://doi.org/10.71122/JIGU.30(1)2026.004

Seismic site characterization in the region near Korba coalfield, Chhattisgarh (India)

Tushar Singhania[1,2], Niptika Jana[1*] and Sanjit Kumar Pal[1]
[1]Department of Applied Geophysics, Indian Institute of Technology (Indian School of Mines)
Dhanbad, Dhanbad-826004, Jharkhand, India
[2]Department of Civil and Infrastructure Engineering, Indian Institute of Technology Jodhpur, Jodhpur District-342030, Rajasthan, India
**Corresponding author: niptika.jana.1201@gmail.com*

ABSTRACT

This study employs seismic techniques for the site characterization of the Korba region in Chhattisgarh, India. Seismic activity has been reported in this region lately, classifying this region in seismic zone III, according to the Building Materials and Technology Promotion Council (BMTPC) assessment (2006). We gather data from 30 different locations in the Korba region, using the Tromino instrument. We estimate the fundamental frequency, construct shear wave velocity for subsurface classification of the Korba region, and develop Horizontal-to-Vertical Spectral Ratio (HVSR) curves for ambient noise data in accordance with the National Earthquake Hazards Reduction Programme (NEHRP) criteria. We calculated the liquefaction vulnerability index (Kg), amplification value, and peak resonant frequencies from the HVSR curve. Amplification factors range from 1.18 to 10.02, while the peak resonant frequencies span from 1.146 to 15.062 Hz. Vs30 for the region varies between 140.06 and 646.90 m/s. These findings indicate presence of soft soil in the western portion of the region, which is situated along the Hasdeo River's bank. In majority of the places, we discovered that the Kg value was less than 10, indicating low liquefaction vulnerability in the examined area.

Keywords: Horizontal-to-vertical spectrum (HVSR), Shear wave velocity, Peak resonant frequency, Site characterization, Liquefaction vulnerability index (Kg), Digital Elevation Model (DEM).

INTRODUCTION

Classification of the nature of subsurface, plays a major role in generating seismic damage risks (Gupta et al. 2021), as soil properties influence the likelihood and severity of an earthquake in a particular region (Akkaya and Ozvan, 2019). Earthquakes produce strong and dynamic forces that travel through the earth as seismic waves. These waves have the potential to induce seismic activity, resulting in vibrations that can impact structures and their foundations. Comprehending the soil's response to these dynamic stresses, is crucial as it differs significantly from its behaviour under static loads, such as the weight of a structure (Farrugia et al., 2016). Understanding the behaviour of soil under dynamic loads, helps in selecting suitable structures that can withstand seismic forces and implementation of appropriate mitigation measures. The soft soil layer's resonance frequency and shear wave velocities (V_S), are crucial for predicting ground motion and effectively preventing or mitigating seismic catastrophes (Farrugia et al., 2016). Comprehending the geographical variances is crucial for evaluating earthquake hazards, preparing for them, and designing robust infrastructure (Ansal, 1999).

Many studies have been conducted on seismic site characterization in various regions (Picozzi et al., 2009; Foti et al., 2011; Gupta et al., 2019; Cultrera et al., 2021; Gupta et al., 2021; Vijayan et al., 2022). However, no similar study has been conducted in the surrounding areas of the Korba region. The current increase in seismic activity in several districts of Chhattisgarh, including Korba, highlights the need to understand the subsurface dynamics for upcoming developmental projects (Parashar, 2023).

The studied region lies under seismic zone 'III' of India, which is a moderate-intensity zone that is assigned under zone factor 0.16. (BMTPC 2nd edition). The Hasdeo river flows in the southern part of the Korba, which divides it into two parts (Singh et al., 2016). The coal mines of Korba include Manikpur, Gevra, Dipka, Kusumunda, Laxman, Pavan, Rajgamar, Balig, Banki, and Surakachhar, out of which Manikpur, Gevra, Dipka and Kusumunda are operated as open cast mines (Singh et al., 2016).

The current population of the Korba region is approximately 5,00,000, which has increased by 1.86% since 2022 (Census of India, 2011). With the increase in population, more construction work is happening in this region. The Korba region lies in seismic zone III, where an earthquake up to magnitude 6 can be expected (Sairam et al., 2011). This would have the potential to damage single-story or multi-story buildings. Therefore, any development in this region should be done by taking into consideration the seismic parameters to mitigate potential damages and ensure resilient development of projects.

Seismic site characterization is often used to identify the sub-surface material properties of the earth. Parameters that are used to define these material properties are, the shear modulus and shear wave velocity, among others (Pandey et al., 2016). Vs 30 value varies with depth as the subsurface profile changes, so thereby with the application of site characterization, we can identify the material properties of any zones as well (Gupta et al., 2019). Many site characterisation techniques are used to identify the characteristics of a site to facilitate ground response analysis, such as Horizontal-to-vertical spectral ratio (HVSR) (Nakamura, 1989), Multichannel analysis of surface

wave (MASW) (Park et al., 1999), Surface analysis of surface waves (SASW), and many more.

In the current study, the Horizontal to Vertical spectral ratio (HVSR) site characterization method was used to classify the subsurface characteristics in the Korba region. Because of its affordability and ease of integration, HVSR is one of the popular non-invasive geophysical site characterization technique, which is used for the measurement of site amplification through the resonant frequency, generated by a three-component seismograph (Lachetl and Bard, 1994). After Nakamura (1989), many researchers used this technique to analyse the seismic site characterization (Nakamura, 1989, 1996, 2000; Field and Jacob, 1993; Bard, 1998; Gallipoli and Mucciarelli, 2009; Sisman et al., 2018; Tiwari et al., 2024). The main objective of this study is to generate the HVSR curves for ambient noise data and estimate the predominant frequency, i.e., fundamental frequency. Then, further inverting the data, we aim to achieve the shear wave velocity profiles to classify the sub-surface of the Korba region as per National Earthquake Hazards Reduction Program NEHRP guidelines (Safety, 2003). The NEHRP, classifies the soil into five types based on their average shear wave velocity at 30 m (Vs30), i.e.,

(i) Soil Type A: Vs30 > 1500m/s, described as hard rock.

(ii) Soil Type B: 760<Vs30< 1500m/s, described as rock.

(iii) Soil Type C: 360<Vs30< 760m/s, described as soft rock/very stiff soil, mostly gravels.

(iv) Soil Type D: 180<Vs30< 360m/s, described as sand, silt, very stiff clay or some gravels.

(v) Soil Type E: Vs30< 180m/s, described as soft clay.

For this purpose, we attempted to collect ambient noise data by using the Tromino instrument in the Korba region. The Tromino is a versatile all-in-one seismometer used for subsoil characterization (HVSR, MASW, and more) and vibration monitoring. It is equipped with three velocimetric and accelerometric channels, one analog channel, and one GPS receiver. Its working range is 0.1Hz to 1024 Hz, making it a valuable tool for a wide range of seismic studies. (https://www.tromino.it/). The HVSR curves are used to measure the velocity contrast between the upper and the lower sedimentary layer of the earth (Parolai et al., 2002)

GEOLOGY AND TECTONICS

The study area covers the region between 22°15′ N to 22°30′ N and 82°15′ E to 82°55′ E with an area of about 530 km^2 (Raja Rao, 1983). Singh et al. (2016) reported some of the operational mines in the Korba region, which include Gevra, Dipka, Kusumunda, Manikpur and Rajgamar. One of the study (Govil and Guha 2023) reported the lithology of the Rajgamar coal mine, where they described the occurrence of an alluvial soil layer within the top 5.2 m of the ground. beneath that there are different layers of sandstone, coal, shale sandstone, seam coal and coal. Singh et al. (2016) further showed that the Gondwana rocks occur all around the Korba coalfield except on the east side where Archean rocks are present, besides Barakars, Talchirs and Kamthi formations. The southern part of the Korba coalfield is faulted, due to which the upper part of the Barakar formation is directly exposed over the underlying basement.

In another significant study, Singh et al. (2018), which focused on a region primarily distinguished by the upper strata of the Early Permian Barakar Formation, belonging to the Lower Gondwana Group. The geological formations in this region have an east-west orientation and often have a southerly inclination of around 5°-8°. The region is characterised by many transverse faults that exhibit varied orientations, including northeast-southwest, northwest-southeast, and east-west, with varying levels of displacement. An east-west fault is also located which tilts towards the south and connects the Upper and Lower Barakar Formations. Significantly, this geological fault separates the Lower Barakar Formation from the Upper Barakar Formation and probably intersects the Hasdeo River with a very small amount of displacement. The E-W trending fault is the primary structural feature in the area and serves as a major source of seismic activity. It influences the subsurface hydrology and can trigger minor seismic events.

METHODOLOGY

Horizontal to vertical spectral ratio (HVSR)

Nakamura (1989), though credited as the developer of this technique, it was originally suggested by Nogoshi and Igarashi (1970). The fundamental frequency of the soil and site amplification from microtremor data are estimated using the HVSR method. This method helps construction engineers to implement earthquake-resistant design features. It increases resilience and safety. It also improves earthquake preparedness and reduces potential damage during future seismic events. Weak and strong ground motions can be used to construct HVSR curves for soil characterisation (Gallipoli and Mucciarelli, 2009; Özalaybey et al., 2011; Askan et al., 2015, 2017; Sisman et al., 2018; Gupta et al., 2019). HVSR determines the amount of signal strength variation across various frequencies in both horizontal and vertical directions. It's a mean of comprehending a signal's properties in terms of its directed energy distribution. It is defined as,

$$HVSR = \frac{\sqrt{H_{NS}^2 + H_{EW}^2}}{V} \quad (1)$$

Where the vertical, east-west, and north-south components of the waveform are denoted by V, H_{EW}, and H_{NS}, respectively.

The distinctive shape of the HVSR amplitude offers a dependable estimate of the site amplification function. This function contributes significantly to the resonance effect, significantly contributing to heightened vibrations within a structure (Nakamura, 1989; Lachetl and Bard, 1994; Herak, 2008; Clavero et al., 2014). Our method carefully follows the steps and guidelines provided by SESAME (2004) for the collection and processing of ambient noise data for HVSR calculation.

Data acquisition and processing

This study used a Tromino instrument to collect microtremor data from 30 observation points in the studied region as shown in **Figure 1**. The Tromino instrument features three-component orthogonal velocity meters, susceptible to electrodynamic signals. As directed by the instructions of the manufacturer's, the Tromino is positioned and levelled on flat ground, aligned north-south to capture noise data (Gupta et al., 2019, 2021). According to Okada and Suto (2003), frequencies more than 1 Hz are produced by anthropogenic sources, while frequencies lower than ~1 Hz are often associated with natural events. The microtremor data was gathered for 30 minutes at a sample frequency of 1024 Hz at each observation site. HVSR data processing was done using Geopsy software (www.geopsy.org).

Additionally, the data was processed by dividing them into stationary windows of 20 to 40 seconds, with the following parameters applied: 2s for short-term averaging (STA), 30s for long-term averaging (LTA), and 0.2 and 0.3s for low and high STA/LTA thresholds, respectively (Hellel et al., 2012). The individual spectra were processed using the technique of Konno and Ohmachi (1998) with a bandwidth coefficient of b=40, before being averaged. Following the widely accepted standard criteria described in SESAME (2004), a demonstration of Horizontal-to-Vertical Spectral Ratio (HVSR) curve was calculated for every site and those in the array. The liquefaction vulnerability index (K_g) values at each location were determined through an empirical formula correlating the dominant frequency (f_o) and amplification factor (A_o).

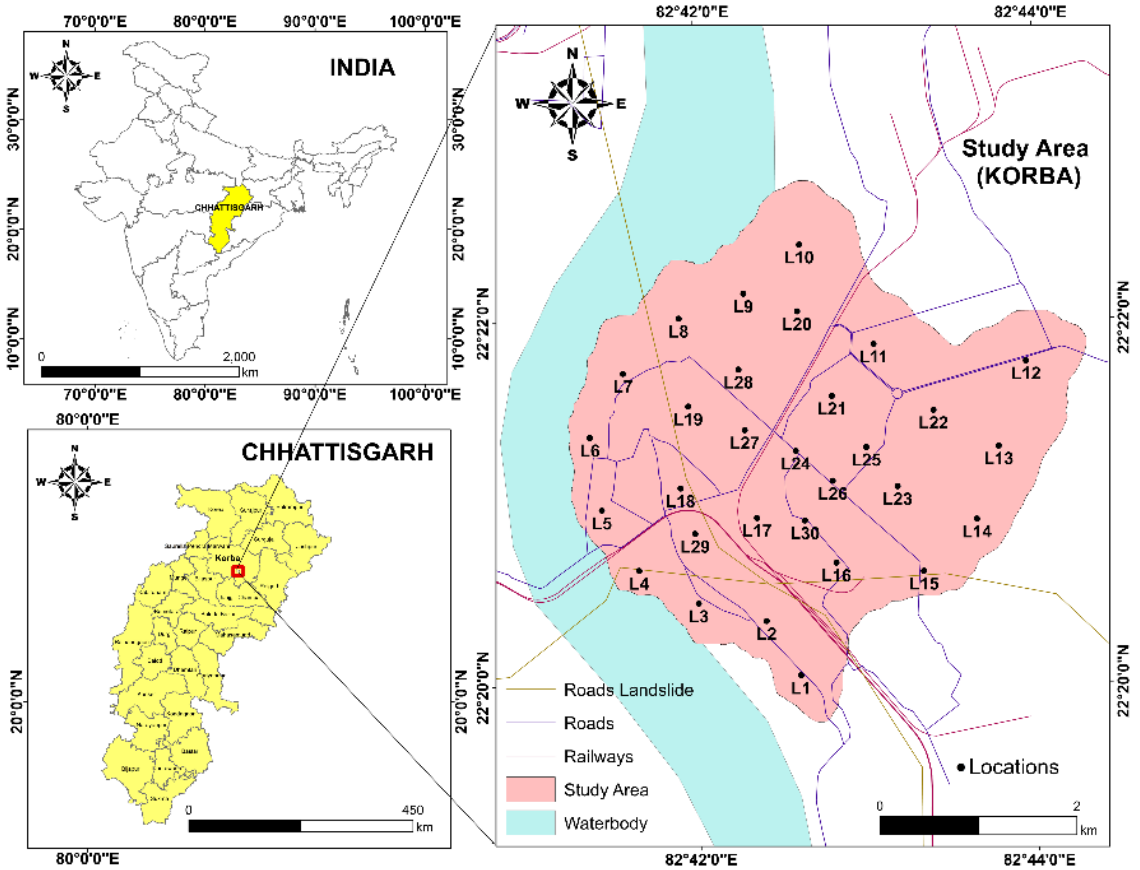

Figure 1. Map showing the locations of microtremor area measurement

$$K_g = \frac{A_O^2}{f_O} \quad (2)$$

Shear wave velocity

The Dinver software (www.geopsy.org) was used for the inversion of the HVSR curve, resulting in the velocity profile for the input data. The inversion process involves systematically searching for parameters that yield the optimal model by minimizing the misfit value (Hobiger, 2011). Parameter constraints that were applied in Dinver during the inversion are, compression-wave velocity, Poisson's ratio, shear-wave velocity, and density. All the parameters were defined as per the pre-defined specified ranges. P wave velocity (Vp), S wave velocity (Vs), and density characteristics were employed as limitations in previous studies to create a model that closely approximates the actual subsurface structure (Katriani et al., 2019; Susilanto et al., 2019). The ellipticity curve is a useful modelling tool that is utilised in the inversion of the HVSR curve. The idea behind this method is to combine the signal window derived from microtremor data in order to distinguish Rayleigh waves from other types of waves. The energy of the combined horizontal and vertical signals inside the signal window is then calculated beyond that. The ellipticity of Rayleigh waves may be determined using this energy as a measure. A relationship between the subsurface structure and the Rayleigh wave ellipticity is established and is explained as a function of frequency. In particular, it sheds light on the sediment thickness and shear wave velocity profiles within the geological layers. Essentially, by carefully examining the Rayleigh wave properties, the ellipticity curve becomes an invaluable instrument for understanding the complex features of underground structures (Hobiger et al., 2009).

RESULTS AND DISCUSSION

For 30 investigated sites in the Korba region, the Horizontal-to-Vertical Spectral Ratio (HVSR) curves were obtained. Examples of the HVSR curves of some investigated locations are shown in Figure 2. This showed the dominant frequency and amplitude characteristics, which are shown in Figures 3 and 4, respectively. The presented spectral ratios showed a frequency range of 0.2-20 Hz, which is essential for assessing common civil engineering structures. Impedance differences between the underlying hard rock and the superficial soft layers are indicated by diagnostic peaks in the HVSR curves. Large peak values frequently indicate sharp contrasts, which may imply that ground motion is amplified (Parolai et al., 2002; Sukumaran et al., 2011; Singh, 2015; Singh et al., 2017a).

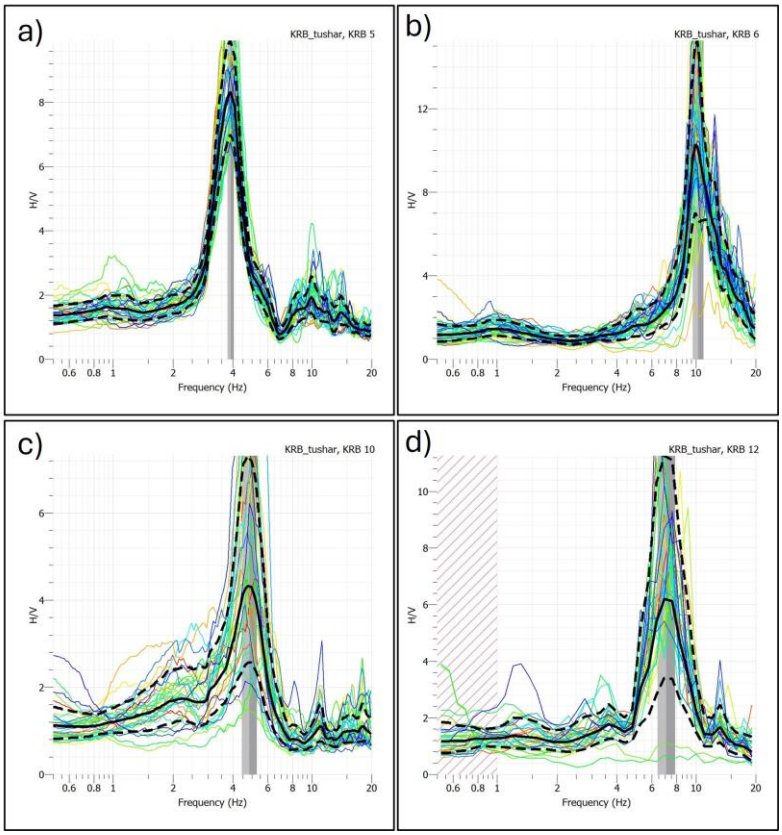

Figure 2. A sample of HVSR curves obtained at **(a)** location 5 (Sarwamangala Para), **(b)** location 6 (Ratakhar), **(c)** location 10 (Dhondi Para) and **(d)** location 12 (Manglam Vihar).

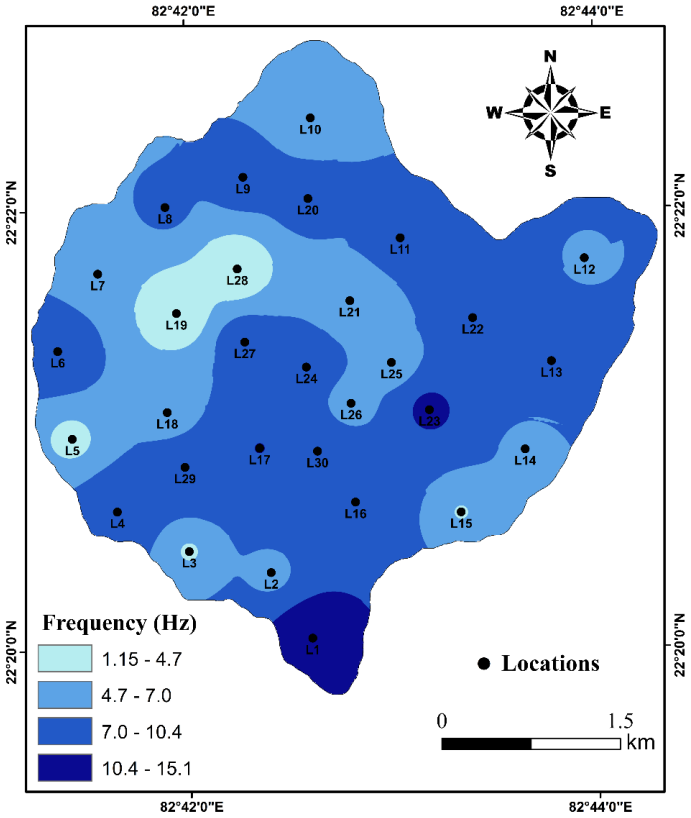

Figure 3. Spatial distribution of peak resonant frequency (Hz) in the study area. Black dots indicate the locations of measurement points.

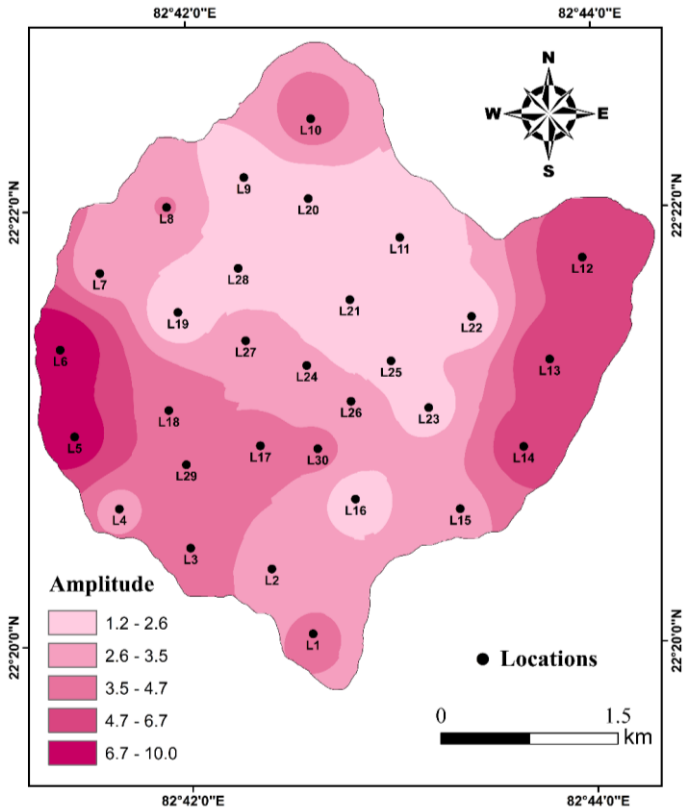

Figure 4. Spatial distribution of amplification factor in the study area. Black dots indicate the locations of measurement points.

Peak resonant frequencies in the Korba region vary mostly between 1.146 and 15.062 Hz, and the corresponding amplification factors fall between 1.18 and 10.02. Figure 5 represents some examples of shear wave velocity profiles at a depth of 30 m (Vs30), as derived by the inversion of HVSR curves. The value of Vs30 ranges from 140.06 to 646.90 m/sec.

Our results indicate that the majority of the Korba region under study fits into the D soil type category, which can be defined as sand, silt, extremely stiff clay, or certain gravels, in accordance with the guidelines of the NEHRP, as can also be noted from Figure 6.

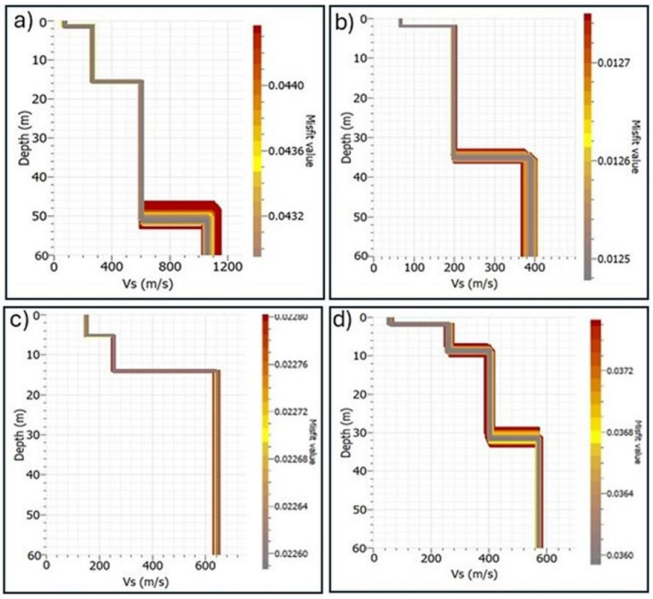

Figure 5. A sample of shear wave velocity profiles obtained at **(a)** location 5 (Sarwamangala Para), **(b)** location 6 (Ratakhar), **(c)** location 10 (Dhondi Para) and **(d)** location 12 (Manglam Vihar).

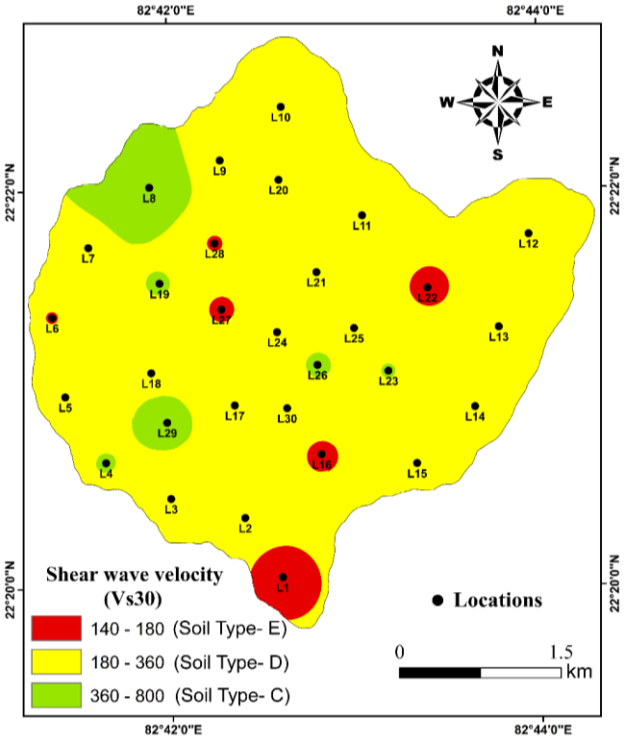

Figure 6. Spatial distribution of shear wave velocity (Vs30) in the study area. Black dots indicate the locations of measurement points

In the western part of the region located to the bank side of the Hasdeo River, the value of amplification factor and peak resonant frequency was observed to be relatively high and low, respectively, which indicates that the soil in that part would be less denser or near to soft (Kramer, 1996). In the North- Eastern part of the study area, the value of the amplitude and peak resonant frequency was observed to be relatively low and high, respectively, which indicates that the soil in that part would be more denser or soft rock (Kramer, 1996). Figure 7 illustrates the Digital Elevation Model (DEM, i.e., Cartosat DEM of 30 m resolution, revealing a distinct topographical pattern along the Hasdeo riverbank. To the west of the region, the terrain exhibits lower elevations, gradually ascending towards the east. Furthermore, the amplitude and frequency values indicate a correlation with soil density. Softer soil can be observed in the lower elevation areas, while denser soil is prevalent in the higher elevation regions.

Further, the soil's vulnerability to liquefication was measured using the liquefaction vulnerability index (K_g value) (Nakamura, 1996). For the betterment of land use planning and mitigating the risk of earthquakes, K_g values offer crucial information on the site's condition (Singh et al., 2017b). The K_g value ranges from 0.03 to 17.65, as seen in Figure 8. High K_g values were found at two locations along the Hasdeo River, indicating that liquefaction occurs at areas with Kg > 10 during large earthquakes (Nakamura, 1996; Huang and Tseng, 2002; Saita et al., 2004; Beroya et al., 2009; Singh et al., 2017b). The K_g value in this study appears to be lower, suggesting that the investigated Korba regions have a lower risk of damage from liquefaction (Singh et al., 2017a).

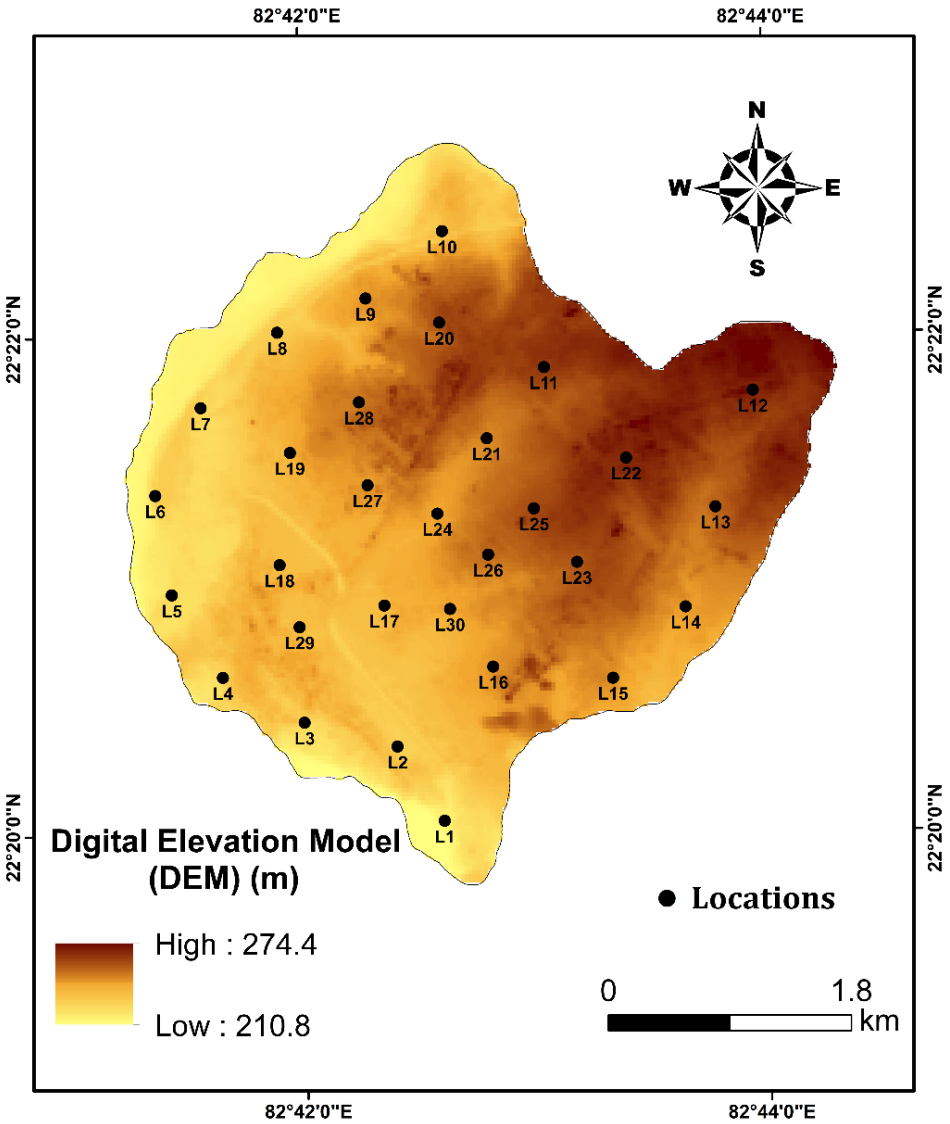

Figure 7. Digital Elevation Model (DEM) for the study area. Black dots indicate the locations of measurement points

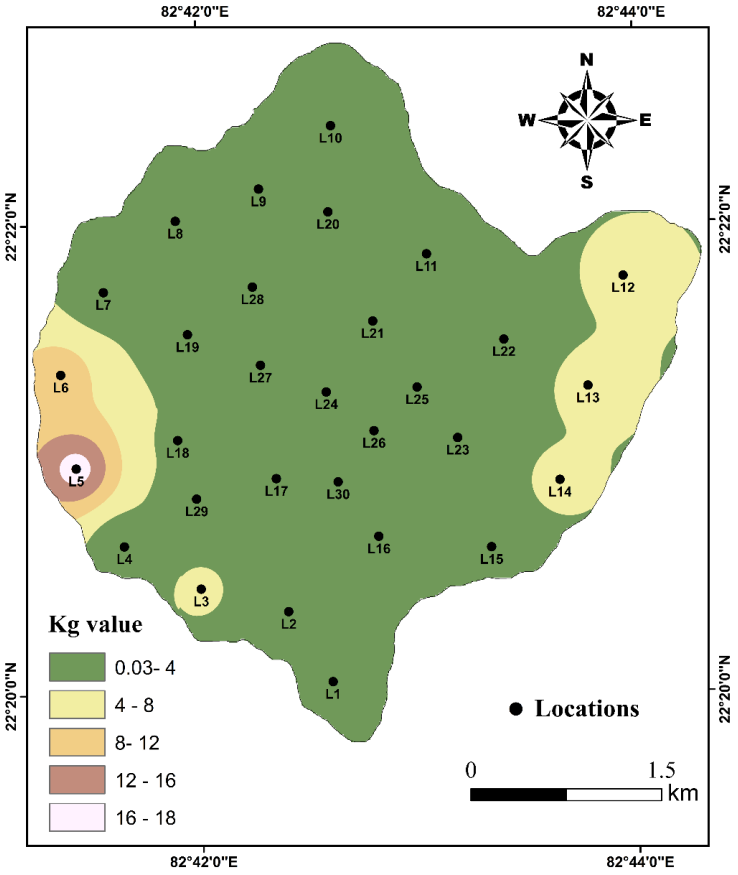

Figure 8. Spatial distribution of Liquefaction Vulnerability Index (Kg) for the study area. Black dots indicate the locations of measurement points

CONCLUSIONS

In the present study, we examined the ambient noise data for 30 sites in the Korba area. Our primary objectives was to provide liquefaction vulnerability index (Kg), shear wave velocity (Vs30) profile, and horizontal-to-vertical spectral ratio (HVSR) curves. Our findings reports the presence of soft soil in the western part of the studied region, which means that these areas are more prone to liquefaction. Our findings in this study will help the engineers to consider all the important factors required before conducting any construction projects in that region. We also find that in the major part of the studied region, the value of the liquefaction vulnerability index is very low, which indicates that these areas have a low risk of ground failure and damage to infrastructure due to low liquefaction during earthquakes, which has important implications for planning of construction projects and disaster preparedness efforts.

Acknowledgement

Tushar Singhania expresses gratitude to Akash Rajput for the help extended during the data collection. Further gratitude is also expressed to Amit Bera for his support in the geoprocessing stages, facilitating an understanding of the instrument and software. No funding agency has given a particular grant for this project. The institutional and national research committees' ethical criteria were followed in every procedure carried out for this investigation.

Author Credit Statement

Tushar Singhania is credited with the data collection, data processing, interpretation and drafting of the manuscript. Niptika Jana is credited with study formation, interpretation, drafting and review of the manuscript. Sanjit Kumar Pal is credited with instrumentation support and review.

Data availability

Data can be made available on a reasonable request.

Compliance with Ethical Standards

The authors declare no conflict of interest and adhere to copyright norms.

REFERENCES

Akkaya, I. and Ozvan, A., 2019. Site characterization in the Van settlement (Eastern Turkey) using surface waves and HVSR microtremor methods. J. Appl. Geophys., 160, 157–170.

Ansal, A.M., 1999. Strong ground motions and site amplification. Earthquake Geotechnical Engineering, 2, 879–894.

Askan, A., Ansal, A., Kurtuluş, A., Kutanis, M., Sucuoglu, H. and Bakir, S., 2015. Assessment of seismic hazard in the Erzincan (Turkey) region: construction of local velocity models and evaluation of potential ground motions. Turk. J. Earth Sci., 24(6), 529–565.

Askan, A., Ansal, A., Kurtuluş, A. and Erdik, M., 2017. An interdisciplinary approach for regional seismic damage estimation. Proc. 16th World Conference on Earthquake Engineering, Santiago, Chile, Jan. 9–13.

Bard, P., 1998. Microtremor measurements: a tool for site effect estimation. In Proceedings, The Effects of Surface Geology on Seismic Motion, 3, 1251–1279.

Beroya, M.A.A., Bautista, M.L.P., Narra, J.C. and Orense, R.P., 2009. Use of microtremor in liquefaction hazard mapping. Eng. Geol., 107(3–4), 140–153.

Building Materials & Technology Promotion Council, Government of India, 2006. Vulnerability Atlas of India, 2nd ed.

Census of India, 2011: Provisional Population Totals. Government of India, 409–413.

Clavero, D., Molina, S., Alarcon, A. and Ruiz, A., 2014. Shear wave velocity estimation in the metropolitan area of Málaga (S Spain). J. Appl. Geophys., 109, 175–185.

Cultrera, G., Cornou, C., Di Giulio, G. and Bard, P.Y., 2021. Indicators for site characterization at seismic stations: recommendations from a dedicated survey. Bull. Earthq. Eng., 19(11), 4171–4195.

Farrugia, D., Paolucci, E., D'Amico, S. and Galea, P., 2016. Inversion of surface wave data for subsurface shear wave velocity profiles characterized by a thick buried low-velocity layer. Geophys. J. Int., 206(2), 1221–1231.

Field, E. and Jacob, K., 1993. The theoretical response of sedimentary layers to ambient seismic noise. Geophys. Res. Lett., 20(24), 2925–2928.

Foti, S., Parolai, S., Albarello, D. and Picozzi, M., 2011. Application of surface-wave methods for seismic site characterization. Surv. Geophys., 32, 777–825.

Gallipoli, M.R. and Mucciarelli, M., 2009. Comparison of site classification from Vs30, Vs10, and HVSR in Italy. Bull. Seismol. Soc. Am., 99(1), 340–351.

Govil, H. and Guha, S., 2023. Underground mine deformation monitoring using synthetic aperture radar technique: a case study of Rajgamar coal mine, Korba, Chhattisgarh, India. J. Appl. Geophys., 209, 104899.

Gupta, R.K., Mahajan, A.K. and Shukla, K., 2019. Site characterization through combined analysis of seismic and electrical resistivity data at Dhanbad, Jharkhand, India. Environ. Earth Sci., 78(6), 226.

Gupta, R.K., Mahajan, A.K., Mittal, H. and Bhattacharya, S.N., 2021. Seismic site characterization and site response study of Nirsa (India). Nat. Hazards, 108(2), 2033–2057.

Hellel, M., Roubion, C., Bensalem, R. and Bard, P.Y., 2012. Basement mapping with single-station and array ambient vibration data: delineating faults under Boumerdes City, Algeria. Seismol. Res. Lett., 83(5), 798–805.

Herak, M., 2008. ModelHVSR- A Matlab tool to model horizontal-to-vertical spectral ratio of ambient noise. Comput. Geosci., 34(11), 1514–1526.

Hobiger, M., 2011. Polarization of surface waves: characterization, inversion and application to seismic hazard assessment. PhD Thesis, Université de Grenoble.

Hobiger, M., Bard, P.Y., Fäh, D. and Scherbaum, F., 2009. Single station determination of Rayleigh wave ellipticity by using the random decrement technique (RayDec). Geophys. Res. Lett., 36(14), L14303.

Huang, H.-C. and Tseng, Y.-S., 2002. Characteristics of soil liquefaction using H/V of microtremors in Yuan-Lin area, Taiwan. Terr. Atmos. Ocean. Sci., 13(3), 325–338.

Katriani, L., Daryono, M.R., Prasetya, G. and Susilanto, P., 2019. Identification of subsurface lithology in Sendang Mulyo, Purwoharjo Village, Samigaluh Subdistrict, Kulon Progo Regency. J. Phys. Conf. Ser., 012008.

Konno, K. and Ohmachi, T., 1998. Ground-motion characteristics estimated from spectral ratio between horizontal and vertical components of microtremor. Bull. Seism. Soc. America, 88(1), pp.228-241.

Kramer, S.L., 1996. Geotechnical Earthquake Engineering. Pearson Education India.

Lachetl, C. and Bard, P.Y., 1994. Numerical and theoretical investigations on the possibilities and limitations of Nakamura's technique. J. Phys. Earth, 42(5), 377–397.

Nakamura, Y., 1989. A method for dynamic characteristics estimation of subsurface using microtremor on the ground surface. Railw. Tech. Res. Inst. Q. Rep., 30(1), 25–33.

Nakamura, Y., 1996. Real-time information systems for seismic hazard mitigation: UrEDAS, HERAS and PIC. Q. Rep. RTRI., 37(3), 112–127.

Nakamura, Y., 2000. Clear identification of fundamental idea of Nakamura's technique and its applications. Proc. 12th World Conference on Earthquake Engineering, 2656, 1–8.

Nogoshi, M. and Igarashi, T., 1970. On the propagation characteristics of microtremors. J. Seism. Soc. Japan, 23, pp.264-280.

Okada, H. and Suto, K., 2003. The microtremor survey method. Soc. Expl. Geophysicists.

Ozalaybey, S., Zor, E., Erdik, M., Alptekin, O., Tapirdamaz, M.C. and Yılmaz, Y., 2011.

Investigation of 3-D basin structures in the Izmit Bay area (Turkey) by single-station microtremor and gravimetric methods. Geophys. J. Int., 186(2), 883–894.

Pandey, B., Jakka, R.S., Kumar, A. and Mittal, H., 2016. Site characterization of strong-motion recording stations of Delhi using joint inversion of phase velocity dispersion and H/V curve. Bull. Seismol. Soc. Am., 106(3), 1254–1266.

Parashar, A.K., 2023. A seismic hazard assessment of North Chhattisgarh (India).. Natural Hazards: New Insights. p. 35

Park, C.B., Miller, R.D. and Xia, J., 1999. Multichannel analysis of surface waves. Geophysics, 64(3), 800–808.

Parolai, S., Bormann, P. and Milkereit, C., 2002. New relationships between Vs, thickness of sediments, and resonance frequency calculated by the H/V ratio of seismic noise for the Cologne area (Germany). Bull. Seismol. Soc. Am., 92(6), 2521–2527.

Picozzi, M., Strollo, A., Parolai, S., Durukal, E., Ozel, O., Karabulut, S., Zschau, J. and Erdik, M., 2009. Site characterization by seismic noise in Istanbul, Turkey. Soil Dyn. Earthq. Eng., 29(3), 469–482.

Raja Rao, C.S., 1983. Coalfields of India Vol. III: Coal Resources of Madhya Pradesh and Jammu and Kashmir. Bull. Geol. Surv. India Ser. A, 45, 204.

Safety, I.S., 2003. NEHRP recommended provisions for seismic regulations for new buildings and other structures (FEMA 450).

Sairam, B., Rastogi, B.K., Aggarwal, S., Chauhan, M. and Bhonde, U., 2011. Seismic site characterization using Vs30 and site amplification in Gandhinagar region, Gujarat, India. Curr. Sci., 754–761.

Saita, J., Bautista, M.L.P. and Nakamura, Y., 2004. On relationship between the estimated strong motion characteristics of surface layer and earthquake damage—case study at Intramuros, Metro Manila. Proc. 13th World Conference on Earthquake Engineering, 1–7.

SESAME, 2004. Guidelines for the implementation of the H/V spectral ratio technique on ambient vibrations measurements, processing and interpretation. European Commission–EVG1-CT-2000-00026 SESAME, 1–62.

Singh, A.K., Varma, N.P. and Mondal, G.C., 2016. Hydrogeochemical investigation and quality assessment of mine water resources in the Korba coalfield, India. Arab. J. Geosci., 9, 1–20.

Singh, A.P., 2015. Seismic hazard evaluation in Anjar city area of western India: microtremor array measurement. Soil Dyn. Earthq. Eng., 71, 143–150.

Singh, A.P., Mishra, O.P., Kumar, A., 2017a. Characterizing surface geology, liquefaction potential, and maximum intensity in the Kachchh seismic zone, Western India, through microtremor analysis. Bull. Seismol. Soc. Am., 107(3), 1277–1292.

Singh, A.P., Parmar, A. and Chopra, S., 2017b. Microtremor study for evaluating the site response characteristics in the Surat City of western India. Nat. Hazards, 89(3), 1145–1166.

Singh, R., Venkatesh, A.S., Syed, T.H., Surinaidu, L., Pasupuleti, S., Rai, S.P. and Kumar, M., 2018. Stable isotope systematics and geochemical signatures constraining groundwater hydraulics in the mining environment of the Korba Coalfield, Central India. Environ. Earth Sci., 77, 1–17.

Sisman, F.N., Askan, A. and Asten, M., 2018. Evaluation of site response with alternative methods: a case study for engineering implications. Pure Appl. Geophys., 175(1), 257–273.

Sukumaran, P., Bhattacharya, S.N., Rai, S. and Mahajan, A.K., 2011. Profiling of late Tertiary–early Quaternary surface in the lower reaches of Narmada valley using microtremors. J. Asian Earth Sci., 41(3), 325–334.

Susilanto, P., Katriani, L., Daryono, M.R. and Prasetya, G., 2019. Analisis kecepatan gelombang geser (Vs) sebagai upaya mitigasi bencana gempabumi di Kulonprogo, DIY. J. Lingkung. dan Bencana Geol., 10(2), 45–53.

Tiwari, A., Rana, N. and Singh, G.P., 2024. A PGA amplification study for Varanasi city (India): Implications for seismic hazard assessment. J. Indian Geophys. Union, 28(6), 417-429.

Vijayan, A., Agrawal, M. and Gupta, R.K., 2022. Seismic site characterization using ambient noise and earthquake HVSR in the easternmost part of Shillong Plateau, India. J. Geol. Soc. India, 98(4), 471–478.

Received on: 17-01-25; Revised on: 6-11-2025; Accepted on : 12-11-2025

J. Ind. Geophys. Union, 30(1) (2026), 45-58
https://doi.org/10.71122/JIGU.30(1)2026.005

Seismic hazard mapping in Gorakhpur, India: A multi parametric approach using predominant frequency, amplification and engineering bed rock depth

Shashank Shekhar[1], Anurag Tiwari[1*], G P Singh[1] and J L Gautam[2]
[1] Department of Geophysics, Banaras Hindu University, Varanasi-221005, India
[2] National Centre for Seismology, Ministry of Earth Sciences, New Delhi- 110003, India
* Corresponding author: aaanuragt@gmail.com

ABSTRACT

Gorakhpur city, situated in the Indo-Gangetic Plain of northern India and classified under Seismic Zone IV, is increasingly getting vulnerable to earthquake-induced ground motion due to its proximity to active Himalayan belt, growing urban footprint and soft alluvial subsurface conditions. This study presents a comprehensive seismic hazard assessment based on key site parameters, including average shear wave velocity up to 30 m ($Vs30$)**,** predominant frequency (f_0)**,** fundamental time period (T_0)**,** peak amplification (A_0)**,** engineering bed rock depth (EBR) and the Seismic vulnerability index (Kg)**.** Ambient noise data is used to estimate f_0 and A_0, while shear wave velocity profiles were obtained through study of Multichannel Analysis of Surface Waves (MASW). Spatial interpolation and GIS-based mapping of these parameters, reveal significant heterogeneity in the subsurface response characteristics. Zones with low $Vs30$, low f_0, longer T_0, high EBR, high A_0 and high Kg values, primarily in the southern parts of the city, demonstrating a high potential for ground motion amplification and structural resonance. The Kg index, effectively highlights the most seismically vulnerable zones within the city, while EBR is estimated using predominant frequency and shear wave velocity. The results underline the critical need for microzonation-based land use planning, earthquake-resilient construction, and site-specific design codes. This study provides essential input for seismic risk reduction and sustainable urban development in Gorakhpur, and establishes a framework for similar assessments in other seismically active regions of the Indo-Gangetic basin.

Keywords: Seismic hazard; $Vs30$; Predominant frequency; Seismic vulnerability index; Engineering bed rock; Gorakhpur; Indo-Gangetic Plain

INTRODUCTION

Earthquakes remain one of the most catastrophic natural hazards, capable of causing extensive loss of life, infrastructure damage, and economic disruption (Kanamori, 1977; Bilham, 2009). The destructive potential of an earthquake is not solely governed by its magnitude or epicentral distance, but also by local site conditions**,** which can significantly amplify ground motions (Seed et al., 1976; Borcherdt, 1994). Hence Seismic hazard assessment is a foundational component of earthquake risk mitigation and resilient urban planning, particularly in tectonically sensitive, thick alluvial subsurface and densely populated regions where seismic ground motions is significantly influenced by local site conditions (Wang and Takada, 2005). While the magnitude and distance of an earthquake source are primary contributors to ground motion intensity, local site effects governed by the subsurface geological and geotechnical conditions, play a crucial role in modifying seismic waveforms. These effects can significantly amplify or de-amplify the ground shaking, affecting the safety and performance of infrastructure during seismic events (Borcherdt, 1994; Bard, 1999). Hence, the characterization of site parameters such as average shear wave velocity ($Vs30$), predominant frequency (f_0), fundamental period (T_0), peak ground amplification (A_0), engineering bed rock depth (EBR) and the seismic vulnerability index (Kg), has emerged as an essential part of site-specific seismic hazard evaluation and microzonation (Nakamura, 1989; Lermo and Chávez-García, 1993; Ibs-von Seht and Wohlenberg, 1999; Delgado et al., 2000).

Gorakhpur City, located in the eastern part of Uttar Pradesh in the Indo-Gangetic Plain, lies in Seismic Zone IV as per the BIS (1893) Part 1 classification, indicating a high damage risk zone. With a population exceeding 0.67 million and a rapid urban growth rate (Census of India, 2011), Gorakhpur's vulnerability to earthquakes is further compounded by its dense infrastructure and ongoing expansion. Its proximity to active Himalayan faults and the alluvial nature of its subsurface deposits enhances the seismic vulnerability of the region (Mohanty et al., 2007; Kolathayar and Sitharam, 2012). In light of growing urbanization and infrastructure development, especially post-2015 urban expansions, it becomes imperative to assess the site response characteristics of the city using various geophysical techniques.

Several studies have emphasized the importance of site characterization for seismic hazard mapping. Nakamura (1989, 2000) introduced the Horizontal-to-Vertical Spectral Ratio (HVSR) technique to estimate predominant site frequency, which has since become a standard method in microtremor-based studies and has been used in recent scenarios as well, such as Shankar et al. (2021a) and Singhania et al. (2026) . Lermo and Chávez-García (1993) validated the use of HVSR in urban site response assessment using single-station measurements. Delgado et al. (2000) introduced the Kg index as an empirical indicator of seismic vulnerability, integrating both amplification and frequency components. Anbazhagan et al. (2010) estimated engineering bedrock depth for shear wave velocity 760 m/s and the depth to bedrock can be estimated using the empirical relation $H = V_s/4f_0$, which is based on the fundamental resonance condition of shear waves in a soil layer overlying the bedrock (Nakamura, 1989; Ibs-von Seht and Wohlenberg, 1999).

In the Indian context, Sitharam et al. (2013) conducted a local site assessment for Lucknow city, while Anbazhagan et al.

(2010) carried out a similar study for Bangalore. Nath et al. (2019), Shankar et al. (2021a), Tiwari et al. (2024) and Shekhar et al. (2025), performed local seismic site characterization in Varanasi, highlighting the spatial variability of f_0 and $Vs30$ in the Ganga alluvial belt. Similarly, studies by Bajaj and Anbazhagan (2019) in the Indo-Gangetic basin and Sitharam et al. (2013) in Uttar Pradesh revealed high amplification zones in regions dominated by thick alluvium. Shankar et al. (2021b) and Khan et al. (2025) also investigated local site parameter for Gorakhpur city. However, Gorakhpur remains largely understudied in terms of integrated, site-specific seismic hazard mapping using dynamic geophysical parameters, despite its strategic and seismic significance.

In this study, the primary objective is to conduct a detailed site-specific seismic hazard assessment of this city by utilizing-site response parameters derived from both field-based geophysical measurements and secondary datasets. Specifically, the study aims to assess the seismotectonic framework to understand the regional seismic setting of Gorakhpur and its surroundings; estimate and spatially interpolate the $Vs30$ using multichannel analysis of surface waves (MASW) and existing borehole data; and derive the predominant frequency (f_0) and corresponding T_0 through microtremor (ambient noise) measurements and HVSR analysis. Additionally, we computed peak ground amplification (A_0) and generated amplification maps for seismic zoning, evaluated the Seismic Vulnerability Index to identify areas with higher potential for seismic damage, and performed EBR modelling. Together, these integrated approaches are intended to provide a robust, high-resolution site-specific seismic hazard profile of Gorakhpur city, supporting effective earthquake risk mitigation and informed urban planning in this region.

STUDY AREA

Gorakhpur city is situated in the eastern part of Uttar Pradesh in India, within the Indo-Gangetic Plain (GDA, 2025). The study area covers both the municipal limits and the peri-urban expansion zones as delineated in the Proposed Land Use Map under Gorakhpur Master Plan 2031 (Revised) (Figure 1). The city is geographically positioned between 26°40′N–26°50′N and 83°20′E–83°30′E, with a total area covered by the Gorakhpur Development Authority (GDA) under which the Gorakhpur Master Plan 2031 is being implemented, has expanded to 643 sq. km. This expanded area includes the Gorakhpur Municipal Corporation, three Nagar Panchayats (Pipraich, Pipiganj, Munderwa Bazar), and 319 villages (GDA, 2024)

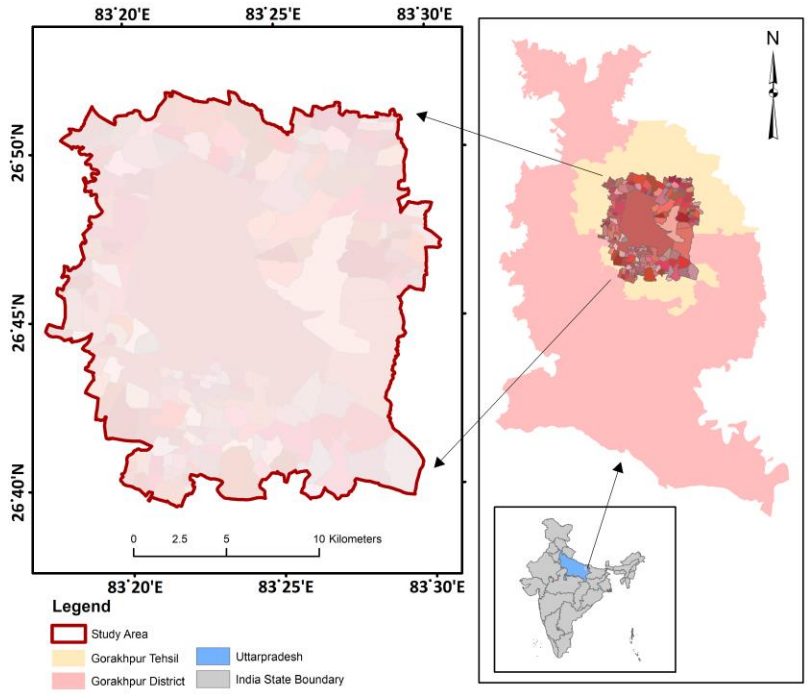

Figure 1. Study area map of Gorakhpur adopted from Gorakhpur Revised Master Plan 2031

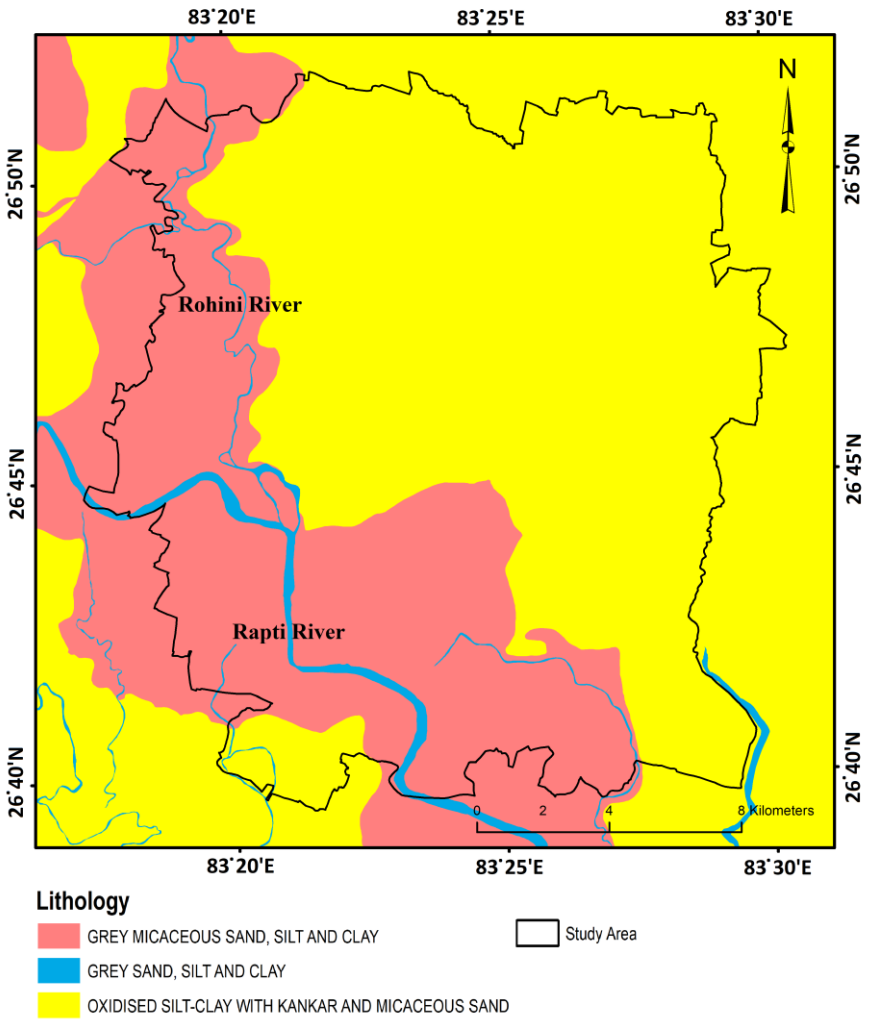

Figure 2. Geological map of Gorakhpur showing the major stratigraphic units (Source: Bhukosh-GSI, 2024)

GEOLOGY AND GEOMORPHOLOGY

The region's geology is characterized by alluvial deposits accumulated over millions of years due to the erosional and depositional activities of Himalayan River systems (Figure 2) (GSI, 2018). The area's geological profile consists primarily of Quaternary sediments, overlying older Tertiary deposits. These sediments are mainly alluvial, comprising sand, silt, and clay in varying proportions.

The geological structure can be divided into three main units: the topmost layer of Recent to Sub-recent alluvium, consisting of fine sand, silt, and clay, typically 10-20 meters thick; the underlying older alluvium, composed of coarser materials including sand, gravel, and occasional clay lenses, extending to depths of 150-200 meters. The Siwalik Group forms the basement rock, consisting of sandstone, shale, and conglomerate of Mio-Pliocene age. (Valdiya, 2010; Singh et al., 2015; Bonsor et al., 2017).

Geomorphologically, Gorakhpur city lies on a flat alluvial plain with a gentle north-south slope, bounded by the Rapti and the Rohini rivers (Figure 3). These rivers have significantly influenced the local landscape through their meandering courses and periodic flooding. The area's geomorphological features include active floodplains along the rivers, older floodplains less prone to flooding, river terraces formed by river incision, and abandoned channels filled with finer sediments (GSI, 2020). These geological and geomorphological characteristics play a crucial role in determining the distribution of shear wave velocities and engineering bedrock depths across the city, which are central to this study's objectives (Sinha and Friend, 1994; Ibs-von Seht and Wohlenberg, 1999).

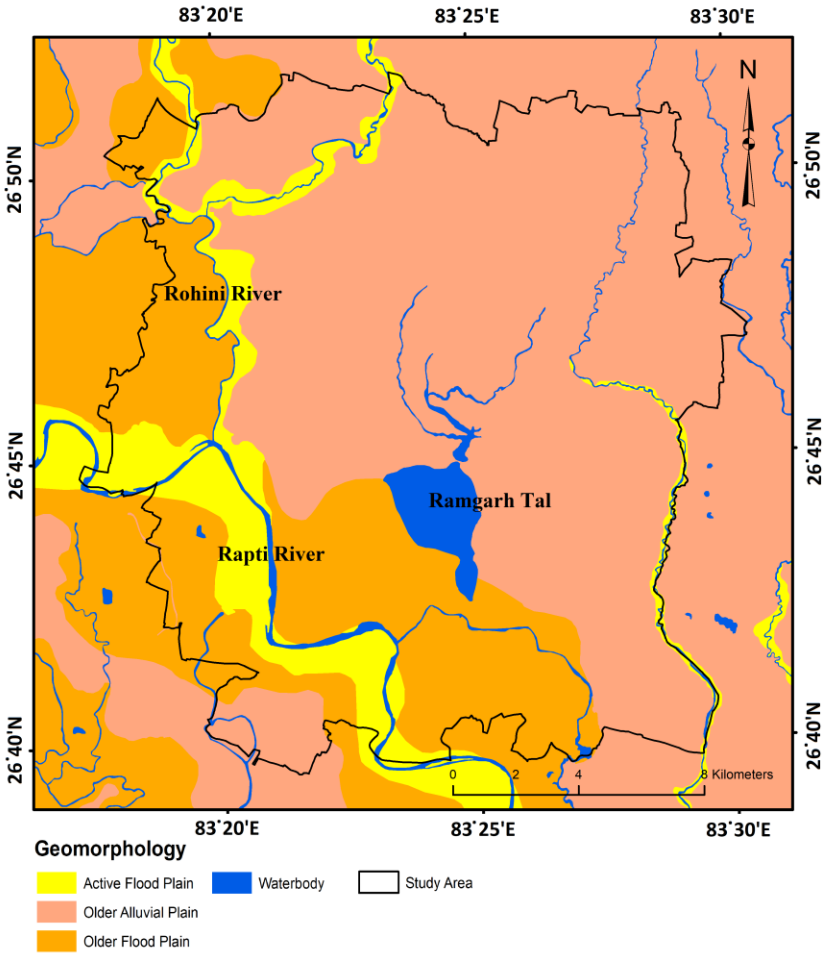

Figure 3. Geomorphological map of Gorakhpur city and its surroundings (Source: Bhukosh-GSI, 2024)

SEISMICITY AND SEISMOTECTONICS

Gorakhpur is located in a seismically active region, influenced by its proximity to the Himalayan collision zone. The city falls under Seismic Zone IV according to the Indian Standard Seismic Zoning Map (BIS, 1893), indicating high damage risk potential. The seismicity of the region is primarily controlled by three major tectonic elements: the Main Boundary Thrust (MBT) located approximately 150 km north, the Himalayan Frontal Thrust (HFT) about 80-100 km north, and the East Patna Fault running NE-SW about 150 km southeast of Gorakhpur (Seeber and Armbruster,1984; Bilham, 2009; Mukhopadhyay, 2018; GSI, 2018, 2020). Historical seismicity records show that Gorakhpur has experienced significant earthquakes, including the 1934 Bihar-Nepal Earthquake (Mw 8.0), the 1988 Bihar Earthquake (Mw 6.6), and the 2015 Gorkha Earthquake (Mw 7.8) in Nepal, which was felt in Gorakhpur and raised concerns about the city's seismic vulnerability (Bilham, 2004, 2009; NDMA, 2010; Nath and Thingbaijam, 2012; USGS, 2024; ISC, 2024). The seismotectonic setting is governed by the presence of several lineaments and buried faults in the Indo-Gangetic Plain (Figure 4).

These features, although not always expressed at the surface, can influence local seismic wave propagation and site response characteristics. The thick alluvial cover in the region can significantly amplify seismic waves, making it essential to accurately characterize the subsurface through Vs and EBR modelling. This seismotectonic context underscores the importance of detailed site characterization studies in the Gorakhpur city. The Vs and EBR models developed in this study will provide crucial inputs for site-specific seismic hazard assessments and help in developing appropriate earthquake-resilient design strategies for the city's infrastructure, addressing the critical need for improved seismic risk mitigation in this rapidly growing urban center. (BIS, 1893; Nath et al., 2007).

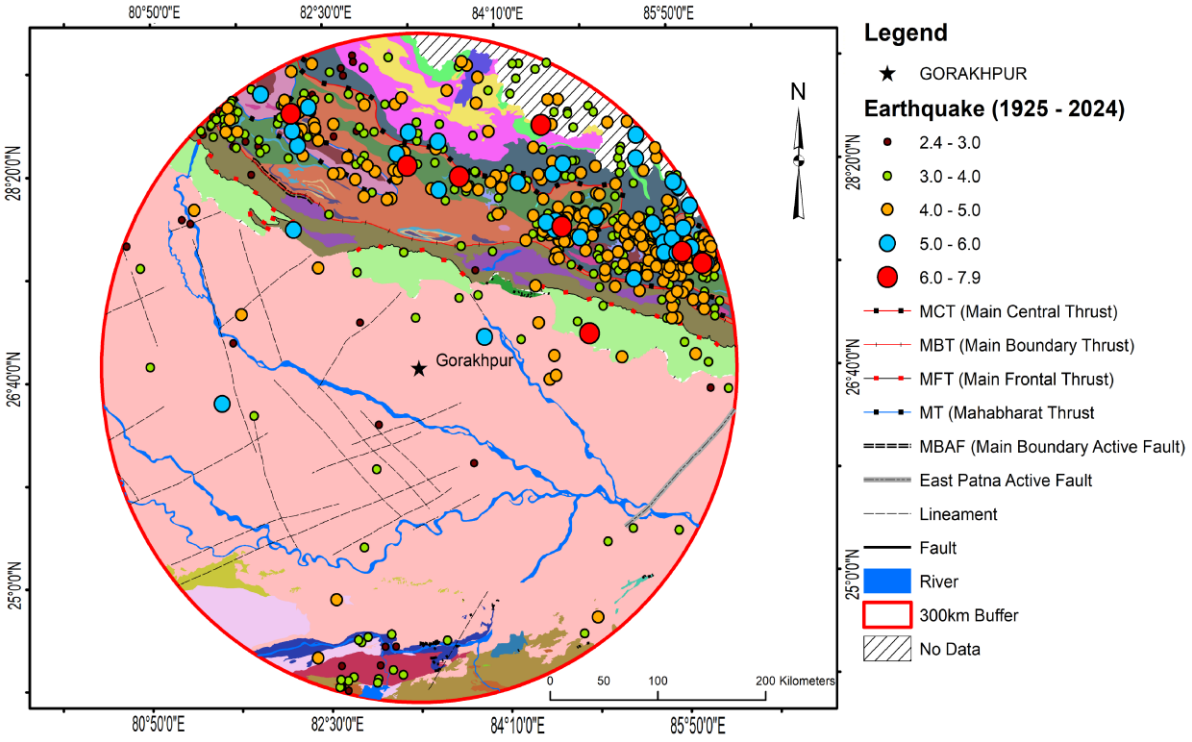

Figure 4. Seismotectonic map of North India showing major faults and historical earthquakes around 300 km of Gorakhpur study area. *(*Source: Bhukosh-GSI, 2024*;* ISC, 2024)

DATA AND METHODOLOGY

Data Sources

This study utilizes a comprehensive collection of high-resolution geophysical and geotechnical datasets to assess the subsurface conditions of Gorakhpur city. The primary data were sourced from the Bhukosh portal of the Geological Survey of India (GSI), which provides access to detailed geospatial, and subsurface information, which are essential for seismic hazard assessment (Bhukosh-GSI, 2024). Key datasets include MASW profiles and microtremor survey records. MASW profiles, acquired by Geological Survey of India (GSI) at multiple strategic locations across Gorakhpur, supply shear wave velocity (Vs) measurements that are fundamental for evaluating subsurface stiffness, stratigraphy, and identifying engineering bedrock (Park et al., 1999; GSI, 2020). Complementing this, microtremor surveys were conducted in accordance with the HVSR methodology to estimate the fundamental frequency (f_0) of local soil columns, a critical parameter for site response analysis (Nakamura, 1989; SESAME, 2004). These surveys were implemented as part of GSI's ongoing seismic microzonation initiative, which aims to delineate zones of varied seismic amplification and vulnerability within urban centres (GSI, 2020). Spatial and urban planning data, including the Gorakhpur Master Plan 2031 (Revised), boundary delineations, and land-use information, were incorporated based on resources provided by the Gorakhpur Development Authority (GDA). These documents ensure that the study's spatial framework reflects both current urban extents and anticipated expansions (GDA, 2025). Additional reports and supporting datasets were consulted from the Uttar Pradesh Avas Evam Vikas Parishad (UPAVP), GDA, and other local governmental agencies to enrich the analysis with demographic, infrastructural, and developmental context. The integration of MASW and microtremor f_0 datasets form the foundation for evaluating engineering bedrock depth and dynamic site response characteristics. This multi-source data approach enables a robust assessment of seismic vulnerability and enhances the geotechnical understanding of Gorakhpur's subsurface, supporting informed urban planning and disaster resilience strategies.

Methodology

The methodology employed in this study integrates various geophysical, geotechnical and geospatial techniques to develop comprehensive seismic hazard model for Gorakhpur city. Our approach began with collection of existing geological, geophysical, seismological, geotechnical and geospatial data from various sources, including government agencies and previous studies (Park et al., 1999; GSI, 2020). We then collected data for the city, through series of field investigations

carried out by the government agencies employing MASW and Microtremor Array Measurements (MAM) to obtain high-resolution Vs profiles. MASW profiles, collected using a 24-channel seismograph with 4.5 Hz geophones, allow for the non-invasive characterization of near-surface stratigraphy and stiffness (Park et al., 1999; Xia et al., 1999). MAM surveys employed broadband seismometers arranged in circular arrays of varying diameters to capture both shallow and deep velocity structures (Okada, 2003). These geophysical datasets were complemented by Standard Penetration Test (SPT) data from strategically located boreholes, providing constraints on soil properties and enabling correlation between Vs and SPT-N values (Ohta and Goto, 1978; GSI, 2020). Data processing involved the application of advanced signal processing techniques to extract dispersion curves from both active MASW and passive MAM seismic data. These dispersion curves were then inverted using a neighbourhood algorithm to obtain 1-D Vs profiles at each measurement location (Sambridge, 1999). The inversion process incorporated a priori information from borehole logs and geological maps to constrain the solutions.

$$Vs(30)_{Estimated} = 30/\sum \frac{v_i}{h_i} \quad (1)$$

The point measurements of Vs were then interpolated using geostatistical methods, primarily ordinary kriging, to create continuous spatial models across the study area (Isaaks and Srivastava, 1989). Cross-validation techniques were employed to assess the accuracy of the interpolation and to optimize the kriging parameters. Additionally, we integrated topographic data and surficial geology maps into our analysis to refine the spatial models, particularly in areas with limited direct measurements (GSI, 2020). Finally, we developed a GIS database to store, visualize, and analyze the spatial distribution of Vs and EBR across the city. This methodology allowed us to create robust, high-resolution models of subsurface properties, providing a solid foundation for subsequent seismic hazard and site response analyses in the region.

To assess the site response characteristics of the studied city, a combination of geophysical field investigations and empirical analyses was employed. Ambient noise recordings were carried out at over 50 sites across the city using a three-component seismometer. The HVSR technique, as proposed by Nakamura (1989), was applied to extract predominant frequency (f_0) and amplification factors (A_0) at each location. The fundamental time period (T_0) was calculated as the inverse of predominant frequency (f_0). MASW-derived $Vs30$ values were validated using borehole data wherever available. The Seismic Vulnerability Index (Kg) was computed as,

$$Kg = {A_0}^2/f_0 \quad (2)$$

Where $A_{0,}$ is the peak ground amplification factor, and f_0 is the predominant frequency of the site, typically obtained through microtremor or H/V spectral ratio analyses, providing a spatial metric of site vulnerability (Delgado et al., 2000). Spatial interpolation and mapping utilized GIS-based Inverse Distance Weighting (IDW), to generate thematic layers for each parameter, supporting the identification of seismic risk zones and the assessment of dynamic site effect variability across the city (Burrough and McDonnell, 1998).

Similarly, the Engineering Bedrock (EBR) depth modelling in this study was performed using microtremor measurements and the established empirical relation between shear wave velocity (Vs), predominant frequency (f_0), and layer thickness. For the purpose of this study, engineering bedrock was defined as the depth where $Vs \geq 760\, m/s$, as per NEHRP classification (BSSC, 2004). Ambient vibration (microtremor) data were recorded at various sites across the study area using a three-component seismometer, and the horizontal-to-vertical (H/V) spectral ratio method (Nakamura, 1989) was applied to determine the site-specific predominant frequency (f_0). This frequency represents the fundamental resonance frequency of the soil column, which is highly sensitive to the shear wave velocity profile and the depth to the underlying stiffer strata. Assuming 1-D vertical propagation of shear waves in a uniform soil layer, EBR depth (h) was computed using,

$$H_{bedrock} = \frac{Vs}{4f_0} \quad (3)$$

where Vs was set to 760 m/s (Nakamura, 1989; Ibs-von Seht and Wohlenberg, 1999).

This formula assumes a 1D vertical propagation of shear waves through a homogeneous soil layer, where Vs represents the average shear wave velocity from the surface to the bedrock, and fo is the site's predominant frequency obtained from HVSR analysis. This approach provides a first-order estimate of seismic bedrock depth. The estimated EBR values were then spatially interpolated using Inverse Distance Weighting (IDW) in a GIS environment to produce a continuous bedrock depth model across the study area, aiding in the assessment of subsurface impedance contrasts critical for seismic site response.

RESULTS AND DISCUSSION

Average shear wave velocity up to 30 m ($Vs30$)

The spatial distribution of $Vs30$ across Gorakhpur city reveals significant heterogeneity in subsurface stiffness. $Vs30$ values range from below 220 m/s in soft alluvial zones near riverbeds to over 320 m/s in relatively compacted or urbanized areas with shallow bedrock (Figure 5). According to NEHRP site classifications, much of the city falls under Site Class D (180–360 m/s), indicating a medium-to-high potential for seismic amplification. The lowest $Vs30$ values are concentrated in the

southern and south-western parts of the city, which correspond to areas with thick unconsolidated sediments. This highlights the need for reinforced design codes in these regions, especially for mid-rise buildings vulnerable to resonance effects.

Predominant Frequency (fo)

The predominant frequency map derived from HVSR analysis shows a wide variation across the study area, ranging from 1.05 Hz to 9.3 Hz (Figure 6). Low frequency zones ($f_0 \leq 2.0$ Hz) are primarily located in areas with thick soft deposits, indicating a higher likelihood of resonance with multi-storey buildings. Conversely, higher frequency zones ($f_0 \geq 4.0$ Hz) are associated with shallow or stiffer subsurface conditions, posing a threat to low-rise structures. The observed spatial pattern of f_0 aligns well with the $Vs30$ map, reaffirming the site classification results. These frequency zones help identify critical building height ranges susceptible to resonance and guide appropriate seismic design measures.

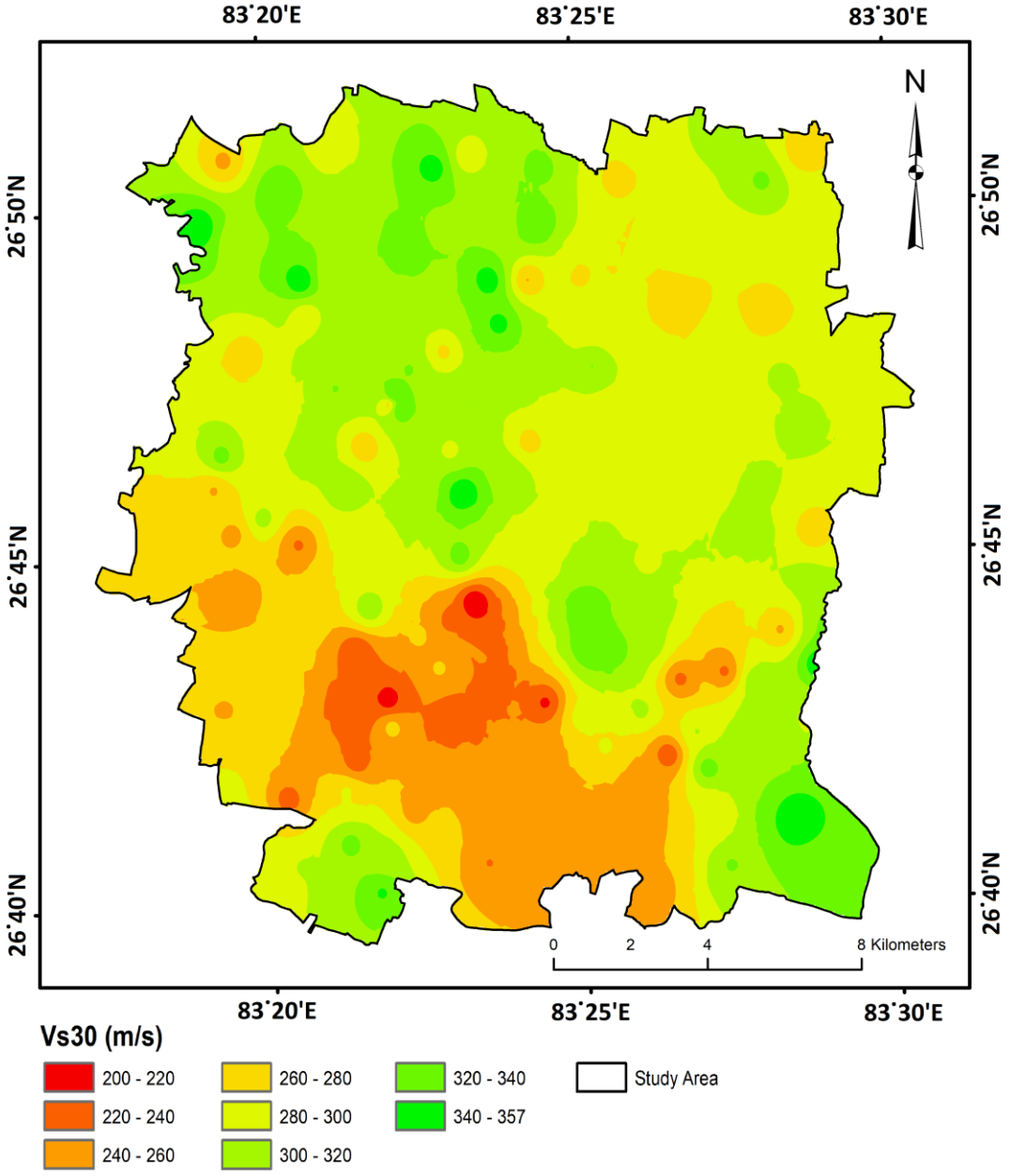

Figure 5. Average shear wave velocity (Vs30) map of Gorakhpur study Area

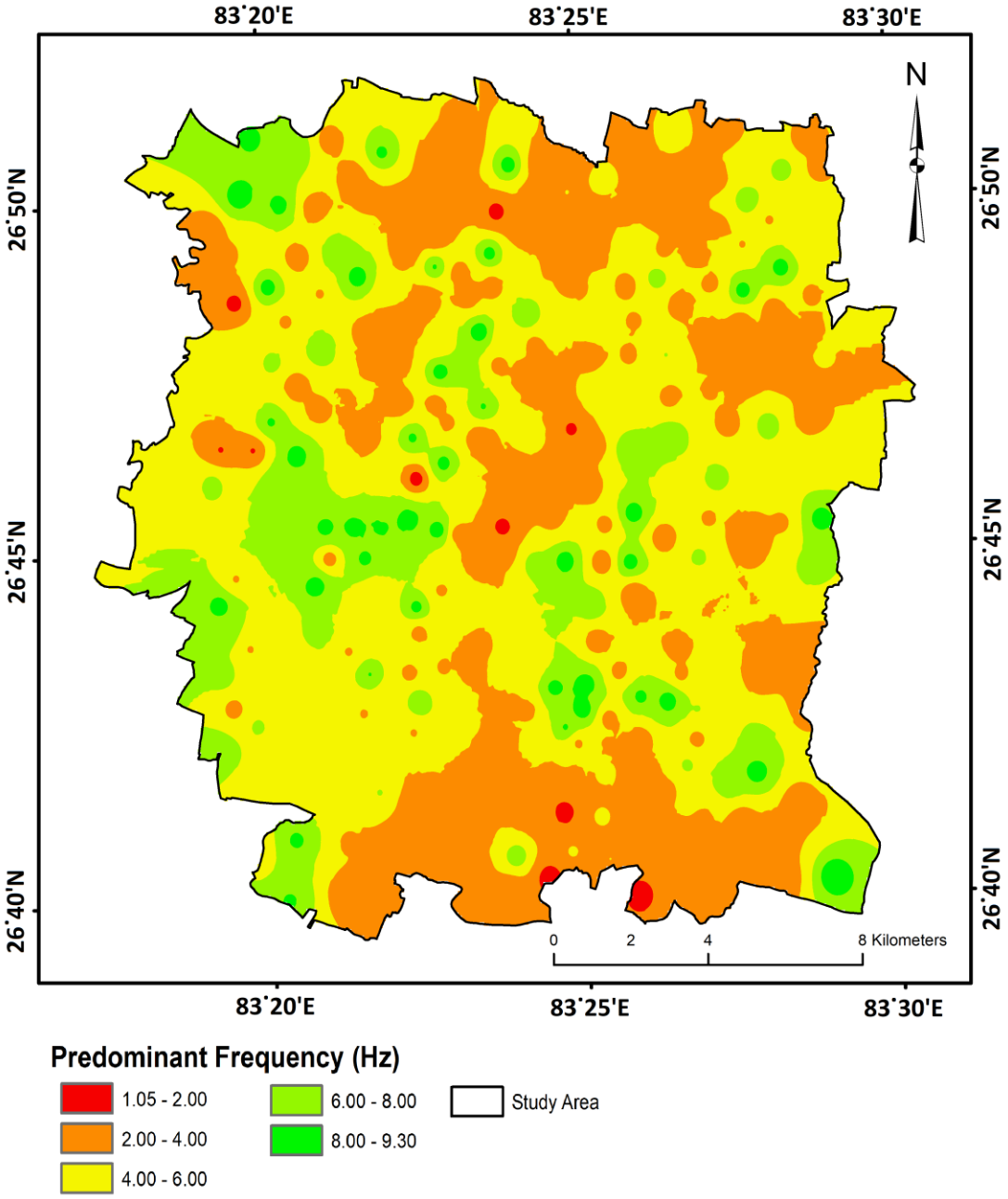

Figure 6. Predominant frequency (fo) Map of Gorakhpur study area

Fundamental time period (To)

The fundamental time period, inversely related to the predominant frequency, varies from 0.13 s to 1 s (Figure 7). Areas with longer periods (>0.6 s) correspond to soft-soil conditions and are particularly hazardous for buildings with similar structural natural periods, such as 4- to 10-storey RC frame structures. Shorter T_0 values (<0.4 s) are found in zones with stiffer soil or shallow bedrock. These periods provide important inputs for seismic code applications and for matching building resonance frequencies with local ground response. The T_0 map thus helps in aligning seismic design strategies with structural vulnerabilities in the region.

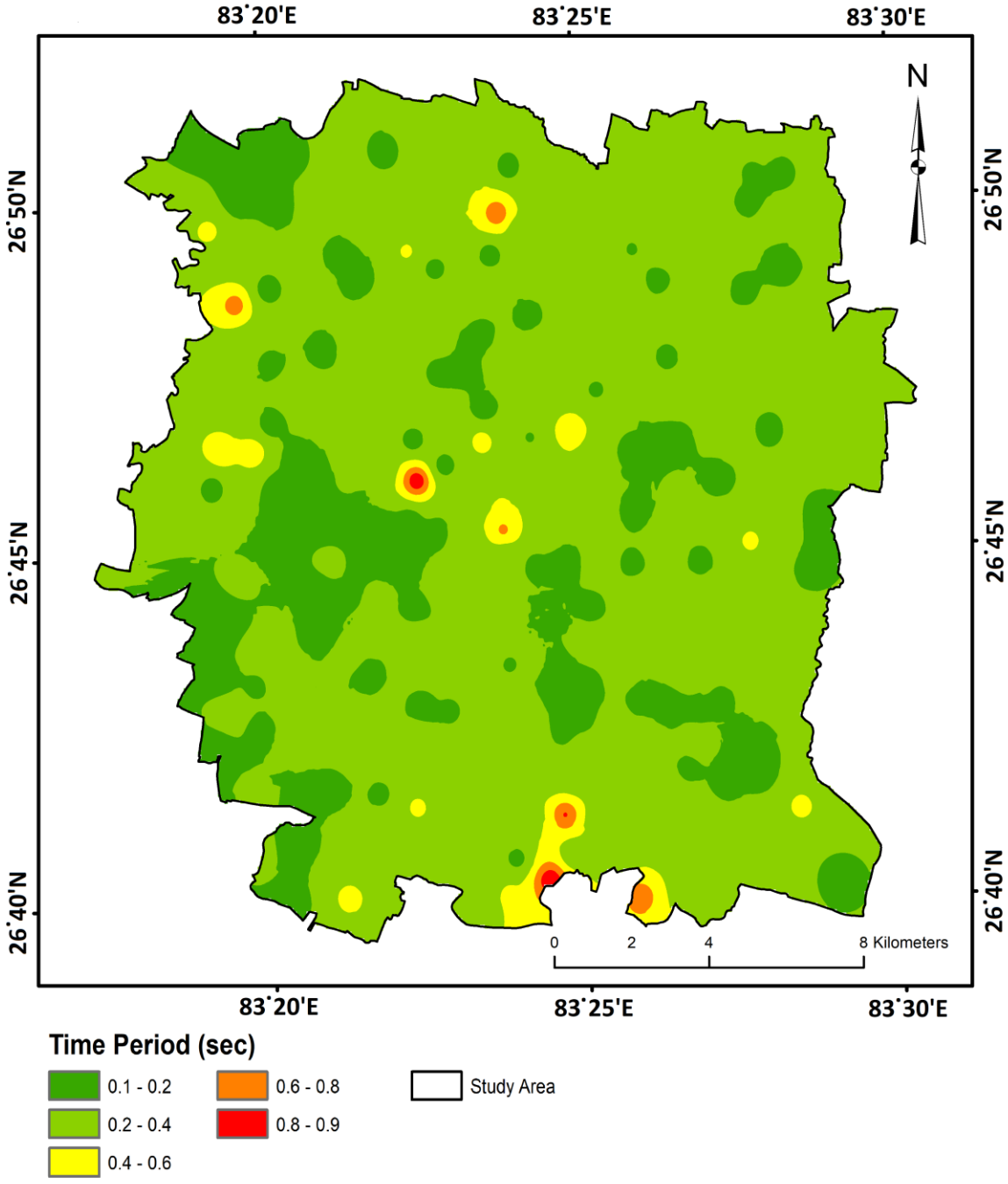

Figure 7. Time period (To) map of Gorakhpur study area

Peak amplification (***Ao***)

The peak amplification factor A_0, extracted from HVSR spectral ratios, ranges from 0.7 to 3.6, indicating varying degrees of seismic wave amplification due to site effects (Figure 8). High A_0 values are predominantly observed in soft, water-saturated alluvial regions, particularly near floodplains and low-lying terrain. The amplification is typically highest in areas with low $Vs30$ and low f_0, where resonance and wave trapping are prominent. This suggests that even moderate magnitude earthquakes could generate disproportionately high ground motion in these regions. Identification of high-amplification zones is critical for prioritizing retrofitting efforts and updating building codes in these areas.

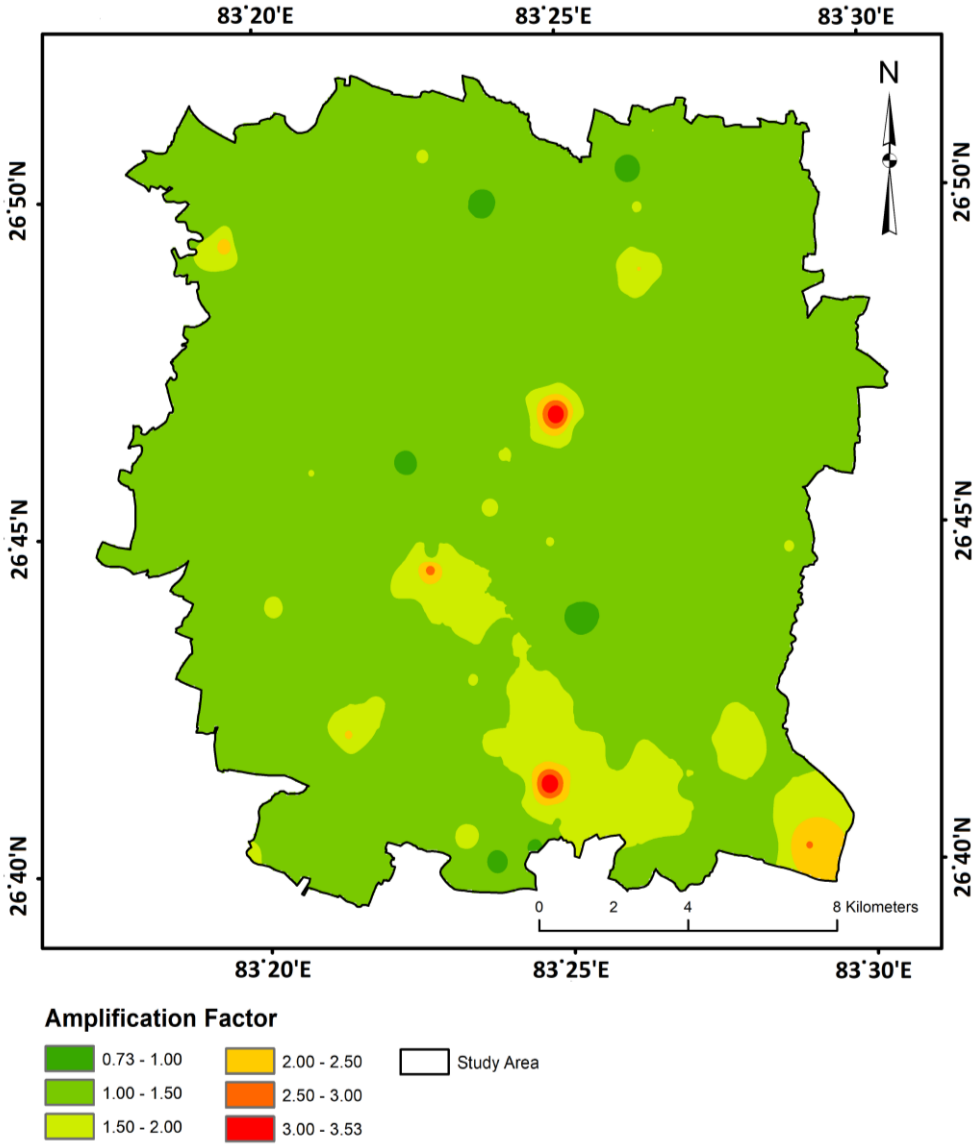

Figure 8. Amplification factor (Ao) map of Gorakhpur study area

Seismic vulnerability index (Kg)

The seismic vulnerability index integrates both the amplification factor and predominant frequency to quantify overall site vulnerability. Kg values in this city range from 0.1 to 10.1**,** with higher values indicating more vulnerable zones (Figure 9). The highest Kg values are recorded in regions with high A_0 and low f_0, suggesting a strong likelihood of resonance with mid-rise buildings and significant ground motion amplification. These zones are primarily located in the distributed parts of the city. The Kg map provides a composite and practical tool for urban seismic risk microzonation, enabling policymakers to identify and mitigate risk in the most vulnerable sectors. This index is widely used empirical parameter to assess site-specific seismic response characteristics, particularly the potential for ground motion amplification due to local soil conditions. Introduced by Nakamura (2000) and further utilized by Delgado et al. (2000), Kg is defined by the equation (2). This index provides a composite measure of seismic vulnerability by capturing both the intensity and frequency characteristics of ground motion. A higher Kg value reflects soft soils with low predominant frequency and high amplification, which are more likely to resonate with typical building frequencies, increasing seismic risk. Conversely, low Kg values represent stiffer ground with lower amplification potential. The Kg index has been effectively applied in seismic microzonation studies across various seismic regions to delineate zones of varying site vulnerability and to support earthquake-resilient urban planning (Nakamura, 2000; Delgado et al., 2000).

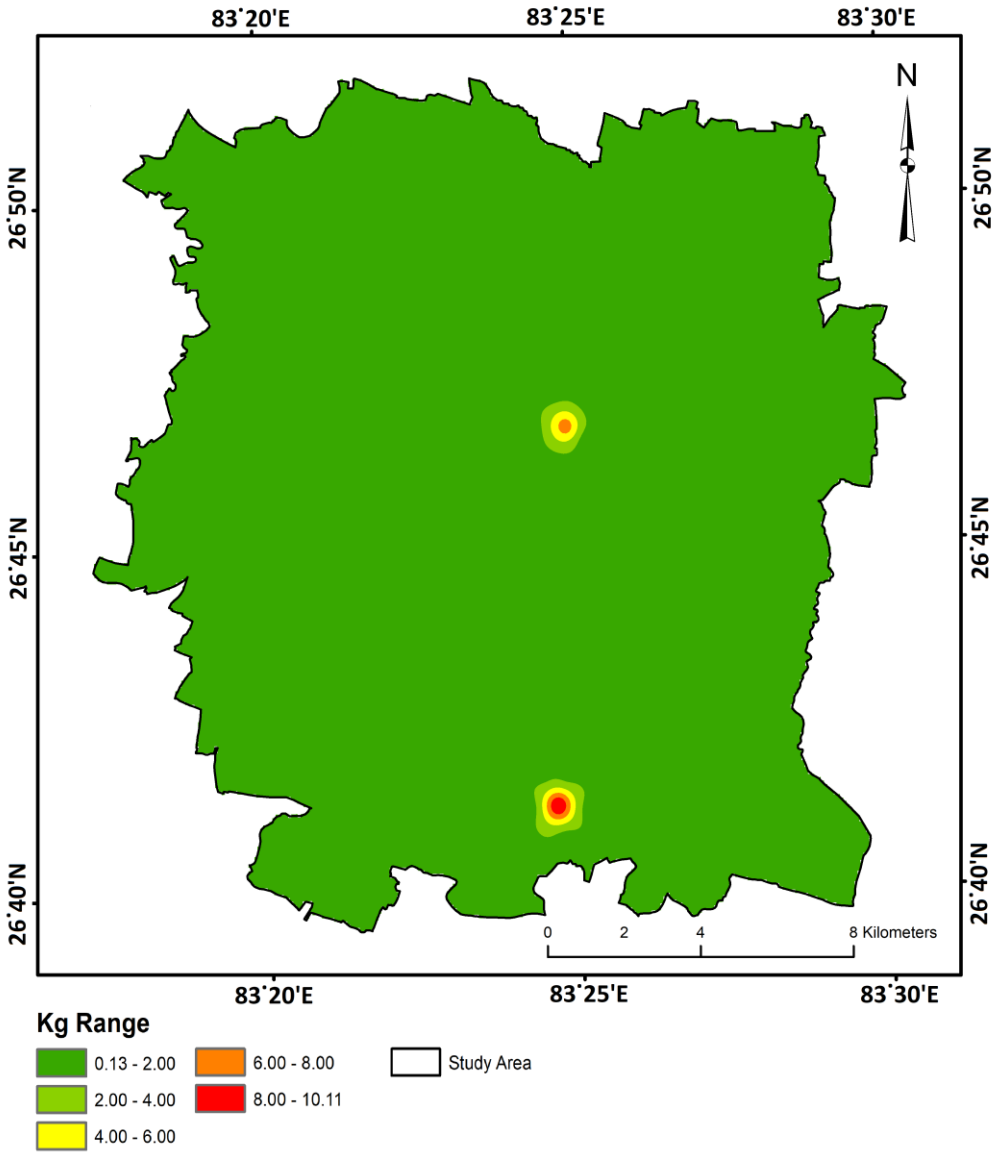

Figure 9. Seismic vulnerability index (Kg) for Gorakhpur study area

EBR modelling

Engineering bedrock is typically defined as the depth at which the shear wave velocity (Vs) reaches or exceeds 760 m/s, marking the transition from softer, unconsolidated sediments to stiffer geological formations that significantly influence seismic wave propagation. In practice, Vs is determined through methods such as MASW, downhole, or borehole geophysical surveys, and these point measurements are often interpolated using geostatistical techniques to generate spatially continuous maps across the study area.

By integrating both Vs and f_0 data, the spatial variation in EBR can be delineated and visualized across the region (Figure 10). For example, in southern areas where f_0 is $\leq$ 2 Hz and Vs is $\geq$300 m/s, sedimentary layers are typically thicker, indicating a deeper EBR. Conversely, locations with higher f_0 values of $\geq$ 4 Hz and lower Vs values of $\leq$ 260 m/s, suggest shallower bedrock conditions. The EBR in the region varies from 21 m to more than 100 m in some area, reflecting significant subsurface heterogeneity as depicted in the EBR map. Mapping these parameters together provides critical input for seismic microzonation, dynamic site response analysis, and urban infrastructure planning.

This integrated approach not only enhances the understanding of subsurface seismic impedance contrasts which govern the amplification and duration of ground motions during earthquakes, but also supports more informed decisions for engineering design and urban development.

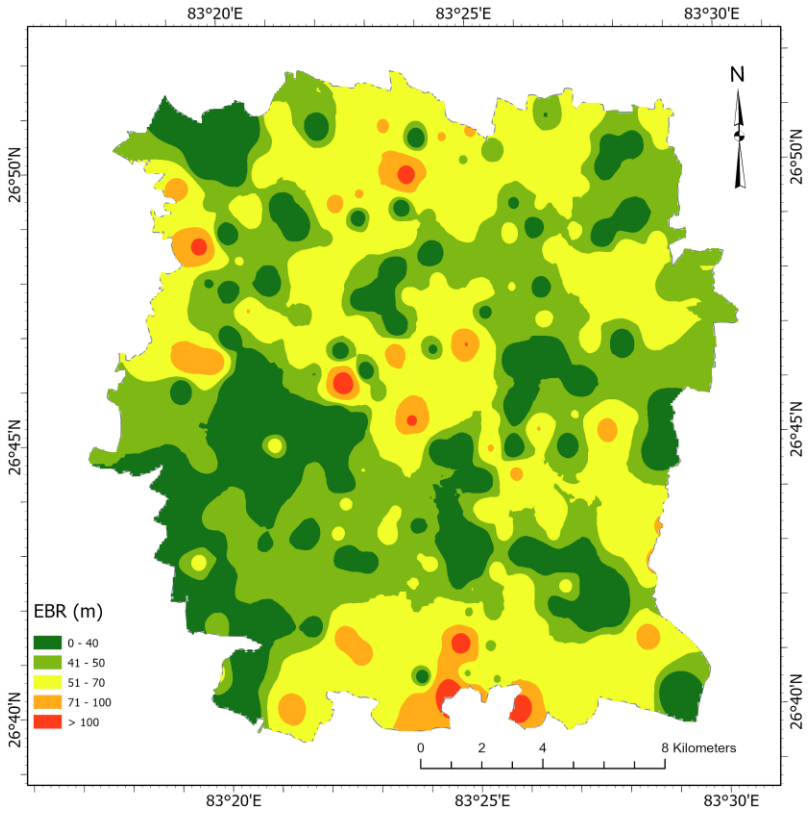

Figure 10. Engineering bedrock (EBR) map of Gorakhpur study area

Seismic hazard

The integrated analysis of dynamic site parameters reveals that the studied city is exposed to varying levels of seismic hazard**,** primarily influenced by local subsurface conditions and geomorphological settings. The spatial distribution of $Vs30$**,** f_0 **,** T_0**,** A_0 and Kg collectively delineates the city's seismic response zones. Areas with low $Vs30$ (<260 m/s), low f_0 (<2.0 Hz), long T_0 (>0.6 s), and high A_0 (>2.0), exhibit the highest seismic amplification potential**,** suggesting that even moderate earthquakes could induce intense shaking in these zones. Moreover, the Kg values exceeding 4 in certain regions clearly mark them as highly vulnerable to seismic-induced ground motion and structural resonance effects. These high-risk areas are primarily located in the central urban core and southern zones**,** where thick alluvial deposits, shallow water tables, and unconsolidated sediments dominate. Such geological settings are capable of trapping and amplifying seismic waves, significantly increasing the probability of damage to buildings, especially the mid-rise structures whose natural frequencies coincide with the site's predominant frequency. On the contrary, the western margins, where $Vs30$ and f_0 are relatively higher and Kg values are lower, show comparatively reduced seismic hazard. This spatial differentiation emphasizes the need for microzonation-based seismic planning, including tailored building design, soil improvement, and risk-sensitive land use policies across Gorakhpur City.

Shankar et al. (2021b) conducted study within the Gorakhpur Municipal Cooperation area, and reported $Vs30$ values ranging from approximately 200–360 m/s, f_0 between 0.43 and 1.02 Hz, Ao between 2.55 and 4.81, and Kg between 14 and 55. These values reflect the site conditions of the urban core. Khan et al. (2025) also conducted their study in and around Gorakhpur city, corresponding to these values. In contrast, the present study covers a much wider area, extending to the boundaries defined by the Gorakhpur Master Plan 2031. This expanded coverage reveals a broader range and higher resolution for all parameters. Specifically, $Vs30$ values in the extended area range from below 220 m/s (in the softest, riverine and peri-urban sediments) up to over 300 m/s (in compacted or shallow bedrock regions). The f_0 varies from 1 Hz in thick alluvium to as high as 3 Hz in stiffer soils and outlying regions significantly broader than the municipal-only range. Ao reach up to 3.5 in some low-lying or unconsolidated zones outside the municipal core, and Kg values exceed 10 in several high-risk peripheral areas.

These findings demonstrate that the newly included peri-urban and rural tracts under the Master Plan 2031, exhibit even lower $Vs30$, higher amplification, and broader f_0 ranges than those documented for the city center. As a result, this study provides a more comprehensive and spatially detailed assessment of seismic hazard for Gorakhpur, highlighting the necessity of area-wise microzonation for effective risk assessment and planning.

CONCLUSIONS

This study presents a detailed site-specific seismic hazard assessment of Gorakhpur city including municipal, newly urbanizing and peri-urban area, integrating multiple site parameters derived from various geophysical, geotechnical surveys and empirical analyses. The use of $Vs30$, f_0, To, A_0, and the Kg has provided a multi-dimensional understanding of the city's local site response characteristics. The spatial patterns reveal that the Gorakhpur city is marked by significant heterogeneity in subsurface stiffness and seismic response, with soft-soil zones exhibiting high amplification and long resonance periods, thereby increasing their susceptibility to structural damage during earthquakes. The derived Kg index effectively combines amplification and frequency characteristics, serving as a practical indicator for seismic hazard microzonation and urban seismic risk classification.

The EBR mapping conducted in this study reveals considerable spatial variability in bedrock depth across Gorakhpur, with EBR ranging from 21 m to over 100 m. These highlight the importance of incorporating detailed EBR profiles into seismic microzonation and foundation design, ensuring that local subsurface conditions are adequately represented in seismic hazard assessments. High hazard zones identified through this study require attention in terms of earthquake-resilient building design, infrastructure retrofitting, and urban development regulations. The findings hold valuable implications for policymakers, urban planners, civil engineers, and disaster management authorities. This research also fills a critical knowledge gap, as Gorakhpur has historically been underrepresented in site-specific seismic studies, despite being located in a significant hazardous seismic zone. Future studies may benefit from incorporating 2D and 3D geophysical modelling, nonlinear site response analysis, and probabilistic seismic hazard assessment (PSHA) for deeper insight. Nonetheless, this study lays the groundwork for risk-informed urban planning, promoting long-term resilience in one of eastern Uttar Pradesh's most rapidly developing urban centres.

Acknowledgment

Major data for the analysis were collected from the website of Geological Survey of India, Gorakhpur Development Authority, Uttar Pradesh Avas Evam Vikas Parishad, and USGS Earth explorer. The authors are thankful to the editor and two anonymous reviewers for their critical input.

Author Credit Statement

SS: Conceptualization, data collection and analysis, manuscript review and editing; AT: Conceptualization, data curation, manuscript writing, GPS: Manuscript writing, JLG: Manuscript review and editing;

Data availability

Data can be made available on a reasonable request.

Compliance with Ethical Standards

The authors declare no conflict of interest and adhere to copyright norms.

References

Anbazhagan, P., Thingbaijam, K.K.S., Nath, S.K., Narendara Kumar, J.N. and Sitharam, T.G., 2010. Multi-criteria seismic hazard evaluation for Bangalore city, India. J. Earth Sci., 38(5), 186–198.

Bajaj, K. and Anbazhagan, P., 2019. Comprehensive amplification estimation of the Indo Gangetic Basin deep soil sites in the seismically active area. Soil Dyn. Earthq. Eng., 127, 105855.

Bard, P. Y., 1999. Microtremor measurements: A tool for site effect estimation? In: Irikura, K., Kudo, K., Okada, H. and Sasatani, T. (eds), The Effects of Surface Geology on Seismic Motion, Balkema, Rotterdam, pp. 1251–1279.

Bhukosh-GSI, 2024. Geological Survey of India, https://bhukosh.gsi.gov.in/Bhukosh/MapViewer.aspx.

Bilham, R., 2004. Earthquakes in India and the Himalaya: Tectonics, geodesy and history; Ann. Geophys., 47(2), 839–858.

Bilham, R., 2009. The seismic future of cities. Bull. Earthq. Eng., 7(4), 839-887.

BIS, 1893. Indian standard criteria for earthquake resistant design of structures. Part 1: General provisions and buildings; 5th edn, New Delhi, Bureau of Indian Standards, 42p.

Bonsor, H.C., MacDonald, A.M., Ahmed, K.M., Burgess, W.G., Basharat, M., R. Calow, R.C., Dixit, A., Foster, S. S. D., Gopal, K., Lapworth, D. J., Moench, M., Mukherjee, A., Rao, M. S., Shamsudduha, M., Smith, M., Taylor, R. G., Tucker, J., van Steenbergen, A., Yadav, S. K. and Zahid, A. , 2017. Hydrogeological typologies of the Indo-Gangetic basin alluvial aquifer, South Asia. Hydrogeol. J., 25, 1377–1406.

Borcherdt, R.D., 1994. Estimates of site-dependent response spectra for design (methodology and justification). Earthq. Spectra, 10(4), 617-653.

BSSC, 2004. NEHRP recommended provisions for seismic regulations for new buildings and other structures (FEMA 450). Part 1: Provisions, 2003 edition. Building Seismic Safety Council, Washington D.C., 356 pp.

Burrough, P. A. and McDonnell, R. A., 1998. Principles of Geographical Information Systems. Oxford University Press.

Census of India, 2011. https://censusindia.gov.in/ census. website/ data/census-tables

Delgado, J., Casado, C. L., Estévez, A., Giner, J., Cuenca, A. and Molina, S., 2000. Mapping soft soils in the Segura River valley (SE Spain): a case study of microtremors as an exploration tool. J. Appl. Geophys., 45(1), 19–32.

GDA, 2025. Gorakhpur Development Authority, Official website. https://gdagkp.in/

GDA, 2024. Gorakhpur master plan 2031 (revised) report. Gorakhpur Development Authority, 2-165.

GSI, 2018. District resource map of Gorakhpur district, Uttar Pradesh. Geological Survey of India publication. https://bhukosh.gsi.gov.in/Bhukosh/Public

GSI, 2020. Seismic Microzonation studies of Gorakhpur City, Uttar Pradesh final report. Geological Survey of India. https://bhukosh.gsi.gov.in/Bhukosh/Public

Ibs-von Seht, M. and Wohlenberg, J., 1999. Microtremor measurements used to map thickness of soft sediments. Bull. Seismol. Soc. Am., 89(1), 250–259.

Isaaks, E. H. and Srivastava, R. M., 1989. An Introduction to Applied Geostatistics. Oxford University Press, 561p.

ISC, 2024. International Seismological Centre, ISC-GEM Earthquake Catalogue, https://doi.org/10.31905/d808b825

Kanamori, H., 1977. The energy release in great earthquakes. J. Geophys. Res. Atmos., 82(20), 2981–2987.

Khan, N., Chaturvedi, R., Prasad, B. and Singh, R.J., 2025. Site-Specific Seismic Hazard Assessment of Gorakhpur City, Uttar Pradesh, India: A Holistic Approach. In: Rastogi, B.K., Kothyari, G.C., Luirei, K. (eds) Natural Hazards and Risk Mitigation. Springer, Singapore, pp.191-209.

Kolathayar, S. and Sitharam, T. G., 2012. Characterization of Regional Seismic Source Zones in and around India. Seismol. Res. Lett., 83(1), 77–85.

Lermo, J. and Chávez-García, F.J., 1993. Site effect evaluation using spectral ratios with only one station. Bull. Seismol. Soc. Am., 83(5), pp.1574–1594.

Mohanty, W., Walling, M., Nath, S. and Pal, I., 2007. First Order Seismic Microzonation of Delhi, India Using Geographic Information System (GIS). Nat. Hazards, 40, 245-260.

Mukhopadhyay, D., 2018. The Making of India: Geodynamic Evolution, 2nd ed by K. S. Valdiya. Curr. Sci., 115(2), 347.

Nakamura, Y., 1989. A method for dynamic characteristics estimation of subsurface using microtremor on the ground surface. Quarterly Report of RTRI, 30(1), 25–33.

Nakamura, Y., 2000. Clear identification of fundamental idea of Nakamura's technique and its applications. In: 12th World Conference on Earthquake Engineering. Auckland, New Zealand.

Nath, S. K. and Thingbaijam, K. K. S., 2012. Probabilistic seismic hazard assessment of India. Seismol. Res. Lett., 83(1):135–149.

Nath, S.K., Thingbaijam, K.K.S., Raj, A., Shukla, K., Pal, I., Nandy, D.R., Yadav, M.K., Bansal, B.K., Dasgupta, S., Majumdar, K. and Kayal, J.R., 2007. Seismic Scenario of Guwahati City. In Proc. Int. Workshop on Earthquake Haz. Mitigations, 210-218.

Nath, S.K., Adhikari, M.D., Maiti, S.K. and Ghatak C., 2019. Earthquake hazard potential of Indo-Gangetic Foredeep: its seismotectonism, hazard, and damage modeling for the cities of Patna, Lucknow, and Varanasi. J. Seismology, 23, 725–769.

NDMA, 2010. Seismic Zones of India. National Disaster Management Authority, India.

Ohta, Y. and Goto, N., 1978. Empirical shear wave velocity equations in terms of characteristic soil indexes. Earthq. Eng. Struct. Dyn., 6(2), 167–187.

Okada, H., 2003. The Microtremor Survey Method. Society of Exploration Geophysicists.

Park, C. B., Miller, R. D. and Xia, J., 1999. Multi-channel analysis of surface waves. Geophys, 64(3), 800–808.

Sambridge, M., 1999. Geophysical inversion with a neighbourhood algorithm—I. Searching a parameter space. Geophys. J. Int., 138(2), 479–494.

Seeber, L. and Armbruster, J., 1984. Some elements of continental subduction along the Himalayan front. Tectonophys., 105(1–4), 263–278.

Seed, H. B., Romo, M. P., Sun, J. I., Jaime, A. and Lysmer, J., 1976. The Mexico earthquake of September 19, 1985—Relationships between soil conditions and earthquake ground motions. Earthq. Spectra, 2(3), 293-310.

SESAME, 2004. Guidelines for the implementation of the H/V spectral ratio technique on ambient vibrations: measurements, processing and interpretation. SESAME European Research Project.

Shankar, U., Kumari, S., Yadav, P. K., Singh, A.P. and Gupta, A. K., 2021a. Microtremor measurements in the India's holy city, Varanasi for assessment of site characteristics. Quat. Int., 585, 143–151.

Shankar, U., Yadav, P.K., Singh, A.P. Gupta, A.K., 2021b. Evaluation of site-specific characteristics using microtremor measurements in the Gorakhpur city of Uttar Pradesh, India. J. Earth Syst. Sci., 130 (188).

Shekhar, S., Tiwari, A., Gautam, J.L., and Singh, G. P., 2025. Seismic risk assessment using analytical hierarchy process: An integrated approach for Varanasi city, India. J. Indian Geophys. Union, 29(4), 260-275.

Singh, A., Singh, C. and Kennett, B., 2015. A review of crust and upper mantle structure beneath the Indian subcontinent. Tectonophys., 644–645, 1–21.

Sinha, R. and Friend, P. F.,1994. River systems and their sediment flux, Indo-Gangetic plains, Northern Bihar, India. Sedimentol., 41(4), 825–845.

Singhania, T., Jana, N. and Pal, S.K., 2026. . Seismic site characterization in the region near Korba coalfield, Chhattisgarh (India). J. Indian Geophys. Union, 30(1), in press.

Sitharam, T. G., Kumar, A., and Anbazhagan, P., 2013. Comprehensive Seismic Microzonation of Lucknow City with Detailed Geotechnical and Deep Site Response Studies. In Proc. of Indian Geotechnical Conference.

Tiwari, A., Rana, N. and Singh, G. P., 2024. A PGA amplification study of Varanasi city (India): Implications for seismic hazard assessment. India. J. Indian Geophys. Union, 28(6), 417- 429.

USGS., 2024, April 1. Earth Explorer. https://earthexplorer.usgs.gov/

Valdiya, K.S., 2010. The Making of India Geodynamic Evolution. Macmillan Publ., New York, 816p.

Wang, M. and Takada T., 2005. Macrospatial Correlation Model of Seismic Ground Motions. Earthq. Spectra, 21(4), 1137-1156.

Xia, J., Miller, R. D., Park, C. B. and Ivanov, J., 1999. Comparison of shear-wave velocity profiles inverted from multichannel surface wave, refraction, and reflection data. Soil Dyn. Earthq. Eng., 18(1), 1–11.

Received on: 8-9-2025; Revised on: 12-11-2025; Accepted on: 13-11-2025

J. Ind. Geophys. Union, 30(1) (2026), 59-69
https://doi.org/10.71122/JIGU.30(1)2026.006

Fault plane solutions of the earthquakes ($1.8 \leq M_L \leq 3.5$) in the Himachal Himalaya, India

Ankush Kumar Ruhela*, J. Das and S.C. Gupta
[1] Department of Earthquake Engineering, Indian Institute of Technology Roorkee,
Roorkee- 247667, India
*Corresponding author: aruhela@eq.iitr.ac.in

ABSTRACT

It is widely acknowledged that even when earthquakes occur inside a specific confined area, there can be significant variations in the focal mechanism solutions. Several earthquakes have been detected by broadband seismometers coupled with a digital recorder (Centaur) at six stations in the Himachal Himalaya during 2018-2019. Therefore, we addressed an approach for identifying the orientation of fault planes in the studied area. In this paper, we retrieved the fault plane solutions of 25 earthquakes using a double couple fault plane method, based on P-wave polarity readings and amplitude ratio with the help of the Seisan program. Earthquakes exhibit diverse fault plane solutions. From a total of 25 earthquakes, 3 show normal faulting, 19 show reverse faulting, and 3 show strike-slip mechanism. This is because rupture lengths for local events ($M < 3.5$) are typically in the range of a few hundred meters to a kilometer, and events may occur on faults with varying orientations. The maximum concentration of thrust faults is consistent with the trend of the Himalayan collisional zone and the location of major faults. Except for some showing a dip greater than 60°, earthquakes with precisely measured depths characterise a zone from 0.1~25 km with an average dip of about 44.6°. All focal mechanisms of events that are available within this zone, indicate a steeper dip. An earthquake that occurred near the Sundarnagar fault, shows a strike-slip mechanism. Based on this interpretation, there may be a genetic relationship between the Himalayan block above the MBT and a transverse structural feature in the underthrusting Indian plate (Sundarnagar fault). Earthquakes reveal a trend of directions concerning the T-axis and P-axis with all types of fault plane solutions.

Keywords: Earthquake, Fault plane solution, Geology and tectonics, Underthrusting, Himachal Himalaya region.

INTRODUCTION

The nature of the instantaneous faulting or earthquake process is one of the most substantial and engaging issues in seismology. The triggering mechanism and the natural mechanism of elastic strain concentration are the fundamentals of earthquake kinematics. Conventionally, the term "fault plane solution" (FPS) relates to the fault orientation, the patterns of stress release, and displacement direction, as well as the dynamic mechanism of seismic wave propagation. The FPS explains the pattern and geometry of faulting following an earthquake. The fault geometry affects the radiated amplitudes in various azimuthal directions, therefore, the FPS is derived from the polarity of the first motion or the amplitude of seismic waves. There is a persuasive explanation that the progressive stresses caused by plate movements, affect specific regions of the Earth's crust and the upper mantle. When stressed rocks suddenly fracture, strain and stress are released simultaneously, which produce seismic waves or earthquake waves. Abrupt fractures typically happen at weak spots in the stressed rocks. The blocks that move in opposite directions due to shear motion on either side of the fault plane, or fracture plane, are referred to as fractures. Since shear motions do not entail a volume change, they can happen anywhere in the brittle region of the Earth's outermost layers, even at significant depths in the upper mantle in some circumstances, where the pressure is quite high. These findings demonstrate that several events with various focal mechanism solution orientations can take place even within a very small region with a few kilometers in dimension. Teleseismic observations from the global network in the 1960s provided sufficient data to determine focal mechanisms for strong and medium-sized earthquakes that were successfully used to formulate the general theory of plate tectonics (Isacks et al., 1968). During the last 15 years, the availability of dense portable networks has permitted the field study of regional micro-seismicity, aftershocks of large earthquakes, swarms, and volcanic events. The methods used for global studies were transferred to local problems without basic modifications. Nevertheless, even in the case of a large number of seismic stations, it is difficult to set up a local network surrounding the focal sphere satisfactorily.

The tangential traction at the interface between two bodies can be inferred from their relative motion. It would be feasible to draw conclusions about the regional stress field if the tangential traction in a given area could be recognised on a variety of planes. A sudden physical change of the ground during an earthquake, releases the accumulated elastic energy. The two blocks of a fault move in opposition to one another, which results in first P motion with distinct polarities in various directions. It would be easy to identify the orientation of the two planes if the measurements from numerous equally dispersed stations around the epicenter were available by partitioning the area into four quadrants with different polarities. However, there is no way to differentiate between the fault plane and the auxiliary plane without additional information. The double-couple source method relies on this inherent ambiguity. To identify the fault plane, there are a few different approaches. A surface break on a fault caused by an earthquake must match one of the planes in the mechanism solution for the displacement and fault plane that were observed. Different approaches must be used because the majority of earthquakes do not coincide with a surface break

on land. In order to demonstrate that the slip was consistent over broad regions if it occurred in the fault plane as opposed to the auxiliary plane. McKenzie and Parker (1967) employed the horizontal projection of the slip vector to eliminate the ambiguity. Other possible sources of information include, the aftershock distribution, the radiation pattern as a function of frequency, and the ellipticity of the isoseismal lines. Various authors (Hodgson, 1957; McIntyre and Christie, 1957; Scheidegger, 1964; Shirokova, 1967) have emphasized the significance of a direction, such as the P or T axis or the null-motion direction, that is exclusively indicated by the fault-plane solution. There is no physical evidence to support this idea because the ambiguity depends on the use of distant stations and is not a characteristic of the fault motion. It is evident from the success of the ideas of paving stone tectonics (McKenzie and Parker, 1967; Morgan, 1968) that selecting between the fault plane and the auxiliary plane, is essential. The ambiguity between the fault and the auxiliary planes can be resolved with additional information from tectonics and aftershock activity data. The faults can be classified as thrust faults, normal faults, and strike-slip faults based on the nature of relative movement along the fault. Hauksson (1990) defined normal-slip vectors with rakes between -45° and -135°, reverse-slip vectors with rakes between 45° and 135°, and strike-slip vectors with rakes between 44° and -44°. Classifications of fault types along these lines are outlined in the Table 1.

Numerous authors have long explored focal mechanism solutions of earthquakes (Honda et al., 1956; Stauder, 1964; Wickens and Hodgson, 1967; Isacks and Molnar, 1971). Lately, a variety of polarity data of P wave beginning motions acquired by dense seismic networks have also been used to infer focal mechanism solutions for small events (Ishida, 1992; Yarnazaki et al., 1992; Castillo and Ellsworth, 1993; Ndikum et al., 2014). These findings demonstrate that numerous occurrences with various focal mechanism solution orientations can be found even within a confined area with dimensions of a few kilometers.

GEOLOGY AND TECTONICS OF THE HIMACHAL HIMALAYA

Himalaya is one of the seismically active regions in the globe where severe earthquakes keep on occurring on a regular basis. Although a trend has been identified, the seismicity in the Himalaya appears to be non-uniform due to the very short instrumental record. This trend is related to a narrow belt of intermediate events between the Main Central Thrust (MCT) and Main Boundary Thrust (MBT), that lies beneath the Lesser Himalaya (Barazangi and Ni, 1982). Being formed as a result of the collision of the Asian and Indian continents, the Himalaya was taken into consideration. According to Dewey and Bird (1970), the Himalaya was created by the collision of the Indian and Asian continents, surrounded by a marginal trench. They believed that further subduction was precluded by the buoyancy of the lithosphere convergence. Powell and Conaghan (1973) made modifications to Dewey and Bird (1970) continent-continent collision model, since such a collision cannot account for the formation of the present-day Himalaya. They put forth an evolutionary theory with two orogeny phases. The Cretaceous to early Tertiary (Eocene) subduction zones along the Indus-Tsangpo suture zone (ITSZ), where India and Asia collided, are related to the first phase. This phase came to an end in the Eocene, and the collision that caused the ITSZ is its immediate aftereffect. The second phase includes the emergence of intracontinental fractures inside the Indian continent and the underthrusting of the Indian continent beneath the Himalaya from the Miocene to the present time.

In the Miocene, an intracontinental main central thrust (MCT) formed south of the suture zone, and in the Pliocene, an intracontinental main boundary thrust (MBT) occurred even further south. The convergence is focused on the newest of these structures at each stage.

Table 1. Classification of fault type based on rake angle (Cronin, 2010).

S.No.	Rake	Fault type
1	0° or 180°	Pure strike-slip fault
2	90°	Pure reverse fault
3	-90°	Pure normal fault
4	-20° to 20°	Left-lateral strike-slip fault
5	20° to 70°	Reverse left-lateral oblique
6	70° to 110°	Reverse fault
7	110° to 160°	Reverse right-lateral oblique
8	-160° to 160°	Right-lateral strike-slip fault
9	-110° to -160°	Normal right-lateral oblique
10	-70° to -110°	Normal fault
11	-20° to -70°	Normal left-lateral oblique

The MCT and MBT are tectonically analogous faults of various ages in the evolutionary model. While the MCT has been dormant for over 15 million years, the MBT is now operational. In the steady-state model, the Indian Plate moved northward by underthrusting its leading edge rather than stacking behind the Himalaya when the Tethys ocean was closed along the ITSZ. There are not many differences between this form of continental subduction and oceanic subduction. Because of this, the MCT is active in the steady state model while being dormant in the evolutionary model.

Numerous plate tectonics models for the progression of the Himalaya were introduced as more evidence became available (Lefort, 1975; Molnar et al., 1977; Bird, 1978; Seeber et al., 1981; Barazangi and Ni, 1982). According to the reports, the Siwalik Himalaya, Lesser Himalaya, High Himalaya, and Tethyan Himalaya are the tectonostratigraphic domains of the Himalaya, running from south to north. Sediments from the Cambrian and Eocene make up the Tethyan Himalaya, which are rich in fossils. The MCT divides the High Himalaya from the Lesser Himalaya. The shift in the folding and metamorphism grade and style of structures is what defines the thrust. Since the middle of the Tertiary (Miocene), the MCT has been evolving. Granite and metamorphic rocks make up the High Himalaya. Some people referred to it as the central crystalline zone. The MBT divides the Lesser Himalaya from the Siwalik Himalaya. Since the Pliocene, the thrust has grown. Sedimentary rocks that have undergone metamorphosis and small amounts of volcanic rock, make up the Lesser Himalaya. These rocks also include transported, isolated fragments of central crystalline rocks. The main frontal thrust (MFT) separates the Indo-Gangetic Plain from the Siwalik Himalaya. Sandstone and mudstone are found in sequence throughout the Siwalik zone.

There have been four great Himalayan earthquakes ($M_w \geq 8$) previously: the 1897 Shillong earthquake ($M_w \geq 8.2$), the 1934 Bihar-Nepal earthquake (M_w- 8), the 1950 Assam earthquake (M_w- 8.6), and the 1905 Kangra earthquake (M_w- 7.8). There are several large magnitude ($M_w \geq 7$) earthquakes as well: the 2005 Kashmir earthquake (M_w-7.6), the 2015 Gorkha earthquake (M_w-7.8), and the 2015 Dolakha earthquake (M_w-7.3). The noticeable earthquakes that have happened in the vicinity of the research area over the past 120 years include, the 1905 Kangra earthquake (M_w-7.8), the 1945 Chamba earthquake (M_s~6.5), the 1975 Kinnaur earthquake (m_b~6.2), and the 1986 Dharamshala earthquake (m_b -5.5). Molnar and Deng (1984) reported the fault plane solution for the Kangra earthquake as a reverse faulting with a dip of 5°, strike 300°, rake $90^{\circ}$and focal depth of 15 km. Molnar and Chen (1983) reported the fault plane solution for the Kinnaur earthquake as normal faulting with a strike-slip component having a dip of 40°, strike 180°, rake 270°, and a focal depth of 9 km. In addition to these, the Garhwal Himalaya was the site of the 1991 Uttarkashi earthquake (M_w-6.7) and the 1999 Chamoli earthquake (M_w-6.5). Cotton et al. (1996) discovered the hypocentre at a depth of 14 km with a strike angle of 318°, dip angle of 11°, and rake angle of 114° for the Uttarkashi earthquake. Xu et al. (2016) reported the fault plane solution for the Chamoli earthquake as reverse faulting with a dip of 9°, strike 292°, rake $90^{\circ}$and focal depth of 15 km. The studied region is situated in the Himachal Himalaya, which contains the Himalaya's northwest region. Additionally, the studied area is characterized by the presence of local and regional tectonic features, including the Drang thrust (DT), the Ropor fault, the Reasi thrust, the Jawalamukhi thrust (JMT), the Sundarnagar fault (SNF), the Kistwar fault (KF), the Kaurik fault system (KFS), the Alakhnanda fault (AF), and the Brasar thrust. Several subsidiary thrusts, including Jwalamukhi and Drang thrusts, which have a significant spatial extent, intersect the frontal belt (between the MBT and the MFT). Figure 1 illustrates the geography of the local network of six stations installed in the Himachal Himalaya. The earthquake data are used to study the focal mechanisms and attributes of the seismic source of the region. Table 2 shows the geographical coordinates and altitudes of the recording sites.

DATA ACQUISITION

For the present study, a network has been set up around the proposed area to study the focal mechanisms of earthquakes. The digital seismographs, consisting of a short-period triaxial seismometer (20-sec compact trillium at four stations) and broadband triaxial seismometer (120-sec trillium at two stations), coupled with a digital recorder (Centaur), have been used for the recording of local earthquakes at the stations during 2018-2019. Digital data is recorded at 100 samples per second. A total of 25 local earthquakes have been identified and are considered for the study of focal mechanisms. All local events are located in the Lesser and High Himalaya. A global positioning system is included with digital stations to synchronize data to IST or UTC. The FPS of events have been drawn, based on amplitude ratios and polarities of the vertical P-wave motions. Figure 2 illustrates the time history of an event at six stations along with the ground motion.

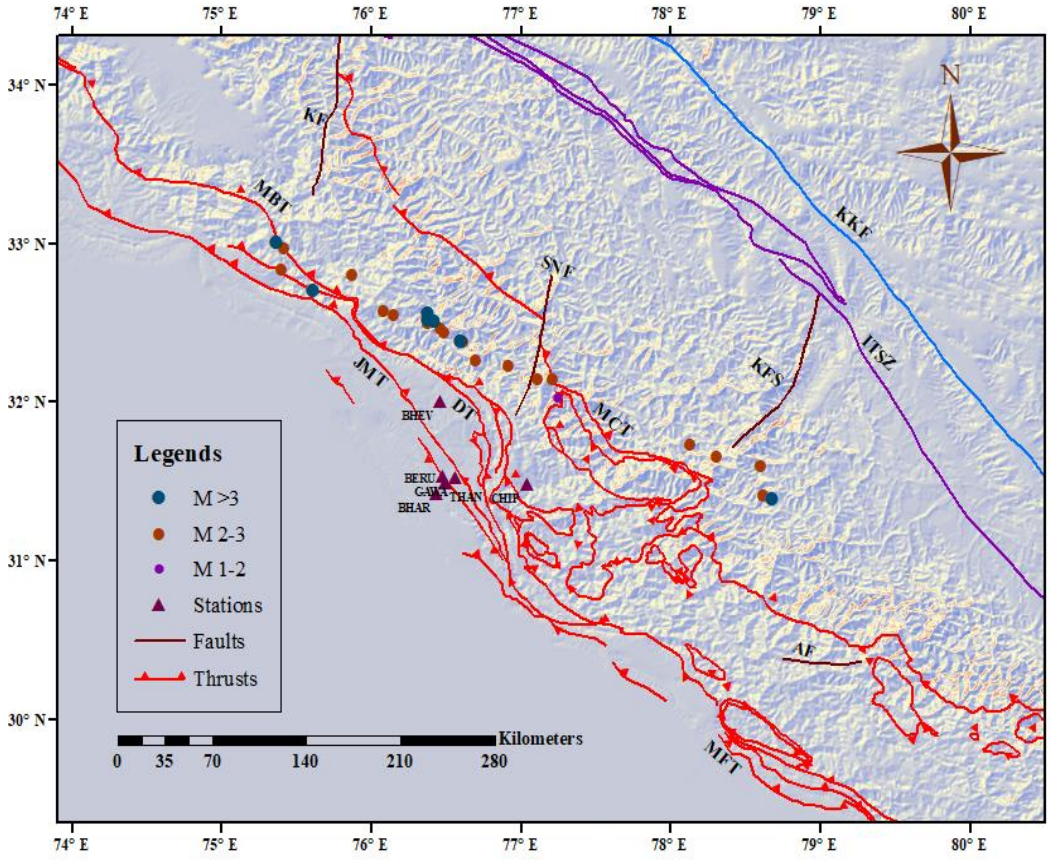

Figure 1. Map showing the study area, the tectonic features in the Himachal Himalaya with events (circles), and locations of seismic stations (triangles). KKF- Karakoram fault, ITSZ- Indus Tsangpo suture zone, KFS- Kaurik fault system, MCT- Main central thrust, MBT- Main boundary thrust, MFT- Main frontal thrust, JMT- Jwalamukhi thrust, DT- Drang thrust, SNF- Sundarnagar fault, AF- Alakhnanda fault, KF- Kishtwar fault, (Tectonic features are from Seismotectonic Atlas of India and its Environs by GSI (2000), along with SRTM-DEM).

Table 2. Geographical coordinates of the recording stations.

S. No.	Station name	Station code	Lat (°N)	Long (°E)	Elevation (m)
1.	Thana Plaun	THAN	31.49	76.50	736
2.	Gawali	GAWA	31.52	76.56	1692
3.	Bharoti	BHAR	31.42	76.44	1176
4.	Chhiprum	CHIP	31.48	77.04	2009
5.	Beru	BERU	31.53	76.48	913
6.	Bhevelli	BHEV	32.00	76.46	1525

METHODOLOGY

To monitor the earthquake activity around the studied area with specific objectives, it is necessary to have an optimum aperture of the network that encompasses the area spatially and azimuthally. The network was deployed by the Department of Earthquake Engineering, IIT, Roorkee. The events have been recorded digitally by the stations, and the phase data of these events have been used in the study. These data sets of local events have been used to locate hypocenters and to study FPS. The hypocenter parameters of 25 local events were estimated by employing the HYPOCENTER program (Lienert and Havskov, 1995), which is incorporated into the Seisan software (Havskov and Ottemoller, 2003). Because the understanding of the local velocity model of the region defined by the network, is an important requirement, the velocity model given by Chander et al. (1986) (Table 3) and modified by Kumar et al. (1994) for the Garhwal Himalaya region, is used in the present study to locate the events. This velocity model is also applicable to the Himachal Himalaya. The standard errors in the estimation of the epicenter (ERH), focal depth (ERZ), and origin time (RMS) are ERH $\leq$ 5.0 Km; ERZ $\leq$ 5.0 Km; and RMS $\leq$ 0.50 s. Tables 4 list the hypocentre parameters of 25 local events.

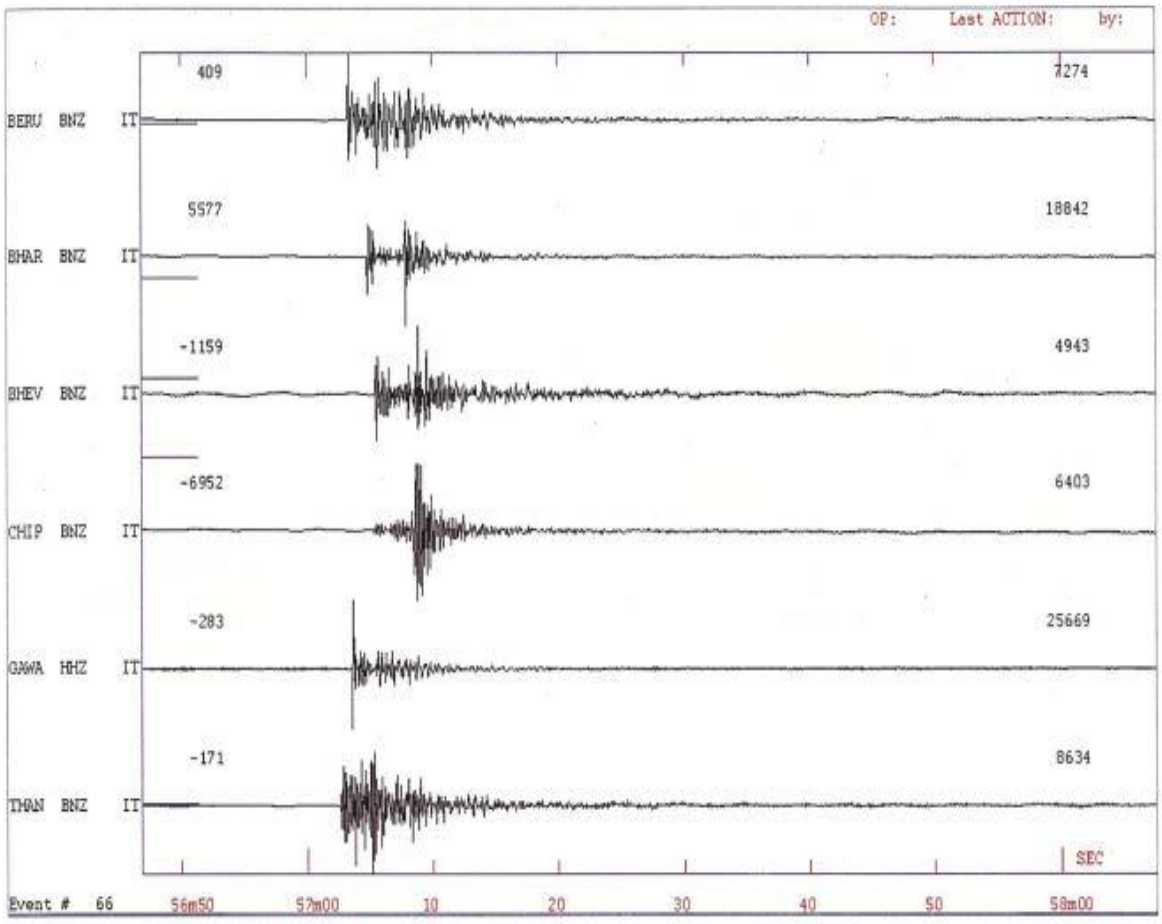

Figure 2. Example of an earthquake 5event recorded at six stations.

Table 3. Velocity model used for locating local earthquakes.

S. No.	P-wave velocity (km/s)	Depth to the top of the layer (km)
1	3	0
2	5.2	1
3	6	16
4	7.91	46

The amplitudes and polarities of the vertical P-wave motion of more than six stations are used to determine the FPS of aa the events that occurred in the Lesser and High Himachal Himalaya. The computer program FOCMEC_EXE has been utilized to calculate FPS (Snoke et al., 1984). This initiative is a component of the SEISAN software (Havskov and Ottemoller, 2003). The polarities and amplitude ratios of identical direct waves are utilized as the program's input data. The amplitude ratios are utilized to constrain the solutions, while the polarities yield the FPSs. The FOCMEC_EXE program requires two information, the maximum number of polarities and the amplitude ratio error, which should be less than a given ratio error. If there are a few badly distributed data points, changing one parameter can give a distinct result. In this study, the guiding criteria of local events for the FPS study include the number of stations that recorded an event and the geographical distributions of stations around MBT and MCT. Because it has been noted that many earthquakes fulfil this requirement, the minimal number of stations needed is set at 6.

The number of polarity errors is decided based on the values of the available data, and the value of 2 is picked from the proposed range of 0 to 5. The value of 0.1 is utilized for the maximum amplitude ratio inaccuracy. Errors are within 10%, according to this ratio. First, the P-wave recorded at different stations can show either compression or dilation first motion,

depending on whether the initial motion is toward or away from the source. A zone of compression appears ahead of a fault, and a zone of dilatation appears behind it when the initial motion of the fault is directed towards the station. This would be converted into motions up or down on a vertical component sensor, accordingly. When the direction of the first motion was on the auxiliary plane, the same pattern of compression and dilatation would have been observed. After plotting P-wave, S-wave, and amplitude data, the program performs the input data to create an effective and methodical grid search for a focal sphere. The program was used to produce possible fault-plane solutions, giving rise to the possibility of presenting several solutions. A program was then used to plot the resultant solution, yielding the fault plane solution in a beach-ball representation (Figure 3).

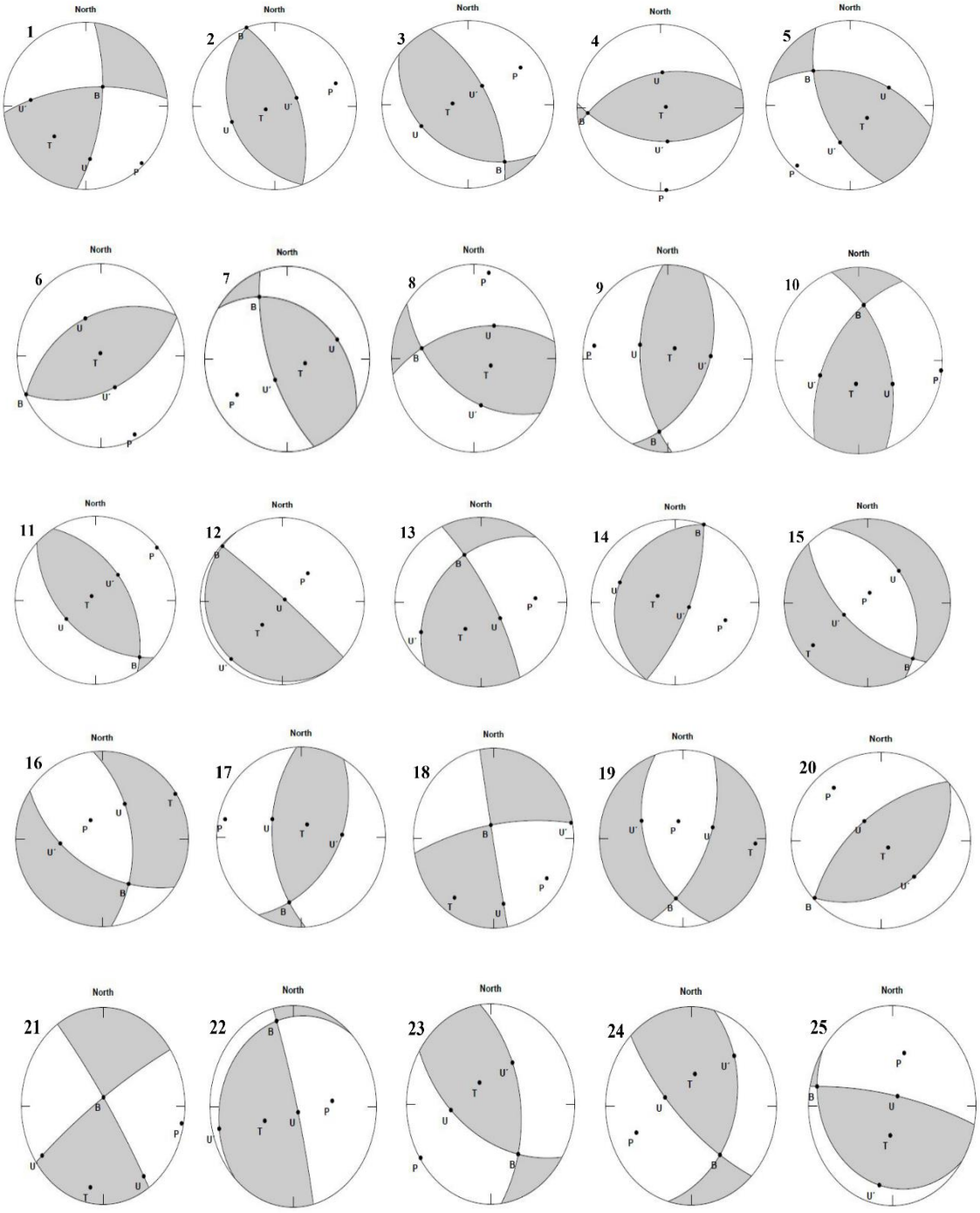

Figure 3. Beach-ball representation of the fault-plane solution of the 25 studied events.

Table 4. Hypocenter parameters of 25 local earthquakes in the Himachal Himalaya from November 2018 to March 2019.

S. No	Date (YYMMDD)	Org time HR:MN:SS	Lat (°N)	Long (°E)	Local mag. (M_L)	RMS Sec	ERH Km	ERZ Km
1	20181103	11:08:08.2	31.41	78.62	2.3	0.2	1.4	2.4
2	20181111	21:50:09.3	32.44	76.49	2.6	0.3	1.8	3.2
3	20181117	02:36:26.8	32.15	77.21	2.5	0.1	0.9	1.4
4	20181120	02:20:16.3	32.70	75.61	3.4	0.1	2.4	0.9
5	20181203	01:36:16.2	31.73	78.13	2.8	0.4	1.6	3.5
6	20181204	00:52:58.2	31.60	78.60	3.0	0.3	5.2	3.8
7	20181220	18:29:38.0	33.01	75.37	3.5	0.21	3.3	2.1
8	20181228	15:21:51.2	32.03	77.25	1.8	0.4	2.5	1.2
9	20190102	07:41:21.5	32.97	75.42	2.5	0.2	3.4	3.7
10	20190109	10:10:45.4	32.80	75.87	2.4	0.2	2.5	0.8
11	20190112	07:01:35.1	32.55	76.15	2.8	0.6	2.7	3.1
12	20190119	07:05:06.5	32.84	75.40	2.8	0.2	4.7	1.6
13	20190121	20:37:23.2	32.47	76.46	3.0	0.3	2.9	3.1
14	20190121	21:33:29.9	32.15	77.11	3.1	0.3	1.2	1.4
15	20190122	10:25:24.1	32.56	76.38	3.0	0.5	2.2	5.4
16	20190122	10:34:32.7	32.51	76.42	3.1	0.5	1.9	5.7
17	20190130	02:00:17.4	32.23	76.92	2.7	0.4	2.7	0.9
18	20190130	08:04:11.3	32.26	76.70	2.7	0.2	3.2	4.5
19	20190131	06:28:28.4	31.39	78.68	3.1	0.2	2.9	2.7
20	20190131	15:15:20.9	32.52	76.38	2.5	0.4	5.1	1.7
21	20190131	19:27:59.0	32.50	76.38	2.6	0.5	1.1	2.9
22	20190205	10:22:42.1	32.38	76.61	2.2	0.2	2.1	0.6
23	20190205	10:24:36.3	32.38	76.60	2.1	0.2	2.5	0.7
24	20190206	01:46:42.5	32.58	76.08	2.2	0.2	3.4	1.8
25	20190317	06:15:00.3	31.66	78.31	2.2	0.3	7.0	1.8

RESULTS

Figure 4 displays the locations of local events together with FPSs. The normal, reverse, and strike-slip faulting solutions are all displayed by FPSs, and it is evident that events that occur in close proximity to one another have distinct mechanisms. This happens because local events (M<3.5) typically have rupture lengths between a few hundred meters and one kilometer, and events might occur on faults that are oriented differently. From a total of 25 events, 3 events show normal faulting having both pure dip-slip component and left-lateral component, 19 events show reverse faulting with a left-lateral component, and 3 events show strike-slip mechanism. From the above discussion, Earthquakes depict all types of fault plane solutions. Interpretation of FPS concerning the T-axis and P-axis reveals the trend of direction. Orientations of the nodal planes, plunge and azimuth of the T-axis and P-axis, are tabulated in Tables 5 and 6.

DISCUSSION AND CONCLUSIONS

In this study, we investigated the focal mechanisms of 25 earthquakes in the Himachal Himalaya. We preferred the fault plane solutions with reliable P-wave first motions, because orientations of the fault planes and slip vectors are among the most crucial characteristics in the study of active tectonics of any region. Still, if more stations had recorded these events, the results would have been far more accurate. Tables 4, 5, and 6 provide the hypocenter and fault plane solution parameters. Figure 4 shows all types of solutions, and it is seen that events located very close to each other have different mechanisms. From a total of incidents, three exhibit normal faulting with a left-lateral component and a pure dip-slip component, nineteen exhibit reverse faulting with a left-lateral component, and three exhibit a strike-slip mechanism. The maximum concentration of thrust faults is consistent with the trend of the Himalayan collisional zone and the location of major faults.

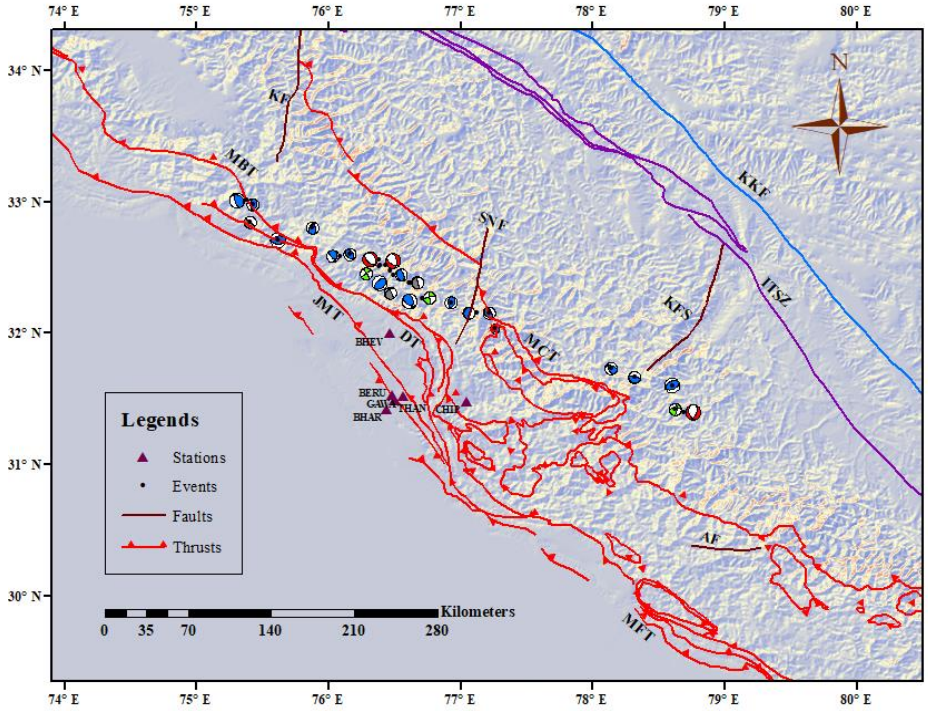

Figure 4. Beachball diagrams, in conjunction with the tectonic characteristics of the studied area, It allow for the deduction of focal mechanism solutions for well-located earthquakes based on P-wave polarity motion and amplitude ratio.

Table 5. Orientations of nodal planes obtained from FPS drawn for 25 events, Nodal plane-1 is identified as fault plane and Nodal plane-2 as auxiliary plane.

S. No.	Date (YYMMDD)	Lat (°N)	Long (°E)	Nodal plane-1			Nodal plane-2			Type of faulting
				Strike (deg.)	Dip (deg.)	Rake (deg.)	Strike (deg.)	Dip (deg.)	Rake (deg.)	
1	20181103	31.41	78.62	06	68	27	265.19	65.11	155.61	Strike-slip
2	20181111	32.44	76.49	160	32	90	340	58	90	Thrust fault
3	20181117	32.15	77.21	127	31	66	334.45	61.51	103.73	Thrust fault
4	20181120	32.70	75.61	258	45	79	93.37	46.04	100.80	Thrust fault
5	20181203	31.73	78.13	285	49	51	155.99	54.09	125.90	Thrust fault
6	20181204	31.60	78.60	244	42	89	65.35	48.01	90.90	Thrust fault
7	20181220	33.01	75.37	303	30	56	160.91	65.51	107.89	Thrust fault
8	20181228	32.03	77.25	260	54	59	125.63	46.10	125.33	Thrust fault
9	20190102	32.97	75.42	177	54	73	24.49	39.32	111.92	Thrust fault
10	20190109	32.80	75.87	341	52	53	211.75	51	127.61	Thrust fault
11	20190112	32.55	76.15	133	45	79	328.37	46.04	100.80	Thrust fault
12	20190119	32.84	75.40	312	86	89	146.05	4.12	104.01	Thrust fault
13	20190121	32.47	76.46	333	76	60	220.27	32.83	153.50	Thrust fault
14	20190121	32.15	77.11	200	20	90	20	70	90	Thrust fault
15	20190122	32.56	76.38	333	35	-75	134.89	56.36	-100.27	Normal fault
16	20190122	32.51	76.42	354	52	-53	123.25	51	-127.61	Normal fault
17	20190130	32.23	76.92	177	52	68	30.27	43.06	115.62	Thrust fault
18	20190130	32.26	76.70	170	89	-17	260.31	73	-178.95	Strike-slip
19	20190131	31.39	78.68	22	56	-64	160.90	41.84	-123.02	Normal fault
20	20190131	32.52	76.38	228	58	89	49.89	32.01	91.60	Thrust fault
21	20190131	32.50	76.38	326	84	8	235.16	82.04	173.94	Strike-slip
22	20190205	32.38	76.61	346	85	82	224.20	9.43	147.85	Thrust fault
23	20190205	32.38	76.60	122	52	53	352.75	51	127.61	Thrust fault
24	20190206	32.58	76.08	135	71	60	15.58	35.03	145.45	Thrust fault
25	20190317	31.66	78.31	281	78	85	123.82	12.99	112.30	Thrust fault

Table 6. Orientation of plunge and azimuth of T-axis and P-axis as obtained from FPS drawn for 25 events.

S. No	Date (YYMMDD)	Org time HR:MN:SS	Focal depth (Km)	P-axis		T-axis	
				Plunge (deg.)	Azimuth (deg.)	Plunge (deg.)	Azimuth (deg.)
1	20181103	11:08:08.2	22.5	1.88	135.08	34.23	46.36
2	20181111	21:50:09.3	7	13	250	77	70
3	20181117	02:36:26.8	14.4	15.87	234.40	69.85	93.62
4	20181120	02:20:16.3	5.4	0.53	355.75	82.23	261.90
5	20181203	01:36:16.2	33.4	02.82	41.46	61.48	306.26
6	20181204	00:52:58.2	16.3	3	334.71	86.92	167.29
7	20181220	18:29:38.0	7.1	18.62	57.66	64.89	281.70
8	20181228	15:21:51.2	32.2	4.29	11.42	64.96	290.65
9	20190102	07:41:21.5	13.9	07.55	279.04	74.30	217.18
10	20190109	10:10:45.4	10	0.55	96.19	61.68	7.21
11	20190112	07:01:35.1	0.1	0.53	230.75	82.23	136.90
12	20190119	07:05:06.5	17	40.99	42.94	48.99	40.92
13	20190121	20:37:23.2	7	25.03	85.97	49.93	29.69
14	20190121	21:33:29.9	18	25	290	65	110
15	20190122	10:25:24.1	6.1	76.16	193.06	10.81	52.26
16	20190122	10:34:32.7	8.6	61.68	147.79	0.55	58.81
17	20190130	02:00:17.4	2.2	4.66	282.41	72.17	207.10
18	20190130	08:04:11.3	43.1	12.65	303.87	11.21	216.42
19	20190131	06:28:28.4	22.3	67.26	165.33	7.56	93.78
20	20190131	15:15:20.9	6.1	12.99	318.73	76.98	314.86
21	20190131	19:27:59.0	0.6	1.37	100.46	9.89	10.70
22	20190205	10:22:42.1	9.9	39.49	83.33	49.39	67.30
23	20190205	10:24:36.3	10	0.55	237.19	61.68	148.21
24	20190206	01:46:42.5	2.4	20.41	247.16	54.02	188
25	20190317	06:15:00.3	26.2	32.82	15.21	56.72	4.55

Previous studies suggested that the Ropar-Manali fault, earlier recognized as a lineament, shows dextral strike-slip motion and is transverse to the regional Himalayan strike. The fault extends from Ropar through Sundarnagar, Mandi, and Kullu to Manali in Himachal Pradesh. An earthquake with strike-slip motion is close to the Sundarnagar fault. There may be a genetic relationship between the Himalayan block above the MBT and a transverse structural feature in the underthrusting Indian plate (Sundarnagar fault). The MCT and MBT are tectonically analogous faults of various ages. Some earthquakes show normal faulting above the MCT, and some thrust events are very close to the west and east sides of the MBT. Therefore, considering the orientation of fault planes in the beachball representation of the fault plane solutions, they are oriented with the Himalayan thrusts and faults. Tandon and Srivastava (1975) conducted an investigation for three regions, namely Kashmir, Central Himalaya and northeast India, including Assam. They determined the fault plane solutions of 30 events. From theses events, 4 events show normal faulting, 25 events show reverse faulting with a left-lateral component, and 1 event shows a strike-slip mechanism. Molnar and Deng (1984) conducted an investigation into the faulting process associated with large earthquakes and the corresponding average deformation rates across Central and Eastern Asia. Their analysis demonstrated that the majority of the large earthquakes are characterized by thrust faulting, a finding that aligns well with the results of the present study.

The direction of the trend is revealed by interpreting FPS in relation to the T- and P-axes. According to the T-axis, 10 events have azimuths between 4.55^0 to 70^0 that trend in the north-east direction, 6 events have azimuths between 93.62^0 to 167.29^0 that trend in the south-east direction, 5 events have azimuths between 188^0 to 261.90^0 that trend in the south-west direction, and 4 events have azimuths between 281^0 to 314.86^0 that trend in the north-west direction, respectively. According to the P-axis, 6 events have azimuths between 193^0 to 250^0 that trend in the south-west direction. P-axis azimuths of 5 events vary from 96.19^0 to 165.33^0 that trend in the south-east direction. Remaining, each 7 events have azimuths between 11.42^0 to 85.97^0, and 279.04^0 to 355.75^0 that trend in north-east and north-west directions, respectively.

Acknowledgments

The authors are grateful to the organizations and individual sections that provided the data and information used in the present study. The authors express their gratitude to the Department of Earthquake Engineering, IIT Roorkee, for providing the data and research facilities. The authors are appreciative of their support.

Author credit statement

Ankush Kumar Ruhela has done the formal analysis and research work presented in this paper using Seisan software for focal mechanisms. J. Das and S.C. Gupta supervised the whole research work and helped in the planning and execution of the manuscript. All the named authors provided their critical feedback on data interpretation and supported the improvement of the manuscript.

Data Availability

The data used in the study is provided by the Department of Earthquake Engineering, IIT Roorkee, India.

Compliance with ethical standards

The authors declare that there are no known financial conflicts of interest or personal relationships that could have influenced the work presented in the paper. They adhere to copyright norms

References

Barazangi, M. and Ni, J., 1982. Velocities and propagation characteristics of Pn and Sn beneath the Himalayan arc and Tibetan plateau: Possible evidence for underthrusting of Indian continental lithosphere beneath Tibet. Geology, 10(4), 179-185.

Bird, P., 1978. Initiation of intracontinental subduction in the Himalaya. J. Geophys. Res.,Solid Earth, 83(B10), 4975-4987.

Castillo, D.A. and Ellsworth, W.L., 1993. Seismotectonics of the San Andreas Fault systembetween Point Arena and Cape Mendocino in north California: Implications for the development and evolution of a young transform. J. Geophys. Res., 98, 6543-6560.

Chander, R., Sarkar, I., Khattri, K. N. and Gaur, V. K., 1986. Upper crustal compressional wave velocity in the Garhwal Himalaya. Tectonophysics, 124, 133–140.

Cotton, F., Campillo, M., Deschamps, A. and Rastogi, B. K., 1996. Rupture history and seismotectonics of the 1991 Uttarkashi, Himalaya arthquake. Tectonophysics, 258(1-4), 35-51.

Cronin, V.S., 2010. A primer on focal mechanism solutions for geologists. Science Education Resource Center, Carleton College, http:serc.carleton.edu/files/NAGT workshops/ structure 04/focal_mechanism_primer.pdf.

Dewey, J. F. and Bird, J. M., 1970. Mountain belts and the new global tectonics. J. Geophys. Res., 75(14), 2625-2647.

GSI, 2000. Geological Survey of India, Seismotectonic atlas of India and its environs.

Hauksson, E., 1990. Earthquakes, faulting, and stress in the Los Angeles basin. J. Geophys. Res., Solid Earth, 95(B10), 15365-15394.

Havskov, J. and Ottemoller, L., 2003. SEISAN: the earthquake analysis softwares for windows, Solaris and Linux, version 8.0. Norway: Institute of Solid Earth Physics, University of Bergen.

Hodgson, J. H., 1957. The nature of faulting in large earthquakes. Bull. Geol. Soc. Am., 68, 611- 644.

Honda, H., Masatsuka, A. and Emura, K., 1956. On the mechanism of the earthquakes and the stress producing them in Japan and its vicinity. Sic Rep. Tohoku University, Set. 5, 8, 186-205.

Isacks, B.L. and Molnar, P., 1971. Distribution of stresses in the descending lithosphere from a global survey of focal-mechanism solutions of mantle earthquakes, Rev. Geophys., 9, 103-174.

Isacks, B., Oliver, J. and Sykes, L. R., 1968. Seismology and the new global tectonics. J. Geophys. Res., 73(18), 5855-5899.

Ishida, M., 1992. Geometry and relative motion of the Philippine Sea plate and Pacific plate beneath the Kanto-Tokai district, Japan. J. Geophys. Res., 97, 489-513.

Kumar, A., Pandey, A.D., Sharma, M.L., Gupta, S.C., Verma, A.K., and Gupta, B.K., 1994. Processing and preliminary interpretation of digital data obtained from a digital seismic array in Garhwal Himalaya. Symposium on Earthquake Engineering, University of Roorkee, India, Vol. 1, 141-152.

LeFort, P., 1975. Himalayas: The collided range, present knowledge of the continental arc: Am. J. Sci., 275-A, 1-44.

Lienert, B.R. and Havskov, J., 1995. A computer program for locating earthquakes both locally and globally. Seism. Res. Lett., 66 (5), 26-36.

McIntyre, D. B. and Christie, J., 1957. A discussion of "The nature of Faulting in Large Earthquakes". Bull. Geol. Soc. Am., 68, 645-652.

McKenzie, D. P. and Parker, R. L., 1967. The North Pacific: an example of tectonics on a sphere. Nature, 216, 1276-1280.

Molnar, P. and Chen, W. P., 1983. Focal depths and fault plane solutions of earthquakes under the Tibetan Plateau. J. Geophys. Res., 88, 1180 – 1196.

Molnar, P. and Qidong, D., 1984. Faulting associated with large earthquakes and the average rate of deformation in central and eastern Asia. J. Geophys.Res.,Solid Earth, 89(B7), 6203-6227.

Molnar, P., Chen, W. P., Fitch, T. J., Tapponnier, P., Warsi, W. E. K. and Wu, F. T., 1977. Structure and tectonics of Himalaya: A brief summary of relevant geophysical observations, Colloq. Int CNRS, Ecologie et Geologic de the Himalaya, Vol. 268, 269-294.

Morgan, W. J., 1968. Rises, trenches, great faults, and crustal blocks. J. Geophys. Res.,73, 1959- 1982.

Ndikum, E.N., Tabod, C.T., Tokam, A.K. and Essimbi, B.Z., 2014. Fault-plane solution of the earthquake of 19 march 2005 in Monatele (Cameroon). Open J. Geology. 4, 289-293.

Powell, C. M. and Conaghan, P. J., 1973. Plate tectonics and the Himalayas. Earth and Planet. Sci. Lett., 20(1), 1-12.

Scheidegger, A. E., 1964. The tectonic stress and tectonic motion direction in Europe and Western Asia as calculated from earthquake fault plane solutions. Bull. Seism. Soc. Am., 54, 1519-1528.

Seeber, L., Quittmeyer, R. and Armbruster, J.G., 1981. Seismicity and continental subduction in the Himalayan arc, in Zagros, Hindu Kush, Himalaya, Geodynamic Evolution, Geodyn. Ser., vol. 3, edited by H.K. Gupta and F.M. Delany, pp. 215-242, AGU, Washington, D.C.

Shirokova, E. I., 1967. General features in the orientation of principal stresses in earthquake foci in the Mediterranean-Asian seismic belt. Izv. Akad. Naul~ S.S.S.R. (Physics of the Solid Earth) 12-22 (English translation).

Snoke, J.A., Munsey, J.W., Teague, A.C. and Bollinger, G.A., 1984. A program for focal mechanism determination by combined use of polarity and Sv-P amplitude ratio data, Earthquake notes, 55-3-15.

Stauder, W., 1964. A comparison of multiple solutions of focal mechanisms. Bull.Seism. Soc. Am., 54, 927-937.

Tandon, A. N. and Srivastava, N., 1975. Fault plane solutions as related to known geological faults in and near India. Annals of Geophys., 28(1), 14-27.

Wickens, A.J. and Hodgson, J.H., 1967. Computer re-evaluation of earthquake mechanism solutions. Publ. Dom. Obs. Ottawa, 33(1), 1-560.

Xu, W., Burgmann, R. and Li, Z., 2016. An improved geodetic source model for the 1999 Mw 6.3 Chamoli earthquake, India. Geophys. J. Int., 205, 236–242. https://doi.org/10.1093/gji/ggw016.

Yamazaki, F., Horiuchi, S., Ito, K. and Moriya, T., 1992. Focal Mechanism Analyses of Aftershocks of the 1984 Western Nagano Prefecture Earthquake. J. Phys. Earth, 40, 327-341.

Received on: 9-10-2024; Revised on: 29-11-2025; Accepted on: 30-11-2025

J. Ind. Geophys. Union, 30(1) (2026), 70-77
https://doi.org/10.71122/JIGU.30(1)2026.007

Deep learning-based model for groundwater quality prediction in Kanyakumari District, Tamil Nadu, India.

Annie Jose* and Srinivas Y
Centre for Geotechnology, Manonmaniam Sundaranar University, Tirunelveli – 627 012, Tamil Nadu (India)
*Corresponding Author: anniejose1996@gmail.com

ABSTRACT

In this study, a Deep learning-based model, Stochastic Neural Network (SNN), which excels in handling uncertain and complex data, is customized to predict groundwater quality in the Kanyakumari District of Tamil Nadu (India), where groundwater is considered a critical source for drinking and agricultural purposes. The SNN model captures the stochastic nature of the data and provides reliable predictions by simulating multiple possible outcomes, making the model ideal for groundwater quality prediction. A range of groundwater quality indicators, such as pH, EC, TDS, etc. were used to train the model. Rainfall patterns were found to have a considerable impact on water quality over a ten-year period, emphasizing the importance to include seasonal data into prediction models. Hence, rainfall data was also included in order to evaluate its impact on groundwater quality. The deep learning model demonstrated its effectiveness with 95% prediction accuracy. The model's capacity to distinguish between classes was evaluated by the Classification Report, Receiver Operating Characteristic (ROC) curves, Area Under the Curve (AUC) values and the confusion matrix. In addition to this, Cross-validation (CV) was employed to confirm the model's performance and also to test the reliability of the results. This study provides an efficient method that can assist in sustainable use of groundwater resources.

Key Words: Deep learning, Groundwater quality prediction, Rainfall, Stochastic Neural Network, Kanyakumari District, Public Health.

INTRODUCTION

Water is a necessity for survival, economic development and human well-being, hence access to clean water is a fundamental right (Kirsch, 2006). With rising living standards, population demands, and expanding domestic, industrial, agricultural, and urban activities, water consumption has increased, resulting in overuse and deterioration of both surface and groundwater resources (Gilli et al., 2012). Groundwater in particular, is difficult to manage and more susceptible to contamination from both geogenic and anthropogenic sources (Karamouz et al., 2011). As water easily dissolves substances, monitoring groundwater quality changes is critical for its protection and conservation. Exceeding permissible limits of physicochemical parameters, may pose serious health risks (Karnena and Saritha, 2019). Groundwater is vital for drinking as well irrigation, especially in the study area of Kanyakumari, in Tamil Nadu and hence proper quality monitoring is critical for sustainable resource management. Given the complex and variable nature of groundwater, which is influenced by both natural and human influences (Giao et al., 2023), traditional evaluation methods based on laboratory testing and statistical analysis can be time and resource draining, especially for large datasets. To address these limitations, this study utilizes data-driven modelling to improve the accuracy and reliability of groundwater quality predictions.

Over the last decade, Machine Learning (ML) has grown rapidly in groundwater quality modeling, as ML algorithms learn patterns directly from data rather than depending on pre-set equations, allowing for precise predictions of water quality parameters (Haggerty et al., 2023). Deep Learning (DL), a subset of machine learning, inspired by neural processing in the human brain, employs multilayer neural networks to evaluate complicated, structured data (Chollet, 2017). These developments indicate great potential in groundwater research, as neural networks often deliver accurate and dependable predictions. They have been extensively used to predict groundwater levels, evaluate water quality near shale gas reserves, improve MODFLOW simulations, predict nitrate contamination and model groundwater drawdown (Lohani and Krishnan, 2015; Kulisz et al., 2021; Gholami and Sahour, 2022; Stylianoudaki et al., 2022; Kishor et al., 2025). All studies indicate that the neural networks may effectively assess groundwater quality and quantity, but most studies utilize conventional Artificial Neural Networks (ANN), which do not capture or forecast uncertainty. Stochastic Neural Networks (SNNs), on the other hand, can reduce overfitting and capture uncertainty. Despite being widely used in domains such as, finance (Kalariya et al., 2022), civil engineering (Emig et al., 2023), microbiology (Sarmadi et al., 2022), and physics (Schneider et al., 2017), their use in groundwater research remains limited. SNN's strength lies in making probabilistic predictions and adapting to changing environmental conditions. In this study, SNN with Monte Carlo Dropout, was used to simulate numerous possibilities per input, resulting in uncertainty-aware groundwater quality prediction. Rainfall was also included to better express climate-related effects on groundwater chemistry. The main objective of the study is to create a sophisticated deep learning model that is specifically suited to capturing the diversity and complexity present in groundwater quality data, to study the prediction reliability using stochastic inference and assess how rainfall affects the accuracy of water quality classification in the Kanyakumari District of Tamil Nadu, India.

STUDY AREA

The study area, Kanyakumari District (Figure 1), is one of those areas that heavily relies on groundwater as a freshwater

supply for agriculture and drinking. The study area falls between 8º 03' to 8º 35 ' N and 77º 15' to 77º 36' E, which is located in the southernmost tip of India. It is bounded by three water bodies: Indian Ocean, Arabian Sea and the Bay of Bengal. The study area enjoys both northeast (NE) and southwest (SW) monsoon seasons, resulting in about receiving an approximate 1448.6 mm of precipitation on average, every year (District Statistical Handbook, 2021-2022). According to GSI (2005), groundwater is present in almost all the formations. The studied district is composed of 80% fractured hard rocks and 20% sedimentary terrain.

METHODOLOGY

Data preparation

The overall methodology of the study is shown in the Figure 2. A decade (2013-2022) worth of groundwater quality data, which comprises of 65 locations and rainfall data from 25 rain gauge stations, were collected from State Ground and Surface Water Resources Data Centre, "Public Works Department", Government of Tamil Nadu. Rainfall patterns are one of those parameters that has a greater influence in the groundwater quality. And hence, rainfall is also added along with groundwater quality parameters such as pH, electrical conductivity (EC), total dissolved solids (TDS), major cations such as Na^+, K^+, Ca^{2+}, Mg^{2+}, total hardness (TH, calculated as the sum of Ca^{2+} and Mg^{2+}), and anions such as SO_4^{2-}, Cl^-, HCO_3^-, CO_3^{2-}, F^-, NO_2^- +NO_3^-. Information such as location, name of the village and the date of collection were also taken along with the parameters. Over the course of the ten-year period, a total of 645 data points were obtained from groundwater samples taken from 65 monitoring wells, spread throughout the study region. Samples were taken twice a year, in the pre-monsoon and post-monsoon seasons, and each site provided several observations. Theissen Polygon Method, which allocates rainfall values to each sampling location according to physical proximity and area of effect, was used to integrate rainfall data with the groundwater sampling sites. The raw data were unsuitable for use without pre-processing and hence, it is carried out by handling missing values and any type of inconsistencies in the dataset was removed to maintain the quality of the data. Missing data and outliers were addressed using simple deletion to assure the accuracy of the analysis and only complete and validated records were included. Outlier detection was also aided by the Calculation of Ion Balance Error (IBE) and data points with notable charge imbalance excluded.

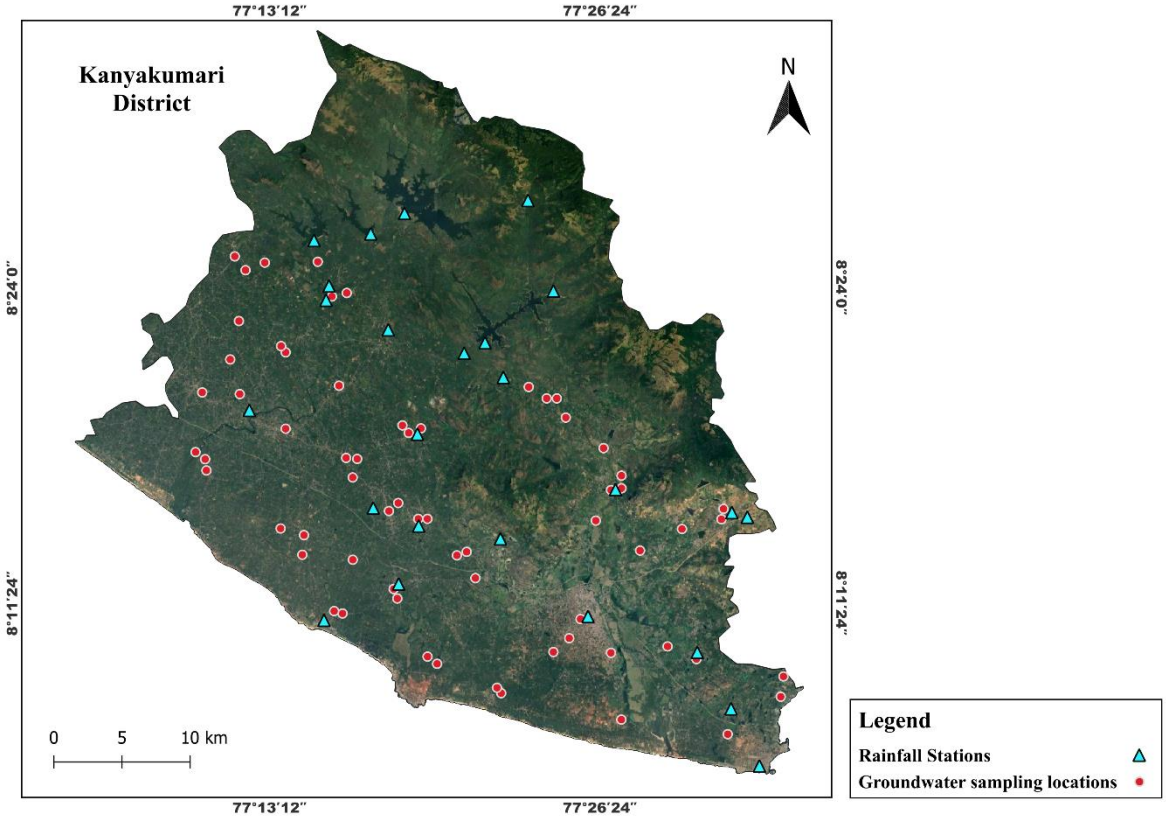

Figure 1. Map showing the distribution of sampling locations and rainfall monitoring stations across the study area in the Kanyakumari District, Tamil Nadu, India.

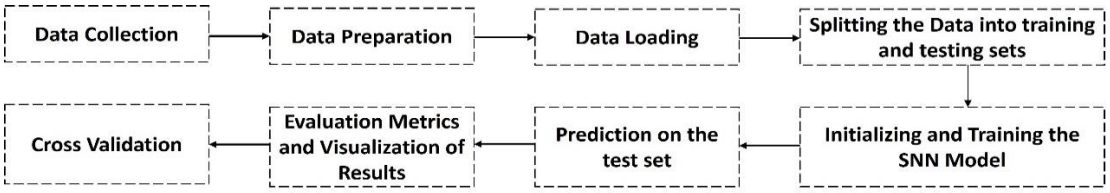

Figure 2. Methodological framework outlining the sequential processes involved in the study.

IBE also known as Charge Balance Error (CBE), is a quality control measure used to evaluate the reliability of analytical data in water chemistry analysis and also to remove any other inconsistencies in the dataset. The calculated IBE had to fall within the permissible range of ±10% (Domenico and Schwartz, 1990). Then, Water Quality Index (WQI) for drinking is calculated on the relation based on BIS (2012) and WHO (2011), which is followed in many studies for example, Vasanthavigar et al. (2010). The purpose of computing Drinking Water Quality Index (DWQI) is to help the researchers, policymakers and the general public to quickly assess the safety of drinking water and make knowledgeable choices regarding water treatment and consumption by condensing complex water quality data into a single numerical value based on multiple water quality parameters. It is expressed as,

$$DWQI = \sum_{i=1}^{n} SI\, i$$

Where 'SI' is the Sub- index which is calculated from assigned parameter weight, measured concentration (C_i) and the permissible limit (S_i) based on BIS (2012) and WHO (2011) standards and 'n' is the number of parameters.

After the calculation of Water Quality Index, the results obtained are compared with the Water Quality Index (WQI) classification in India, which categorizes groundwater into five quality levels, helping in determining the suitability of groundwater for consumption and indicating the severity of water quality degradation.

The classes are labeled as Class 0, Class 1, Class 2, to be used in the prediction. Following the DWQI, the correlation matrix (**Figure 3)** exhibits linear connections between groundwater quality metrics, with coefficients ranging from -1 to +1. Strong positive correlations were found between EC, TDS, Na, and Cl ($r > 0.85$), showing a strong hydrochemical relationship, whereas fluoride, and nitrate showed weaker relations.

Overall, the matrix highlights significant hydrochemical linkages and aids in feature selection for the deep learning-based groundwater quality prediction model.

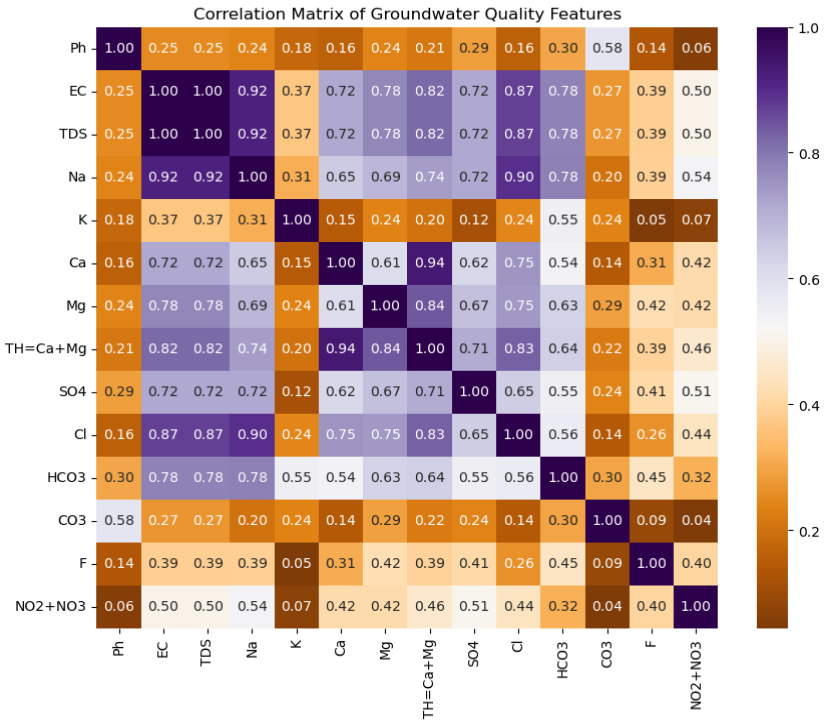

Figure 3. Pearson correlation matrix depicting the strength and direction of linear correlations between groundwater quality metrics, generated to assist in feature selection.

Working of Stochastic Neural Network (SNN) model

Based on Florensa et al. (2017), a broad category of neural networks incorporating stochastic units in the computation are called Stochastic neural networks (SNNs). The SNN model is customized based on the necessities of the research work. This study uses SNN with Monte Carlo Dropout, an effective deep learning method for classification problems that gives uncertainty estimation in addition to predictions. The Framework of SNN model for groundwater quality prediction involves the process of data normalization, assignment of weightages on the neurons, regularization and model compilation after data preparation. Data normalization process is done to ensure that the input features follow a typical Gaussian distribution, a fundamental requirement for accurate and reliable model training called Z-score normalization having been used to normalize the features.

The architecture of the SNN was designed with an input layer, two hidden layers and an output layer. The layout of the input layer is defined in accordance with the number of features. The first hidden layer has 128 neurons with ReLU (Rectified Linear Unit) Activation function and the second hidden layer has 64 neurons. The ReLU activation function was chosen for its computational simplicity, strong gradient propagation, and ability to prevent the vanishing gradient problem, which was observed in trials with deeper networks and in environmental datasets with wide range of parameters. The output layer consists of three units with Softmax activation function. After assigning the neurons, Dropout is used as a regularization method to reduce overfitting. Using Monte Carlo Dropout, the model may assess uncertainty during inference by producing a range of predictions rather than a single output, allowing it to better capture variability and prediction confidence. The model was trained on 80% of the data and tested on the remaining 20%, then combined with the Adam optimizer and Sparse Categorical Cross-Entropy loss. To reduce overfitting, a learning rate of 0.001, 10 epochs, and a batch size of 32, with a 0.5 dropout rate after each dense layer, were employed. Monte Carlo Dropout with 100 stochastic iterations was utilized to assess prediction uncertainty, and early stopping based on validation loss (patience of three epochs) guaranteed training was stopped once convergence was achieved.

Evaluation metrics

In order to evaluate the effectiveness of the deep learning model, computation of evaluation metrics is essential (Müller and Guido, 2016). To guarantee robustness and dependability, the performance of the suggested SNN model was thoroughly assessed using an array of statistical and graphical metrics. Metrics such as Confusion Matrix, Classification Report, Receiver Operating Characteristic (ROC) and Area Under Curve (AUC), are computed to assess the model. According to Pradhan and Kumar (2019), a confusion matrix, also referred to as an error matrix, is generated by comparing the observations on actual and predicted values of the dataset. For a multiclass classification problem, the confusion matrix is taken as 3×3 matrix for three classes, with elements - True Positive (TP), False Positive (FP), True Negative (TN) and False Negative (FN). Next, Classification Report is generated which summarizes significant metrics such as accuracy (the percentage of correctly predicted samples), precision (the percentage of relevant instances among predicted positives), recall (the percentage of relevant instances correctly identified), and F1-score (the harmonic mean of precision and recall). ROC curve, a graphical plot illustrates the diagnostic ability of a classifier system as its discrimination threshold is varied and AUC is a numerical value that represents the area under the ROC curve. A higher AUC generally indicates a better-performing model. Cross-validation was applied to assess the model's generalization capabilities; with K-fold CV chosen for its reliability, especially when working with limited environmental datasets. The five-fold CV ensured that each sample contributed to both training and validation, which improved model stability and reduced bias. The model was trained on 80% of the data in each fold and validated on the remaining 20%, and the process was repeated five times to ensure a thorough performance evaluation.

RESULTS AND DISCUSSION

Groundwater quality in the study area was classified into three categories: Excellent (Class 0), Good (Class 1), and Poor (Class 2). Figure 4 reveals that 77% of samples are rated excellent, 18% good, and 5% poor, indicating an evident class imbalance. To address this issue, a class-weighting approach was utilized during model training, with weights assigned in inverse proportion to class frequencies in order to prioritize minority samples while reducing bias toward the majority class. Also, Figure 5 suggests that rainfall patterns play a crucial role in influencing the groundwater quality. As rainfall increases, water quality tends to improve and vice-versa.

Performance of the SNN model across three categories Class 0 (excellent water), Class 1 (good water), and Class 2 (poor water) are depicted in the confusion matrix (Figure 6). With only three samples incorrectly classified as Class 1, the model performs exceptionally well, particularly for Class 0. Class 2 instances are correctly predicted but the iterative instances are very small, may be due to the very low number of data points. The model is dependable for practical groundwater quality evaluation as evidenced by its low misclassification, especially when it comes to detecting good and poor water quality.

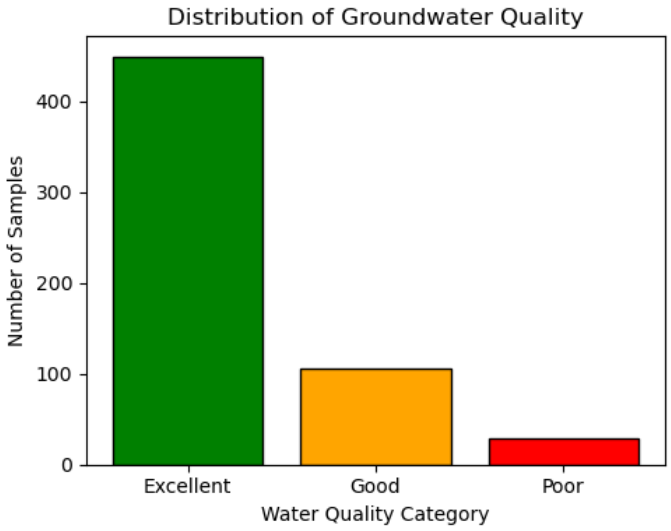

Figure 4. Bar chart illustrating the distribution of groundwater quality classes (excellent, good, and poor) across the study area, based on the Drinking Water Quality Index (DWQI).

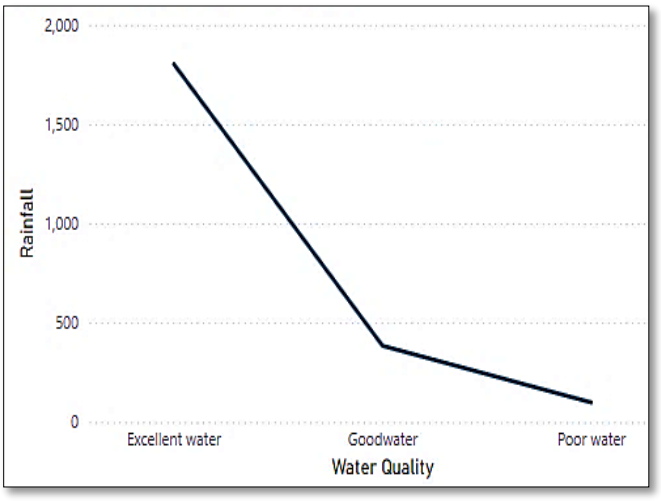

Figure 5. Graph depicting the relationship between groundwater quality classes and rainfall variation in the study area.

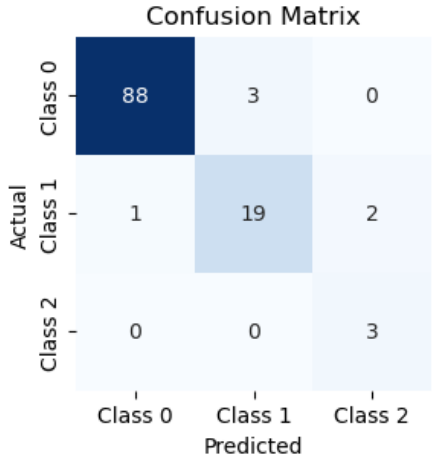

Figure 6. The confusion matrix displaying the classification performance of the Stochastic Neural Network (SNN) model across the three groundwater quality categories.

The classification report (Table 1) demonstrates impressive model performance, with Class 0 attaining near-perfect scores due to its more widespread inclusion in the dataset, Class 1 exhibiting solid precision and recall (0.86), and Class 2 with reduced accuracy but perfect recall despite limited data. Overall, the model reached 95% accuracy, indicating a strong and dependable groundwater quality classification.

To visualize the model's performance across various threshold settings, ROC curves (Figure 7) were generated, giving a graphical representation of the true positive rate (sensitivity) against the false positive rate. The Area Under the Curve (AUC) values for all classes are high, indicating strong classification performance. The ROC-AUC for each class were satisfactory, indicating strong discriminatory ability.

The prediction graph (Figure 8) displays a clear agreement between the actual groundwater quality classes and the SNN model's predicted labels, with real values represented by a blue solid line and forecasts by an orange dotted line. The close overlap of the two curves implies strong sample-wise prediction accuracy. The model's resilience is further confirmed by its high mean cross-validation accuracy of 93% and low standard deviation of 0.03, indicating consistent and reliable performance across all folds.

Table 1. Classification report on the SNN Model.

Class labels	Precision	Recall	F1 score	Support
0	0.99	0.97	0.98	91
1	0.86	0.86	0.86	22
2	0.60	1.00	0.75	3
Accuracy			0.95	116
Macro avg.	0.82	0.94	0.86	116
Weighted avg.	0.95	0.95	0.95	116

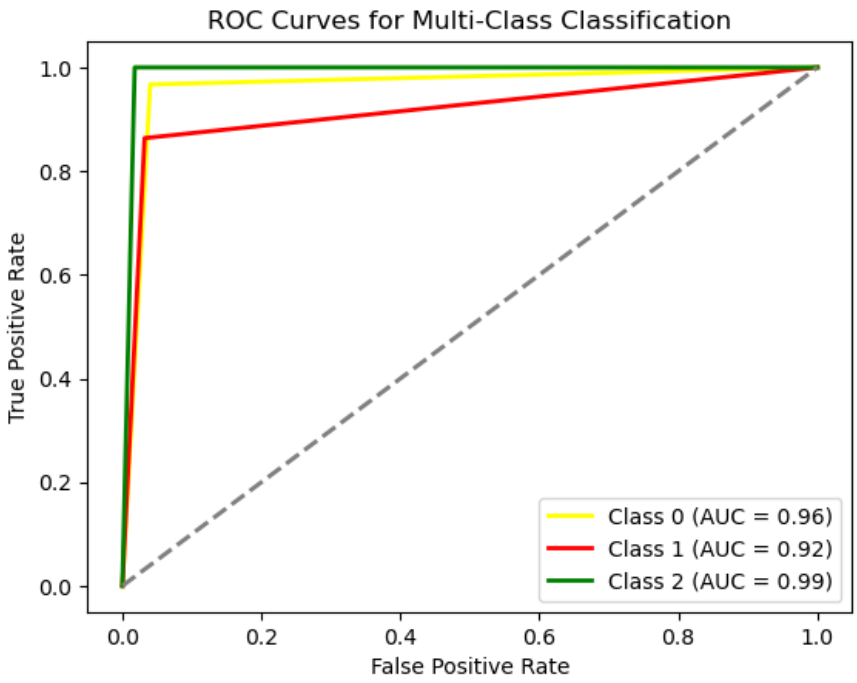

Figure 7. The smooth and well-separated Receiver Operating Characteristic (ROC) curves with corresponding Area Under the Curve (AUC) values for the Stochastic Neural Network (SNN) model generated for the three groundwater quality classes

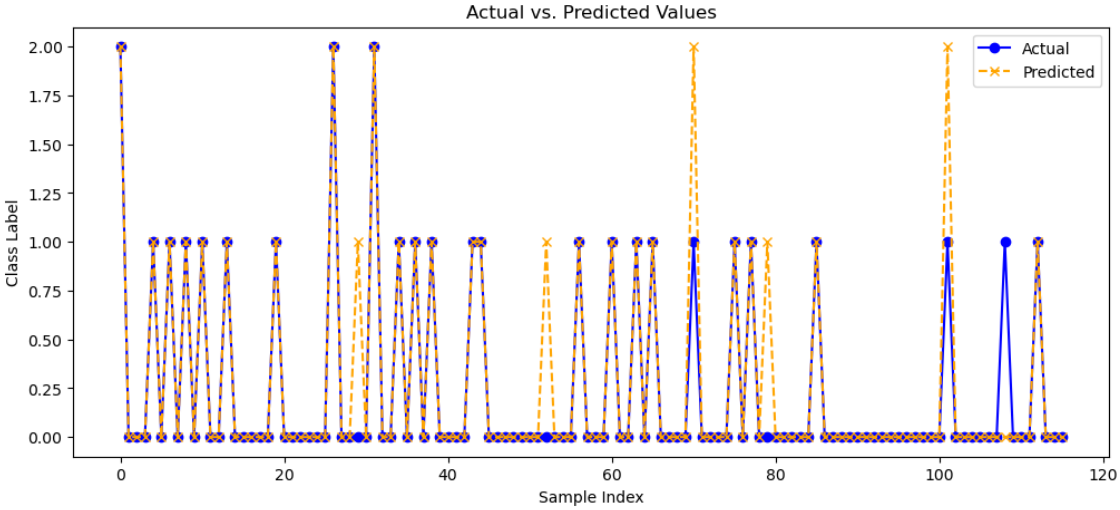

Figure 8. Prediction graph comparing the actual and predicted groundwater quality class labels generated by the Stochastic Neural Network (SNN) model for the test dataset.

Further, the model produces accurate predictions, particularly for Class 0 (excellent water), showing that it has a powerful learning source. Misclassifications occur due to overlapping attributes; yet, Class 1 (good water) is also predicted effectively. Notably, Class 2 (poor water) had perfect recall, which means that no instances of Class 2 were overlooked. The balance between sensitivity and specificity in minority class predictions is statistically supported by the classification report and visually by the prediction graph, which validates the confusion matrix findings. ROC curves of SNN for multi-class classification also demonstrate the effectiveness of the model, with high AUC scores suggesting high level of class separability. Cross-validation resulted in a consistent mean accuracy of 0.93 with moderate variability (SD = 0.03), demonstrating consistency across datasets. Also, the model's increased accuracy with rainfall inclusion shows that it successfully captured these hydrogeological relationships. Overall, the SNN model showed excellent predictive power, with encouraging prospects for environmental monitoring. By incorporating randomness during inference, the SNN model makes it possible to evaluate predictive uncertainty and more accurately reflect groundwater dynamics, an advantage that significantly aids in making sound environmental management decisions.

CONCLUSIONS

In this study, a customized Stochastic Neural Network (SNN) model was developed to categorize and predict groundwater quality in Kanyakumari District of Tamil Nadu. Using Monte Carlo Dropout and a wide range of water quality parameters, the model significantly improved generalization and quantified predictive uncertainty. Evaluation metrics such as the classification report, confusion matrix, and ROC-AUC curves, verified the model's capacity to distinguish between groundwater quality classes, which was further reinforced by consistent 5-fold cross-validation results. With 95% accuracy, the model is suitable for regions with dynamic groundwater, providing probabilistic predictions required for effective groundwater management. Future research might delve into ensemble stochastic models, Bayesian deep learning, or other physical frameworks, as well as extending the approach to real-time applications on IoT-enabled platforms. To gain a more detailed understanding of groundwater quality trends, other hydrogeological, climatological, and human-influenced variables could be included. Adding variables like seasonal fluctuations, land-use changes, and soil composition could increase the accuracy of predictions.

Acknowledgements

The authors extend their sincere gratitude to Dr. Selvam and Dr. Siva Subramanian of Department of Geology, V.O. Chidambaram College, for their valuable insights and constructive comments, which significantly enhanced the clarity and depth of this work. We also express our heartfelt appreciation to Dr. Saravanan and Dr. Arun Bose of Centre for Geotechnology, Manonmaniam Sundaranar University, for their steadfast support and encouragement throughout the study. "The authors express deep gratitude to our Vice Chancellor Prof.Dr.N.Chandrasekar for the invaluable support" Our sincere thanks are further extended to Dr. O. P. Pandey, Chief Editor of JIGU, for his thoughtful guidance and thorough review of the manuscript.

Author Credit Statement

AJ: Conceptualization, methodology, writing original draft, SY: Writing, review and supervision

Data Availability

Data cannot be made publicly available; readers should contact the corresponding author for details.

Compliance with Ethical Standards

The authors declare no conflict of interest and adhere to copyright norms.

REFERENCES

BIS, 2012. Indian standard specification for drinking water, Second Revision, IS 10500: 2012, Publication Unit, Bureau of Indian Standard, Manak Bhawan, New Delhi, pp. 1-6.

Chollet, F., 2017. Deep Learning with Python, Second Edition, Manning Publications Co., Shelter Island, New York, pp. 8.

District Statistical Handbook, 2022-2023. Department of Economics and Statistics, Kanniyakumari District, Government of Tamil Nadu, Land of Cash Crops, India. https://kanniyakumari.nic.in

Domenico, P.A. and Schwartz, F.W., 1990. Physical and Chemical Hydrogeology. Wiley, New York, pp. 824.

Emig, J., Reuter, U., Bolz, P. G., Leischner, S. and Falla, G. C., 2023. A stochastic neural network-based approach for metamodelling of mechanical asphalt concrete properties. Int. J. Pavement Engineering, 24 (1). https://doi.org/10.1080/10298436.2023.2177650

Florensa, C., Duan, Y. and Abbeel, P., 2017. Stochastic Neural Networks for Hierarchical Reinforcement Learning. arXiv (Cornell University). Proc. Int. Conf. Learning Representations (ICLR), Apr. 2017. doi: 10.48550/arxiv.1704.03012.

Gholami, V. and Sahour, H., 2022. Prediction of groundwater drawdown using artificial neural networks. Environ. Sci. Pollution Res., 29(22), 33544-33557. doi: 10.1007/s11356-021-18115-9

Giao, N. T., Nhien, H. T. H., Anh, P. K. and Thuptimdang, P., 2023. Groundwater quality assessment for drinking purposes: a case study in the Mekong Delta, Vietnam. Scientific Reports, v.13, no.1.

Gilli, E., Mangan, C. and Mudry, J., 2012. Hydrogeology: Objectives, Methods, Applications. CRC Press, pp. 4-14.

GSI, 2005. Geology and Mineral Map of Kanyakumari District (eds. Sundaram R., Ranganathan M., and Vasudevan D., compiled in OP: TNKP, Chennai; Published by Geological Survey of India, Southern Region, Hyderabad.

Haggerty, R., Sun, J., Yu, H. and Li, Y., 2023. Application of machine learning in groundwater quality modeling - A comprehensive review. Water Res., v.233, 119745

Kalariya, V., Parmar, P., Jay, P., Tanwar, S., Raboaca, M. S., Alqahtani, F., Tolba, A. and Neagu, B., 2022. Stochastic neural Networks-Based algorithmic trading for the cryptocurrency market. Mathematics, 10(9), 1456. https://doi.org/ 10.3390/math10091456

Karamouz, M., Ahmadi, A. and Akhbari, M., 2011. Groundwater hydrology: Engineering, Planning, and Management. CRC Press, p. 142

Karnena, M. K. and Saritha, V., 2019. Evaluation of Spatial Variability in Ground Water Quality using Remote Sensing. Int. J. Recent Technol. Engineering (IJRTE), 8(2), 4269-4278

Kirsch, R., 2006. Groundwater geophysics: a tool for hydrogeology, Second Edition, Choice Reviews Online, Springer, 44, pp. 511.

Kishor, K., Aggarwal, A., Srivastava, P. K., Sharma, Y. K., Lee, J. and Ghobadi, F., 2025. A Systematic Literature Review of MODFLOW Combined with Artificial Neural Networks (ANNs) for Groundwater Flow Modelling. Water, 17(16), 2375. https://doi.org/10.3390/w17162375

Kulisz, M., Kujawska, J., Przysucha, B. and Cel, W., 2021. Forecasting water quality index in groundwater using artificial neural network. Energies, *14*(18), 5875; https://doi.org/10.3390/en14185875

Lohani A.K. and Krishnan. G., 2015. Groundwater level simulation using artificial neural network in southeast, Punjab, India. J. Geol. Geophys., 4(3). DOI: 10.4172/2329-6755.1000206

Müller, A. C. and Guido, S., 2016. Introduction to Machine Learning with Python: A Guide for Data Scientists, 279-299.

Pradhan, M. and Kumar, U. D., 2019. Machine Learning with Python. Pp.149-160

Sarmadi, S., Winkle, J. J., Alnahhas, R. N., Bennett, M. R., Josić, K., Mang, A. and Azencott, R., 2022. Stochastic neural networks for automatic cell tracking in microscopy image sequences of bacterial colonies. Math. and Computational Appl., 27(2), 22. https://doi.org/10.48550/arXiv.2104.13482

Schneider, E., Dai, L., Topper, R. Q., Drechsel-Grau, C. and Tuckerman, M. E., 2017. Stochastic Neural Network Approach for learning High-Dimensional Free Energy Surfaces. Phys. Rev. Lett., 119 (15), 150601

Stylianoudaki, C., Trichakis, I. and Karatzas, G. P., 2022. Modeling groundwater nitrate contamination using artificial neural networks. Water, 14(7). 1173; https://doi.org/10.3390/w14071173

Vasanthavigar, M., Srinivasamoorthy, K., Vijayaragavan, K., Ganthi, R. R., Chidambaram, S., Anandhan, P., Manivannan, R. and Vasudevan, S., 2010. Application of water quality index for groundwater quality assessment: Thirumanimuttar sub-basin, Tamilnadu, India. Environ. Monitoring and Assess., 171. 595-609.

WHO, 2011. World Health Organisation. Guidelines for Drinking Water Quality, 4th ed., pp. 223-228

Received on 17-05-2025; Revised on 22-11-2025; Accepted on 29-11-2025

J. Ind. Geophys. Union, 30(1) (2026), 78-85
https://doi.org/10.71122/JIGU.30(1)2026.008

Centre for Geothermal Energy Research (CGER) at CSIR–NGRI, Hyderabad: Advancing sustainable geothermal energy in India

Labani Ray[1,2,*], Rama Mohan Kurakalva[1,2], Ved Prakash Maurya[1,2], Niraj Kumar[1,2], Biswajit Mandal[1,2], Nishu Chopra[1,2], K.N.D. Prasad [1,2], Imlirenla Jamir[1,2], Pratul Ranjan[1,2], Nagaraju Podugu[1], P. Karuppannan[1], Dewashish Kumar[1,2], M. Satyanarayanan[1,2] and K.J.P. Lakshmi[1]
[1]CSIR-National Geophysical Research Institute, Hyderabad 500007, India
[2]Academy of Scientific and Innovative Research (AcSIR), Ghaziabad 201002, India
*Corresponding author: labani.ngri@csir.res.in

INTRODUCTION

The CSIR–National Geophysical Research Institute (CSIR–NGRI), Hyderabad (India), is country's unique geoscientific research institution, dedicated to research investigations spanning from near-surface processes to deep Earth exploration with a strategic focus on natural resource exploration (groundwater, mineral, geothermal energy, and hydrocarbon) and hazard assessment for sustainable development. Among various renewable energy resources, geothermal energy stands out as a reliable, clean, and sustainable resource, capable of providing continuous baseload power, independent of climatic or seasonal variability (Gupta and Roy, 2007). Leveraging its multidisciplinary expertise in geological, geochemical, and geophysical sciences, CSIR–NGRI, the Geological Survey of India (GSI) and other institutions, have led national efforts that have resulted in the delineation of ten geothermal provinces across the country's diverse tectonic settings (Figure 1). Although India possesses considerable geothermal potential, particularly in regions with hot springs, this resource remains largely untapped.

CSIR–NGRI has a long-standing legacy in geothermal research, spanning over six decades, with pioneering contributions in heat flow measurements, subsurface temperature mapping, characterization of rock thermal properties, geophysical imaging, and geochemical analyses across various geological terrains in India (Saxena and Gupta, 1986; Patro, 2017; Ray, 2021).

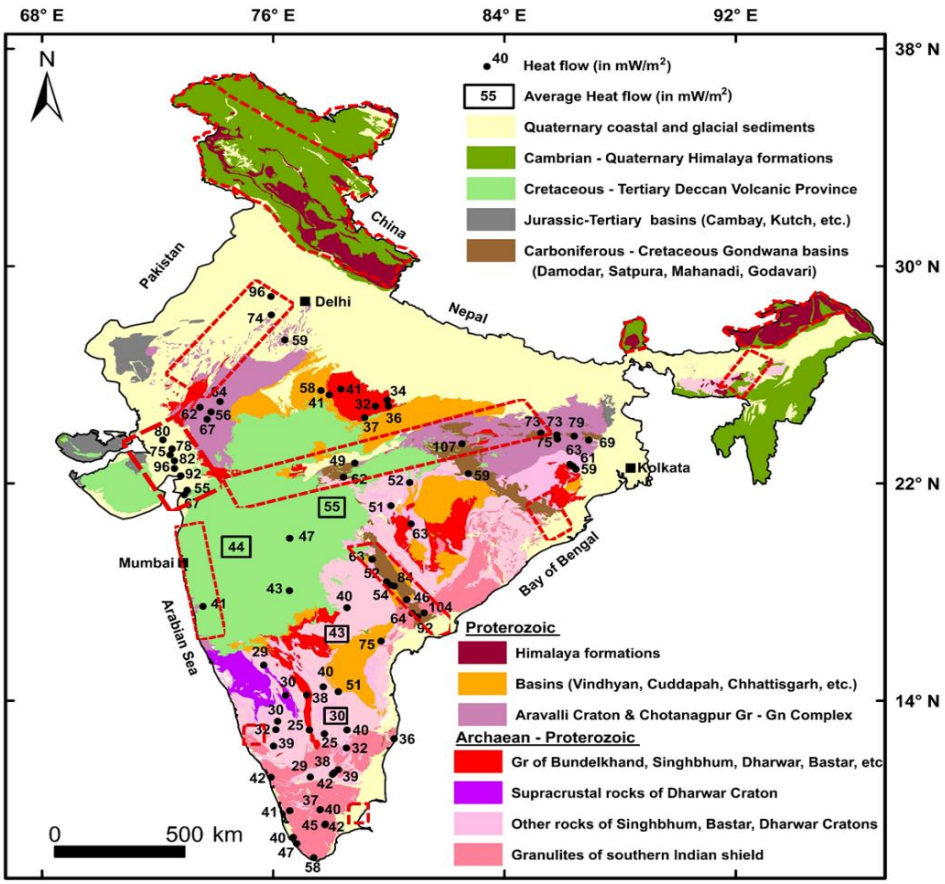

Figure 1. Geological map of India showing geothermal provinces (modified after GSI, 2022) along with heat flow distribution.

These sustained multidisciplinary efforts have provided the scientific foundation for delineating the geothermal reservoirs and advancing site-specific resource assessment in key geothermal provinces. Among the ten identified potential geothermal provinces, this institute is currently leading major integrated investigations in two key geothermal provinces, viz. Puga–Chumathang–Panamik region of the Ladakh Himalaya (Pavankumar et al., 2024; Dutta et al., 2025; Kumar et al. 2025a; Ojha et al., 2025; Patro et al., 2025) and the Tattapani geothermal province in Chhattisgarh (Kumar et al., 2025b; Maurya et al., 2025; Ray et al., 2025a, b, c). These initiatives represent a strategic step towards harnessing indigenous clean energy resources to enhance national energy security and economic development. Furthermore, sustained scientific deliberations through national conclaves (Ray et al., 2023), expert brainstorming, and comprehensive field studies culminated in the establishment of the Centre for Geothermal Energy Research at CSIR–NGRI. This dedicated centre provides a focused institutional framework for advancing geothermal science, developing indigenous technologies, and supporting sustainable geothermal exploitation, in alignment with India's National Policy on Geothermal Energy (Ministry of New and Renewable Energy, MNRE; 2025) and the country's commitment to achieving net-zero emissions by 2070.

CENTRE FOR GEOTHERMAL ENERGY RESEARCH (CGER)

The Centre for Geothermal Energy Research (CGER) was inaugurated on September 9, 2025, by Dr. (Mrs.) N. Kalaiselvi, Director General, CSIR & Secretary, DSIR, Government of India, at CSIR–NGRI, Hyderabad. The event was attended by directors of CSIR sister laboratories, scientists, and staff of CSIR–NGRI (Figure 2). CGER envisions becoming a leading Centre of Excellence in geothermal research by integrating advanced geological, geochemical and geophysical approaches to explore, understand, and harness geothermal energy in a sustainable manner. Its mission is to advance geothermal exploration through integrated geoscientific research (Ray et al., 2025d), foster the development of innovative subsurface technologies, and establish a national geothermal data repository, while nurturing future energy professionals and fostering impactful national and global collaborations.

The CGER will serve as a national hub for geothermal research and development, focusing on subsurface imaging, fluid characterization, and the development of a comprehensive data repository. It fosters national and international collaborations to advance geothermal science and technology. The centre also emphasizes training the next generation of geothermal professionals to build capacity in this emerging sector (Figure 3). Together, these efforts guide CGER's mission to enable sustainable geothermal energy exploration and utilization of geothermal resources in India.

CGER aims to contribute to the United Nations Sustainable Development Goals, including affordable and clean energy (SDG 7), industry, innovation, and infrastructure (SDG 9), sustainable cities and communities (SDG 11), and climate action (SDG 13) (United Nations, 2015). In parallel, the centre advances research in support of India's national missions, Atmanirbhar Bharat and Viksit Bharat 2047. Its vision is fully aligned with India's National Policy on Geothermal Energy (MNRE, 2025) and the country's long-term commitment to achieve net-zero emissions by 2070.

Figure 2. Inauguration of CGER by Dr. N. Kalaiselvi, DG, CSIR, and Secretary, DSIR.

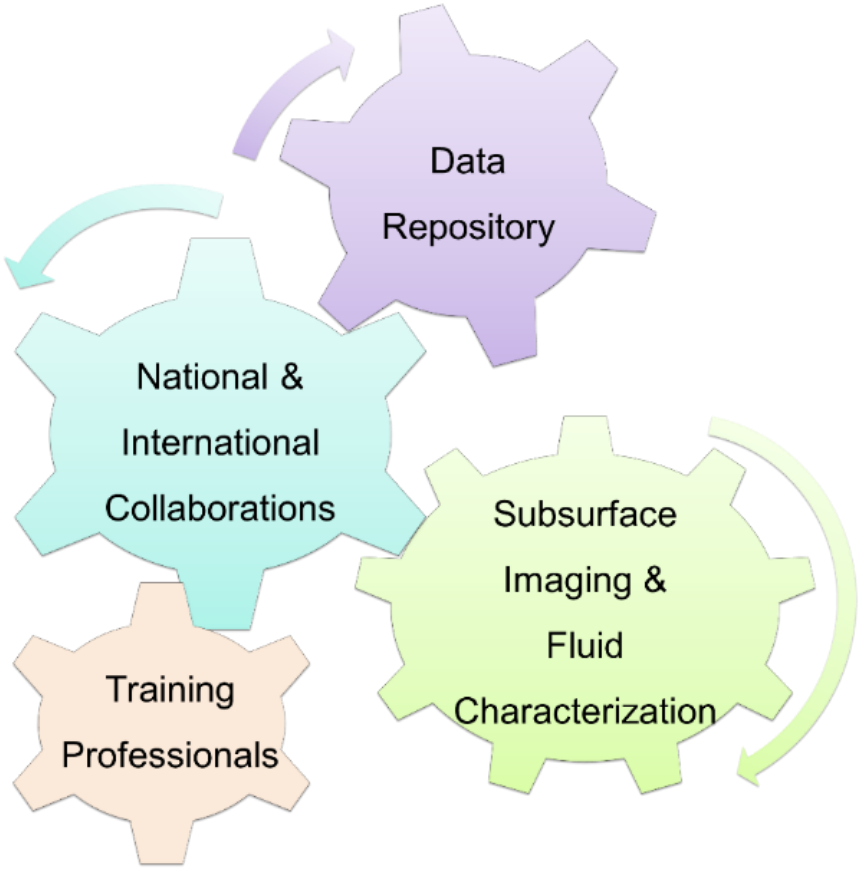

Figure 3. Roles and responsibilities of CGER.

FACILITIES AT CGER

The CGER hosts an integrated facility encompassing geophysical, thermal, rock mechanics, and hydrogeochemical capabilities, forming a comprehensive scientific infrastructure for advancing geothermal research in India. These facilities enable systematic investigation of subsurface heat and fluid flow, reservoir properties, and coupled thermo-hydro-mechanical processes, which are critical for understanding and sustainable development of geothermal systems. Geophysical facilities offer capabilities to characterize subsurface structures and physical properties through the seismic, electrical, electromagnetic, gravity, and magnetic investigations. These tools are crucial for imaging fault systems, mineralized zones, as well as delineating the depth and dimension of the geothermal reservoirs. Mapping of fracture zones and their interconnectivity is mainly done by various electrical methods such as Electrical Resistivity Tomography (ERT) and Electric-field Vector Resistivity Imaging (EVRI), shallow seismic, gravity and magnetic, whereas, deep geothermal reservoirs are investigated by magnetotellurics (MT), seismic and gravity methods (Figure 4).

Thermal facilities are used to determine geothermal gradient, radiogenic heat production, thermophysical properties of rocks and its variation with temperature. These datasets are used to determine surface heat flow, thermal regime of the geothermal provinces (Figure 5).

Rock mechanics facilities focus on the mechanical behaviour of rocks and geomaterials under controlled stress, temperature, and pore pressure conditions. They support experimental studies on rock strength, deformation, fracture propagation, and thermo-hydro-mechanical (THM) coupling, which are vital for understanding reservoir stability, induced seismicity, underground excavations, and subsurface energy storage (Figure 6).

Hydrogeochemical facilities enable detailed analysis of groundwater and geothermal fluids, including major ions, trace elements, isotopes, and gas chemistry. These analyses provide critical insights into fluid origin, evolution, water–rock interaction processes, and geochemical controls on resource sustainability and environmental quality (Figure 7).

Figure 4. Geophysical field instrumentation set-ups for subsurface investigations in geothermal exploration **(a)** Electrical Resistivity Tomography **(**ERT), **(b)** Electric-field Vector Resistivity Imaging (EVRI), **(c)** Magnetotellurics (MT), **(d)** Seismic, **(e)** Gravimeter, and **(f)** Magnetometer.

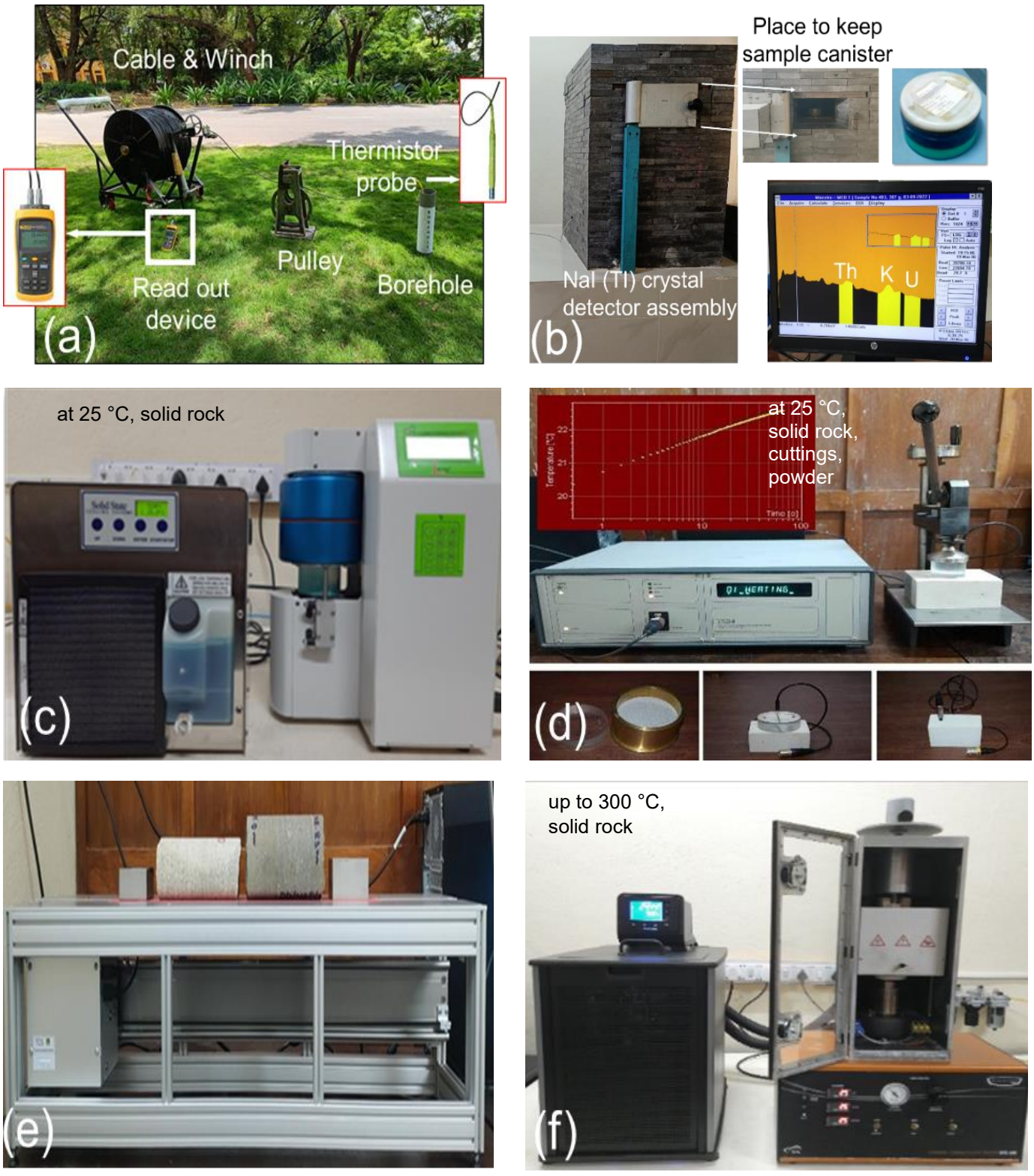

Figure 5. Field and laboratory facilities for thermal investigations in geothermal exploration. **(a)** Borehole temperature logging set-up, **(b)** Rock radioactivity measurement set-up, **(c)** Steady-state thermal conductivity meter, **(d)** Transient thermal conductivity meter, **(e)** Thermal conductivity scanner, **(f)** Steady-state thermal conductivity meter at elevated temperature.

Figure 6. Laboratory facilities for rock mechanical and physical properties. **(a)** Universal Testing Machine, **(b)** Triaxial Testing Machine, **(c)** Gas Pycnometer, **(d)** Density and porosity measurement set-up.

Figure 7. Laboratory facilities for hydrogeochemical investigations for geothermal exploration. **(a)** Ion Chromatography with Autosampler for Major anions and cations, **(b)** High Resolution-Inductively Coupled Plasma Mass Spectrometer (HR-ICP-MS) for Trace Elements and REEs, **(c)** Isotope Ratio Mass Spectrometer (IRMS) for Stable isotopes, **(d)** Gas Chromatograph-Mass Spectrometer (GC-MS) for gases.

FUTURE DIRECTIONS AND WAY FORWARD

CGER has outlined its strategic road map for advancing geothermal research and development in India, with a focus on translational outcomes, national priorities, and long-term sustainability, through the following thematic areas.

Advanced geothermal resource assessment and characterization

CGER will enhance integrated geothermal exploration through high-resolution geophysical imaging, heat flow mapping, thermophysical property measurements, and geochemical/isotopic studies. Emphasis will be placed on identifying reservoir depth, geometry, permeability, and sustainable heat extraction potential in both conventional and unconventional geothermal systems across India.

Development of enhanced and low-enthalpy geothermal systems

Future research will focus on Enhanced Geothermal Systems (EGS), as well as medium- to low-enthalpy resources and direct-use applications. Numerical modeling of thermal–hydraulic–mechanical (THM) processes will support feasibility assessments and reservoir sustainability.

Feasibility demonstration and technology translation

CGER will work towards pilot-scale geothermal demonstration projects in collaboration with MNRE, PSUs, state agencies, and industry partners. This will serve to validate technology, reduce risk, and facilitate the transition from exploration to utilization, thereby bridging the gap between research and applications.

Geothermal integration with energy systems and net-zero goals

It involves integrating geothermal energy with hybrid renewable systems (solar–geothermal, geothermal heat pumps) and district heating/cooling networks. CGER will contribute to de-carbonization strategies aligned with India's net-zero emissions target for 2070 by promoting geothermal as a reliable, base-load, and climate-resilient energy source.

Digital geothermal atlas and national data repository

The CGER aims to develop a dynamic, GIS-based geothermal database that integrates geological, geophysical, geochemical, and thermal datasets. This digital platform will support national planning, investor confidence, and evidence-based policymaking under India's National Policy on Geothermal Energy.

Capacity building, skill development and knowledge dissemination

The Centre will strengthen human resource development through specialized training programs, doctoral and postdoctoral research, and international exchange initiatives. Outreach to state governments, academia, and industry will enhance awareness and promote informed decision-making for the development of geothermal energy.

International collaboration and policy support

CGER will expand strategic collaborations with leading global institutions to adopt best practices, advanced modelling tools, and innovative technologies. Scientific outputs will directly support national geothermal roadmaps, regulatory frameworks, and long-term energy planning.

CONCLUDING REMARKS

The establishment of the Centre for Geothermal Energy Research (CGER) at CSIR–NGRI, represents a significant step toward creating a unified national platform for advancing geothermal science, technology, and policy support in India. By integrating geological, geophysical, geochemical, and thermal studies, CGER addresses critical knowledge gaps related to resource characterization, reservoir sustainability, and utilization pathways across the country's diverse geothermal provinces. This multidisciplinary framework enables a scientifically robust assessment of geothermal potential, supporting the transition from exploration-driven studies to application-oriented outcomes. CGER's strategic focus on medium-to-low enthalpy systems, enhanced geothermal concepts, direct-use applications, and pilot-scale demonstrations, will position geothermal energy as a reliable, indigenous, and environmentally sustainable component of India's energy portfolio. The Centre's efforts contribute directly to national priorities, including energy security, de-carbonization, and regional development, while supporting India's commitments under the National Policy on Geothermal Energy and the net-zero emissions target for 2070. Through capacity building, digital data integration, and strong national and international collaborations, CGER strengthens India's technical and human resource base for long-term geothermal development. It is also aligned with the United Nations Sustainable Development Goals and national missions such as "Atmanirbhar Bharat" and "Viksit Bharat 2047", CGER exemplifies the role of science-driven institutions in enabling sustainable growth. Overall, the centre is poised to play a transformative role in translating India's geothermal potential into tangible benefits for society, the economy, and the environment.

Acknowledgements

The authors sincerely thank Dr. Prakash Kumar, Director, CSIR–NGRI, for his consistent support, encouragement, and guidance. The contributions and cooperation of the Geological Survey of India (GSI), ONGC Energy, Oil India Limited (OIL), the Ministry of New and Renewable Energy (MNRE), the Ministry of Earth Sciences (MoES), and academic collaborators, are gratefully acknowledged. This work is published with the approval of CSIR–NGRI vide reference number NGRI/Lib/2025/Pub-147

References

Dutta, A., Ray, L., Chopra, N., Prajapati, S.K., Sidagam, E.R., Podugu, N., Dudhate, A.P., Uddandam, S.K. and Raj, A., 2025. Recent Geothermal Investigations in the Ladakh Himalaya, India: Implications for Future Geothermal Energy Exploration. J. Geol. Soc. India, 101(6), 995-1001.

GSI, 2022. Geothermal Atlas of India, Geological Survey of India, Government of India, Special publication 125.

Gupta, H.K., and Roy, S. 2007. Geothermal Energy: An Alternative Resource for the 21st Century. Elsevier.

Kumar, D., Ojha, A.K., Maurya, V.P., Satyanarayanan, M., Dhakate, R., Kumar, P., Kumar, D. and Rathore, J.S. 2025a. New insight into the shallow sub-surface for geothermal prospection of Puga valley, Ladakh, India from electrical resistivity tomography. Geothermics, 131, 103409.

Kumar, N., Prasad, K.N.D. and Ray, L. 2025b. Gravity-Based Structural Characterisation of the Tatapani Geothermal Province, Central India. AGU Annual Meeting, Dec. 15-19, New Orleans, Louisiana.

Maurya, V. P., Mishra, A., Ray, L., Srinivas, N., and Podugu, N. 2025. Near-Surface Electrical Prospecting for a Geothermal System in Central India. AGU Annual Meeting, Dec. 15-19, New Orleans, Louisiana, USA.

MNRE, 2025. National Policy on Geothermal Energy, Ministry of New and Renewable Energy, Government of India.

Ojha, A., Kumar, D. and Satyanarayanan, M. 2025. Heat source for the Himalayan hot springs: A view from the Puga Geothermal Field, Ladakh, India. Geothermics, 135 (103537), 1 – 20.

Patro, P.K. 2017. Magnetotelluric Studies for Hydrocarbon and Geothermal Resources: Examples from the Asian Region. Surv. Geophys., 38, 1005−1041.

Patro, P.K., Dhamodharan, S., Durga, V., Azeez, K.A., Babu, N., Reddy, K.C., Gupta, A.K. and Krishna, M.S., 2025. Delineation of a geothermal source beneath the Panamik-Changlung Hot Springs along the Karakoram Fault, Ladakh, India, using magnetotelluric studies. J. Volcanol. Geoth. Res., 108478.

Pavankumar, G., Manglik, A., Demudu Babu, M., Kandregula, R. S. and Barman, A., 2024. A potential deep geothermal reservoir in eastern Ladakh as inferred from the upper crustal geoelectric structure of the region. Phys. Earth Planet. Int., 356, 107263.

Ray, L., 2021. Heat Flow Studies in India: An Update. J. Geol. Soc. India, 97, 1214–1225.

Ray L., Chopra N., Podugu N., Sarolkar P.B., Dutta A., Prajapati S.K. and Dudhate, A. P., 2023. Report on workshop on 'Geothermal Energy Resources of India: Present Status and Way Forward' at CSIR-National Geophysical Research Institute, Hyderabad. J. Geol. Soc. India, 99(11), 1626-1629.

Ray, L., Kurakalva, R. M., Maurya, V. P., Kumar, N., Chopra, N., Prasad, K.N.D., Jamir, I. Kumar, D., Satyanarayanan, M., Podugu, N., Uddandam, S.K., Fatima, M., Nidharshan, B. M., Mohapatra, P., Chandrapuri, S., Lakshmi, K.J.P., Prakash, O., Mishra, A., Srinivas, N., Mandal, B., Ranjan, P., Karuppannan, P., Pandey, V., Prem Kumar, N., Attar, Md. R. S., and Lohithkumar, K., 2025a. Geothermal Potential at Tattapani Hot Spring Region, Central India: Current Status and Future Prospects. SPG Biennial International Conference & Exposition, Dec. 26-28, JECC Jaipur, Rajasthan, India.

Ray, L., Kurakalva, R. M., Maurya, V. P. and Kumar, N., 2025b. Exploring Geothermal Resources in India: Current Scenario and Future Prospects. AGU Annual Meeting, Dec. 15-19, New Orleans, Louisiana, USA.

Ray, L., Chopra, N., Fatima, M., Nidharshan, B. M., Mohapatra, P., Podugu, N., Uddandam, S.K., Prajapati, S.K., Dutta, A. and Chandrapuri, S., 2025c. Insights into Thermal Properties and Subsurface Thermal Structure of the Tattapani Geothermal Province, central India. AGU Annual Meeting, Dec. 15-19, New Orleans, Louisiana, USA.

Ray, L. Kurakalva, R. M., Maurya, V. P., Kumar, N., Mandal, B., Chopra, N., Prasad, K.N.D., Jamir, I., Ranjan, P., Podugu, N., Karuppannan, P., Kumar, D., Satyanarayanan, M. and Lakshmi, K.J.P., 2025d. Harnessing the Earth's Heat: Establishment of the Centre for Geothermal Energy Research (CGER) at CSIR–NGRI for Advancing India's Clean Energy Future. J. Geol. Soc. India, 1-5.

Saxena, V. K., and Gupta, M. L., 1986. Geochemistry of the thermal waters of Salbardi and Tatapani, India. Geothermics, 15(5-6), 705-714.

United Nations, 2015. Transforming our world: The 2030 Agenda for Sustainable Development.

Received on 3-12-2025; Revised on 29-12-2025; Accepted on 31-12-2025

GUIDE FOR AUTHORS

The Journal of Indian Geophysical Union (JIGU), a SCI Journal published bimonthly by the Indian Geophysical Union (JIGU), is an inter disciplinary journal from India that publishes high-quality research in earth sciences with special emphasis on the topics pertaining to the Indian subcontinent and the surrounding Indian Ocean region. The journal covers several scientific disciplines related to the Earth sciences such as solid Earth Geophysics, geology and geochemistry, apart from marine, atmosphere space and planetary sciences. J-IGU welcomes contributions under the following categories :

*Research articles, short notes and students section reporting new findings, results, etc.

*Review articles providing comprehensive overview of a significant research field.

In addition, JIGU also welcomes short communications, after communications and report on scientific activity, book reviews, news and views, etc.

The manuscript should be submitted electronically as a single word format (.doc file) including the main text, figures, tables, and any other supplementary information along with the signed "Declaration Letter". The manuscript should be submitted by email (jigul1963@ gmail.com) to the Chief Editor.

After acceptance of the manuscript the corresponding author would be required to submit all source files (text and Tables in word format) and figure in high resolution standard (*.jpg, *.tiff, *.bmp) format. These files may be submitted to JIGU as a single *.zip file along with the "Copyright Transfer Statement".

IMPORTANT INFORMATION

Ethics in publishing; J-IGU is committed to ensuring ethics in publication and takes a serious view of plagiarism including self-plagiarism in manuscripts submitted to the journal, Authors are advised to ensure ethical values by submitting only their original work and due acknowledgement to the work of others used in the manuscript. Authors must also refrain from submitting the same manuscript to more than one journal concurrently, or publish the same piece of research work in more than one journal, which is unethical and unacceptable. Editor of JIGU is committed to make every reasonable effort to investigate any allegations of plagiarism brought to his attention, as well as instances that come up during the peer review process and has full authority to retract any plagiarized publication from the journal and take appropriate action against such authors if it is proven that such a misconduct was intentional.

Similarly, Editor and Reviewers are also expected to follow ethical norms of publishing by ensuring that they don't use any unpublished information, communicated to them for editorial or review purpose, in their own research without the explicit written consent of the author. They are also expected to keep manuscript' data/ observations/ any other information related to the peer review confidential to protect the interest of the authors. Reviewers should refrain from reviewing the manuscripts in which they have conflicts of interest resulting from competitive, collaborative, or other relationships or connections with any of the authors, companies, or institutions connected to the manuscript.

Conflict of interest

All authors are requested to disclose any actual or potential conflict of interest including any financial, personal or other relationships with other people or organizations within three years of beginning the submitted nor that could inappropriately influence, or be perceived to influence, their work.

Submission declaration

Submission of a manuscript implies that the work has not been published previously and it is not under consideration for publication elsewhere, and that if accepted it will not be published elsewhere in the same or any other form, in English or in any other language, without the written consent of the publishers. It also implies that the authors have taken necessary approval from the competent authority of the institute/organization where the work was carried out.

Copyright

After acceptance of the manuscript the corresponding author would be required to sign and submit the "Copyright Transfer Statement".

MANUSCRIPT PREPARATION

The corresponding author should be identified (include E-mail address, Phone/Mobile number). Full affiliation and postal address must be given for all co-authors.

Abstract:

An abstract of not more than 300 words must be included.

Text:

The manuscript should be structured to include a front page containing the title, Author(s) name, affiliation and address of the institute, where the work was carried out, and 5-to-6 Key words. Author(s) present address, if different from the above mentioned address, may be given in the footnote. The corresponding author should be identified with an asterisk and his/her email ID should be provided. This page should be followed by the main text consisting of Abstract, Introduction, Methods/ Techniques/ Area description, Results, Discussion, Conclusions, Acknowledgements, and References. Tables and Figures with captions should be inserted at the end of main text. It should not be inserted in the body of the text.

Figures/ Illustrations:

figures should be provided in camera-ready form, suitable for reproduction (which may include reduction) without retouching. Figures in high-resolution (at least 300 dpi) standard formats (*.jpg, * tiff, *.bmp) are acceptable. Figures should be numbered according to their sequence in the text. References should be made in the text to each figure. Each figure should have a suitable caption.

Tables:

Authors should take note of the limitations set by the size and layout of the journal. Table should not exceed the printed area of the page. They should be typed on separate sheets and details about the tables should be given in the text. Heading should be brief. Large tables should be avoided and may be provided as supplementary information, if required.

Equations:

Equations should be numbered sequentially with Arabic numerals and cited in the text. Subscripts and Superscripts should be set off clearly.

Equation writing software that presents each equation as an object in MS Word will be accepted. Style and convention adopted for the equations should be uniform throughout the paper.

References:

All references to publications cited in the main text should be presented as a list of references in order following the text and all references in the list must be cited in the text. References should be arranged chronologically, in the text. The list of references should be arranged alphabetically at the end of the paper.

References should be given in the following form:

Kaila, K.L., Reddy PR., Mall D.M., Venkateswarlu, N., Krishna V.G. and Prasad, A.S.S.S.R.S., 1992, Crustal structure of the west Bengal el eon deep seismic sounding investigations. Geophys. J. Int., 1,45-66.

REVIEW PROCESS:

All manuscripts submitted to the journal are peer-reviewed. It is advisable to send the contact details of 4 potential reviewers along with the manuscript to expedite the review process. Editor has the option to select reviewers from the list or choose different reviewers. The review process usually takes about 3 months. All enquiries regarding the manuscript may be addressed to the Chief Editor.

GALLEY PROOF:

Technical editing of manuscripts is performed by the editorial board. The author is asked to check the galley proof for typographical errors and to answer queries from the editor. Authors are requested to return the corrected proof within two days of its receipt to ensure uninterrupted proceedings The editor will not accept new material in proof unless permission from the editorial board has been obtained for the addition of a "note added in proof". Authors are liable to be charged for excessive alterations to galley proof.

PUBLICATION CHARGES:

There are no page charges for publication. The corresponding author will receive a soft copy (pdf format) of his/her published article. Should the author desire to purchase reprints of his/her publication, he/she must send the duly signed Reprint Order Form (accompanies the galley proof and contains price details) along with the corrected galley proof to the Editor. The reprint charges must be paid within one month of sending the Reprint Order Form.

Any payment related to printing or purchase of reprints should be made in the form of a Demand Draft in the name of Treasurer, Indian Geophysical Union, payable at Hyderabad.

You may download the pdf file from:
http://iguonline.in/journal/instructions.php